

STRUCTURE AND MAGNETIC PROPERTIES OF  
MANGANESE-BISMUTH COMPOSITE



A Thesis Submitted in Partial Fulfillment of the Requirements for the  
Degree of Doctor of Philosophy in Applied Physics  
Suranaree University of Technology  
Academic Year 2021

โครงสร้างและสมบัติเชิงแม่เหล็กของสารคอมโพสิต  
ระหว่างแมงกานีสและบิทัมส



นายเสถียรพงศ์ งามสมฤทธิ์

วิทยานิพนธ์นี้เป็นส่วนหนึ่งของการศึกษาตามหลักสูตรปริญญาวิทยาศาสตรดุษฎีบัณฑิต

สาขาวิชาฟิสิกส์ประยุกต์

มหาวิทยาลัยเทคโนโลยีสุรนารี

ปีการศึกษา 2564

# STRUCTURE AND MAGNETIC PROPERTIES OF MANGANESE-BISMUTH COMPOSITE

Suranaree University of Technology has approved this thesis submitted in partial fulfillment of the requirements for the Degree of Doctor of Philosophy.

Thesis Examining Committee



(Dr. Wiwat Nuansing)

Chairperson



(Assoc. Prof. Dr. Prayoon Songsiriritthigul)

Member (Thesis Advisor)



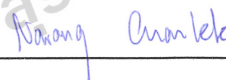
(Prof. Dr. Rattikorn Yimnirun)

Member



(Prof. Dr. Supree Pinitsoontorn)

Member



(Dr. Narong Chanlek)

Member



(Assoc. Prof. Dr. Chatchai Jothityangkoon)

Vice Rector for Academic Affairs

and Quality Assurance



(Prof. Dr. Santi Maensiri)

Dean of Institute of Science

เสถียรพงศ์ งามสมฤทธิ์ : โครงสร้างและสมบัติเชิงแม่เหล็กของสารคอมโพสิตระหว่าง  
แมงกานีสและบิสมัท (STRUCTURE AND MAGNETIC PROPERTIES OF MANGANESE-  
BISMUTH COMPOSITE). อาจารย์ที่ปรึกษา : รองศาสตราจารย์ ดร.ประยูร ส่งสิริฤทธิกุล,  
126 หน้า.

คำสำคัญ: แมงกานีส-บิสมัท, โคบอลต์

วิทยานิพนธ์ฉบับนี้มุ่งเน้นไปที่การพัฒนากระบวนการเผาผนึกภายใต้ภาวะความเป็นสุญญากาศ, การสังเคราะห์สารแม่เหล็กที่มีส่วนผสมระหว่างแมงกานีสและบิสมัทด้วยเงื่อนไขที่เหมาะสม ตรวจสอบสารคอมโพสิตระหว่างแมงกานีสบิสมัทและโคบอลต์ และการพัฒนาระบบออกไซด์รีดักชัน เพื่อการศึกษาและปรับปรุงคุณสมบัติเชิงแม่เหล็ก โดยในขั้นตอนแรกเป็นการออกแบบและพัฒนา เทคนิคการเผาผนึกภายใต้ความเป็นสุญญากาศขั้นสูงพิเศษ ( $\sim 10^{-8}$  mbar) อันเนื่องมาจากแมงกานีส ออกไซด์จะเกิดขึ้นทันทีเมื่อแมงกานีสบริสุทธิ์สัมผัสกับออกซิเจน ดังนั้นกระบวนการเผาผนึกที่ประกอบ ขึ้นมาในงานวิจัยนี้จึงจำเป็นต้องเลี่ยงการมีอยู่ของออกซิเจนในระบบ ขั้นตอนการสังเคราะห์สาร แม่เหล็กแมงกานีสบิสมัท (MnBi) นั้นมีพารามิเตอร์มากมายที่จะส่งผลกระทบต่อคุณสมบัติเชิง แม่เหล็ก โดยในงานวิจัยนี้ได้ทำการศึกษาพบว่า ค่าพารามิเตอร์ที่เหมาะสมในการสังเคราะห์มี ดังต่อไปนี้ ขนาดของผงอนุภาค MnBi ที่เล็กกว่า 20 ไมครอน ความเป็นสุญญากาศระหว่างการเผา ผนึกต้องรักษาไว้ไม่ให้เกิน  $10^{-7}$  mbar ขนาดอนุภาคสารตั้งต้นแมงกานีสเล็กกว่า 10 ไมครอน อัตราส่วนอะตอมระหว่าง แมงกานีส:บิสมัท เท่ากับ 1:1 อุณหภูมิที่ใช้ในการเผาผนึกอยู่ที่ 275 องศา เซลเซียส และค้างอุณหภูมิไว้เป็นเวลา 12 ชั่วโมง ด้วยค่าพารามิเตอร์ที่เหมาะสมนี้ทำให้ได้ค่าลบล้าง ความเป็นแม่เหล็ก (coercivity: Hc) อยู่ที่  $4.28 \pm 0.07$  kOe ค่าความอิ่มตัวเชิงแม่เหล็ก (saturated magnetization: Ms) อยู่ที่  $53.42 \pm 0.90$  emu/g และค่าผลผลิตพลังงานสูง (maximum energy product: (BH)max) อยู่ที่  $1.98 \pm 0.05$  MGOe นอกจากนี้ งานวิจัยนี้ยังได้ทำการศึกษาลงผลกระทบต่อ การเติมโกลเดียมในระหว่างกระบวนการอบแมงกานีสพบว่า การฟอร์ตตัวเป็นวัสดุแม่เหล็กแมงกานีส บิสมัทถูกขัดขวางด้วยกลุ่มไฮโดรคาร์บอน ที่เคลือบอยู่บนอนุภาคแมงกานีส และการเจือสารแม่เหล็ก MnBi ด้วยโคบอลต์พบว่าอันตรกิริยาทางแม่เหล็กระหว่าง hard magnetic และ soft magnetic phase เป็นไปตามค่าทางทฤษฎี อีกทั้งยังได้มีการออกแบบและสร้างระบบรีดักชันออกไซด์ เพื่อเพิ่ม ประสิทธิภาพเชิงแม่เหล็ก

สาขาวิชาฟิสิกส์  
ปีการศึกษา 2564

ลายมือชื่อนักศึกษา เสถียรพงศ์ งามสมฤทธิ์  
ลายมือชื่ออาจารย์ที่ปรึกษา ประยูร ส่งสิริฤทธิกุล

SATIENRAPONG NGAMSOMRIT : STRUCTURE AND MAGNETIC PROPERTIES OF  
MANGANESE-BISMUTH COMPOSITE. THESIS ADVISOR : ASSOC. PROF. PRAYOON  
SONGSIRIRITTHIGUL, Ph.D. 126 PP

Keyword: Manganese-Bismuth, Cobalt

This thesis focuses on the development of vacuum sintering systems and manganese-bismuth-based magnetic synthesis under optimal conditions, examine the alloy of Mn, Bi, and Co. As well as the development of oxide reduction systems for the study and improvement of magnetic properties. The first step was to design and develop a sintering technique with an ultra-high vacuum ( $\sim 10^{-8}$  mbar). When pure Mn is exposed to oxygen, manganese oxide forms immediately. Therefore, the sintering system incorporated into this research was necessary to avoid the presence of oxygen in the system. The MnBi magnetic synthesis process has many parameters that affect its magnetic properties. In this research study, it was found that the optimal parameters for the synthesis are as follows. The MnBi powder particle size is smaller than 20 microns. The vacuum during sintering must be maintained at no more than  $10^{-7}$  mbar. The manganese substrate particle size is smaller than 10 microns. The atomic ratio between Mn and Bi 1:1. The sintering temperature is  $275^{\circ}\text{C}$  and is held for 12 hrs. These appropriate parameters, this results in a coercivity ( $H_c$ ) of  $4.28 \pm 0.07$  kOe, a saturated magnetization ( $M_s$ ) of  $53.42 \pm 0.90$  emu/g, and a high energy product maximum energy product (BH) max of  $1.98 \pm 0.05$  MGOe, respectively. In addition, this study examined the effects of glycine addition during the Mn grinding process, found that the formation of MnBi magnetic material was found to be hampered by hydrocarbon groups coated on manganese particles. MnBi magnetic doping with Co, it was discovered that the magnetic interaction between the hard magnetic and soft magnetic phases conformed to the theoretical value, and an oxide reduction system has also been designed and constructed to further improve magnetic efficiency.

School of Physics  
Academic Year 2021

Student's Signature Satienrapong  
Advisor's Signature Prayoon S.

## ACKNOWLEDGEMENTS

This thesis could not be accomplished without help and support from many people, to whom I would like to express my sincere words of acknowledgment.

First and foremost, I would like to express my sincere gratitude to my thesis advisor, Assoc. Prof. Dr. Prayoon Songsiriritthigul, who provided me the guidance, support, and excellent opportunities to carry out this research activity.

I would like to express my grateful to Prof. Dr. Rattikorn Yimnirun who is the thesis defense committee, for his kind support and introduction/suggestion to different aspects of research and science.

I am also very grateful to Prof. Dr. Supree Pinitsoontorn who is also the thesis defense committee, for supporting and providing me the opportunity to access to the VSM system in his laboratory.

I would like to acknowledge Dr. Wiwat Nuansing who is the chairman of the thesis defense committee, for giving me his valuable time.

I would like to thank Dr. Narong Chanlek who is the thesis defense committee, for assistance and guidance in XPS measurements at BL5.3: XPS of SLRI. I would like to thank Dr. Hideki Nakajima, for the opportunity to study and utilize the instrument at the BL.3.2a: PES of SLRI.

My deep gratitude to Dr. Chomphunuch Songsiriritthigul at SLRI for providing me with the opportunity to utilize the instruments at the BL7.2W: MX beamline and Dr. Wantana Klysubun, beamline manager at BL.8: XAS for supporting me to learn about XAS technique.

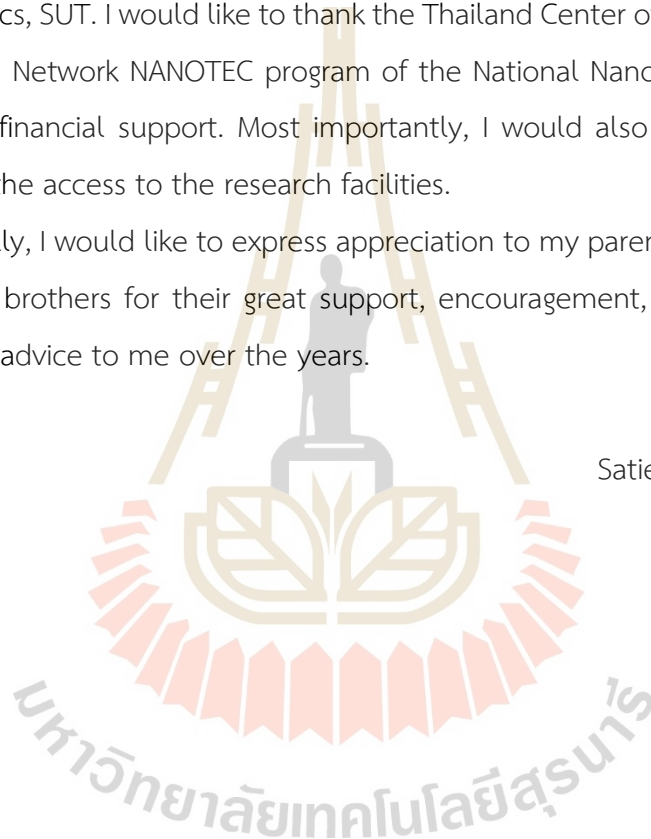
I would like to thank Asst. Prof. Dr. Somchai Maneewan and Asst. Prof. Dr. Chantana Punlek, who were my kind advisors for my undergraduate and master's degrees at Naresuan University. They were very important people who supported and helped me to graduate.

I would like to give big thank to Dr. Thanit Saisopa, Dr. Kittikhun Seawsakul, Dr. Tanachat Eknapakul, the staffs at Beamline 8, Beamline 7.2, Beamline 5.3, and Beamline 3.2 at SLRI, all former and present members of the nanospectroscopy group, school of physics, SUT, all teachers, my friends, my seniors, my juniors, and all staffs in school of Physics, SUT for their support.

I would like to thank the External Grants and Scholarships for Graduate Students (OROG) for financial support towards the degree of Doctor of Philosophy in Applied Physics, SUT. I would like to thank the Thailand Center of Excellence in Physics and Research Network NANOTEC program of the National Nanotechnology Center of Thailand for financial support. Most importantly, I would also like to thank SLRI of Thailand for the access to the research facilities.

Finally, I would like to express appreciation to my parents and both my older and younger brothers for their great support, encouragement, and good aspects as well as good advice to me over the years.

Satienrapong Ngamsomrit



# CONTENTS

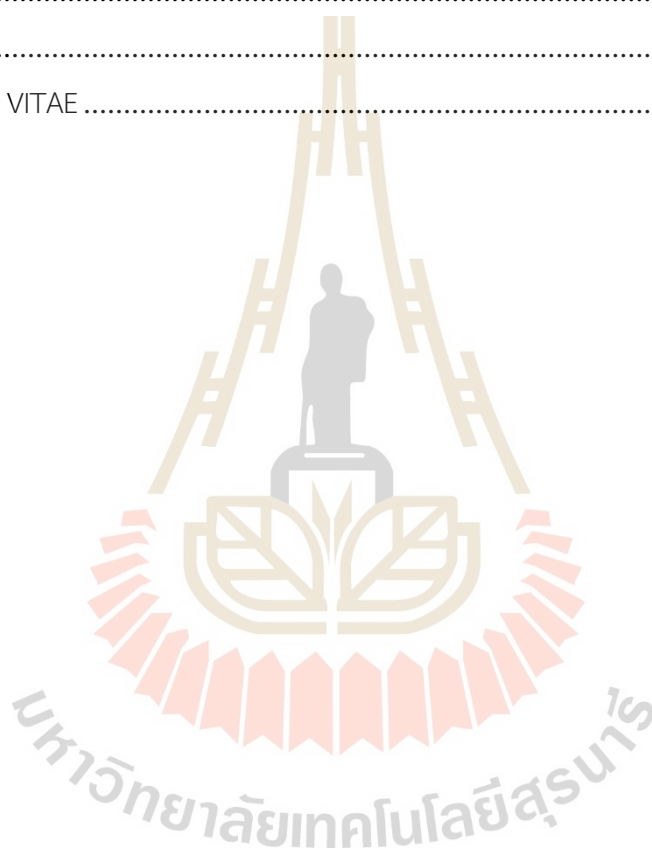
	<b>Page</b>
ABSTRACT IN THAI .....	I
ABSTRACT IN ENGLISH .....	II
ACKNOWLEDGEMENTS .....	III
CONTENTS .....	V
LIST OF TABLES .....	VIII
LIST OF FIGURES .....	IX
<b>CHAPTER</b>	
<b>I INTRODUCTION.....</b>	<b>1</b>
1.1 Background and motivation.....	1
1.2 Objectives of the thesis.....	4
1.3 Outline of the thesis.....	5
<b>II THEORY AND LITERATURE REVIEW.....</b>	<b>6</b>
2.1 Magnetization .....	6
2.2 Induction hysteresis loop and magnetic properties .....	7
2.3 Classification of magnetic materials .....	9
2.3.1 Diamagnetic materials.....	9
2.3.2 Paramagnetic materials.....	10
2.3.3 Ferromagnetic materials .....	11
2.3.4 Anti-ferromagnetic materials.....	11
2.3.5 Ferrimagnetic materials.....	12
2.4 Magnetic domain .....	13
2.5 LTP-MnBi compound .....	15
2.5.1 Properties of LTP-MnBi .....	19

## CONTENTS (Continued)

	<b>Page</b>
2.5.2 Synthesis techniques for LTP-MnBi.....	22
2.5.2.1 Induction melting technique.....	22
2.5.2.1 Melt spinning technique.....	26
2.5.2.3 Chemical method.....	28
2.5.2.4 Sintering technique .....	29
2.5.3 Dilution of LTP-MnBi magnetic materials with the third element....	33
2.5.4 Relation between oxide content and MnBi properties .....	36
2.5.5 MnBi based hard/soft composite magnet .....	39
<b>III RESEARCH METHODOLOGY .....</b>	<b>45</b>
3.1 Instrument development for vacuum sintering system .....	45
3.2 Preparation of LTP-MnBi magnetic materials .....	46
3.3 Preparation of MnBi by Mn grinding time condition.....	49
3.4 Preparation of MnBi by glycine addition condition .....	50
3.5 Preparation of LTP-MnBi and Co composite .....	51
3.6 Preparation of MnBi magnetic materials alignment .....	53
3.7 Characterization of MnBi magnetic materials.....	54
3.7.1 X-ray diffraction.....	54
3.7.2 Scanning electron microscope .....	56
3.7.3 Vibrating sample magnetometer.....	59
3.7.4 BL3.2Ua: Photoemission spectroscopy.....	63
3.7.4.1 BL3.2Ua: Photoemission spectroscopy.....	64
<b>IV RESULTS AND DISCUSSION .....</b>	<b>67</b>
4.1 Commissioning of vacuum sintering system.....	67
4.2 Synthesis of LTP-MnBi .....	69
4.3 Effect of the particle size .....	76
4.4 Effect of pressure during sintering .....	81
4.5 Effect of prolonged ball milling.....	87

## CONTENT (Continued)

	Page
4.6 Influence of glycine .....	93
4.7 LTP-MnBi and Co composite .....	99
<b>V CONCLUSIONSION .....</b>	<b>106</b>
REFERENCE.....	109
APPENDIX .....	120
CURRICULUM VITAE .....	126



## LIST OF TABLES

Table	Page
3.1 List of the values of the parameters studies in this work .....	54
4.1 Magnetic properties of different pressure samples .....	84
4.2 Magnetic properties of MnBi using Mn griding time samples.....	90



## LIST OF FIGURES

Figure	Page
1.1 Mn-Bi phase diagram.....	4
2.1 Induction hysteresis loop.....	8
2.2 Shows the external magnetic field response of various magnetic materials .....	9
2.3 Schematic diagram of direction of diamagnetic materials.....	10
2.4 Schematic diagram of direction of paramagnetic materials .....	10
2.5 Schematic diagram of direction of ferromagnetic materials.....	11
2.6 Schematic diagram of direction of anti-ferromagnetic materials.....	12
2.7 Schematic diagram of direction of ferrimagnetic materials .....	12
2.8 Schematic depiction of domain wall and gradual change in dipole orientation across a domain wall.....	13
2.9 The magnetization process at each step is compared with the magnetization curve.....	14
2.10 The energy density $(BH)_{\max}$ at room temperature of hard magnetic materials increased during the twentieth century, as did the introduction of new materials with comparable energy density .....	15
2.11 Show the magnetic properties of rare earth elements with a high-performance device compared to the temperature .....	16
2.12 The magnetic properties of rare earth elements compared with MnBi .....	17
2.13 Critically matrix of permanent magnetic materials.....	18
2.14 A simulation of the magnetic separator process .....	19
2.15 XRD pattern of LTP-MnBi achive after low temp. low ball milling.....	21
2.16 Induction melting process .....	23
2.17 Coercivity curve $M_s$ and $H_c$ of MnBi at different jet milling pressures .....	24
2.18 MnBi phase weight ratio at various jet milling pressures.....	24
2.19 Demagnetization curve (b) $M_s$ and $H_c$ values for MnBi ball grinding function prepared.....	25

## LIST OF FIGURES (Continued)

Figure	Page
2.20 The relationship between magnetic properties at different temperatures the thumbnail shows the M-H loop hysteresis of MnBi material ball mill for 3 and 7 h .....	26
2.21 Melt-spinning process. ....	27
2.22 Coercivity value graph (demagnetizing curve) of crushed MnBi materials $H_c$ and $M_r$ $(BH)_{max}$ of crushed MnBi materials of different particle sizes.....	27
2.23 Chemical method .....	28
2.24 A schematic of the microstructure changes during LPS .....	30
2.25 The demagnetization value of temperature-dependent LTP-MnBi.....	31
2.26 Planetary mill (FRITSCH, PULVERISETTE (P7)).....	32
2.27 M-H curves of soft and hard magnet.....	34
2.28 M-H curves of soft and hard phase with exchange coupling magnet.....	34
2.29 Magnetic exchange spring: hard phase stiffness response of soft high magnetization phase in magnetic nano-composite.....	35
2.30 Intrinsic coercivity versus polarization of soft and hard magnetic materials. A closer look at high energy density NdFeB-type .....	36
2.31 XRD analysis of $Mn_{60}Bi_{40}$ material, The phase ratio under different preparation conditions.....	38
2.32 M-H curves, Magnetic properties, MnBi magnetic material $(BH)_{max}$ at 300 K.....	39
2.33 Demagnetization curves at RT for MnBi/Co NWs magnet with difference Co NWs contents .....	40
2.34 Demagnetization curves MnBi/Co NWs magnet.....	41
2.35 The hysteresis loop of MnBi, MnBi/Fe-Co (95/5 wt.%) and MnBi/Fe-Co (90/10 wt.%) .....	42
2.36 Demagnetization curves MnBi/NdFeB magnet with MnBi content at RT.....	42
2.37 The morphology of Co NWs by solvothermal method for 60 min (a) 200°C, (b) 225°C, (c) 250°C, (d) 260°C .....	43

## LIST OF FIGURES (Continued)

Figure	Page
2.38 The Hysteresis loop of Co NWs for 60 min at difference temperature.....	44
3.1 Photo of the vacuum sintering system with draw of the effusion cell.....	46
3.2 Raw materials of manganese and bismuth .....	47
3.3 The procedure for the synthesis of MnBi magnets starts with mixing Mn and Bi powders.....	48
3.4 Planetary mill process .....	48
3.5 Sieve screen process.....	49
3.6 M-H curves of MnBi composite with Co and each element of Mn-Bi-Co composite with an atomic ratio of 1:1 after sintering in a vacuum at 275 °C for 12 hours .....	51
3.7 M-H curves of MnBi composite with Co by vacuum sintering at 275 °C for 12 hours and MnBi ball milling at 300 rpm for 30 minutes with Co (no sintering).....	52
3.8 MnBi powder placement on bar magnets with a magnetic field of 0.5 T.....	53
3.9 Bragg's law of diffraction condition depicted as lattice planes.....	55
3.10 Sample placement for XRD measurements and sample holder.....	56
3.11 The fundamental diagram of a scanning electron microscope (SEM).....	57
3.12 The interaction area of the electron beam and the signal emitted from the specimen.....	58
3.13 Display during measurement of physical characteristics and chemical composition at various locations and Sample positioning within the SEM machine .....	59
3.14 A simplified diagram showing the components of the VSM and an inductive probe region diagram consisting of a sensing coil Sampling and sampling bars under an external magnetic field .....	61
3.15 Indicates the position of the sample measurement within the VSM.....	63
3.16 The optical layout of the BL3 beamline.....	64
3.17 XPS principle.....	66

## LIST OF FIGURES (Continued)

Figure	Page
3.18 Display during measurement of the chemical composition at the surface of the sample and (b) Sample positioning within the XPS system.....	82
4.1 Typical graph showing the relationship between vacuum pressure and temperature in the effusion cell during sintering. ....	69
4.2 MnBi ingot after sintering in vacuum. ....	70
4.3 Photo of Mn-Bi Sample after sintering in vacuum at 275 °C and a diagram showing the location on the ingot from where XRD patterns. ....	70
4.4 XRD curves are measured from magnetic powder MnBi, measured at the BL7.2W: MX optical beam system with two forms of incident X-ray radiation: ricochet (GIXRD) and pass-through (XRD).....	72
4.5 XRD patterns of MnBi powders after sintering in vacuum at 275 °C for 3, 6, 9 and 12 hours.....	73
4.6 Low- and (b) high-resolution SEM image and EDS spectra taken from two locations of MnBi powder after sintering in vacuum at 275 °C for 12 hours.....	74
4.7 M-H curves of 275 °C sintered Mn-Bi sample with different sintering durations. The insets show the maximum energy product (top-left) and coercivity and saturate magnetization (bottom-right).....	75
4.8 XRD patterns of MnBi at 275 °C for 12 hours with particle size of < 20 μm and 20-53 μm .....	77
4.9 XRD patterns of MnBi powder obtained after sintering in vacuum at 275 °C for 3 and 48 hours compared with database of MnBi, Bi and Mn phase .....	78
4.10 Shows the magnetic properties of MnBi particles size of < 20 μm and 20-53 μm .....	80
4.11 shows the maximum energy product $(BH)_{\max}$ of LTP-MnBi particles size of < 20 μm and 20-53 μm .....	81
4.12 XRD patterns of UHV-MnBi, LV-MnBi and AP-MnBi and Zoom in: 2-theta range of 34.5°-50.0°.....	82

## LIST OF FIGURES (Continued)

Figure	Page
4.13 M-H curves after demagnetizing field correction of UHV-MnBi, LV-MnBi and AP-MnBi. The inset of (a) shows the demagnetization curves of raw M ( $N = 0$ ) and correct M ( $N = 0.4$ ) of the UHV-MnBi (bottom-right). shows the maximum energy product ( $(BH)_{max}$ ) of all samples.....	83
4.14 Camera image (b) high-resolution SEM images (c) EDS spectra taken at MnBi region (black region) and (d) Bi region (white) of AP-MnBi ingot .....	86
4.15 The low-resolution SEM images of Mn ball milling 3 hours, 7 hours, 11 hours and 15 hours. The average Mn particle size are shown in the right figure.....	88
4.16 Shows the M-H curves of the sintered samples prepared using Mn powder particle from ball milling different time and magnetic properties of MnBi powder.....	89
4.17 XRD patterns of MnBi powders after sintering in vacuum at 275 °C for 12 hours the magnetization ( $M_s$ ) as a function of MnBi concentration. Red line shows the extrapolation of $M_s$ .....	90
4.18 XPS spectra of Mn ball milling for 3 hours and (b) MnO/Mn ratio with ball milling time.....	91
4.19 shown the distribution of the MnBi powder after sintering in vacuum after sintering in vacuum at 275 °C for 12 hours.....	92
4.20 XPS spectra of Mn ball milling different time and MnBi sample after sintering in vacuum at 275 °C for 12 hours .....	93
4.21 Morphology of glycine-added Mn powder in ball milling for 1 and 3 hours.....	94
4.22 The M-H hysteresis loop of the MnBi prepared from conventional ball milling (MnBi_M3) and the glycine addition for 1 hours (MnG <sub>1</sub> Bi) and 3 hours (MnG <sub>3</sub> Bi) .....	95
4.23 The XRD pattern of the MnBi-M3, MnG <sub>1</sub> Bi and MnG <sub>3</sub> Bi.....	96
4.24 XPS spectra of the MnBi-M3, MnG <sub>1</sub> Bi and MnG <sub>3</sub> Bi .....	97

## LIST OF FIGURES (Continued)

Figure	Page
4.25 The SEM images of the (a) MnBi-M3 and (b) MnG <sub>3</sub> Bi .....	98
4.26 Shows the M-H curves of the sintered samples prepared using Mn powder particle from ball milling for 3, 7 and 11 hours .....	100
4.27 M-H curves after sintering in vacuum of MnBi-M3, MnBi/Co-M3, MnBi/Co-M3-0.5T and Cobalt. The inset of shows the (BH) <sub>max</sub> of samples (Upper left). M-H curves after sintering in vacuum of MnBi-M7, MnBi/Co-M7, MnBi/Co-M7-0.5T and Cobalt. The inset of shows the (BH) <sub>max</sub> of samples (upper left).....	102
4.28 XRD patterns of MnBi/Co-M3, MnBi/Co-M7 and MnBi/Co-M11 and MnBi-M3, MnBi/Co-M3 compared with Cobalt .....	104

# CHAPTER I

## INTRODUCTION

### 1.1 Background and motivation

The permanent magnet has a key role in driving technology increasingly, such as motor/generators in electric vehicles and wind turbines, including the storage device etc. (Cao et al., 2018). This makes it an important part of the development of modern technology, which has led to the increasing demand for permanent magnets (Gutfleisch et al., 2011). The highly efficient permanent magnets have a high coercivity and remain magnetic even without any external magnetic field, causing those permanent magnets to have a high maximum energy product  $(BH)_{max}$  as well (Kramer et al., 2012; Liu et al., 2018). However, most high potential permanent magnets are synthesized from rare earth elements such as Nd-Fe-B and Sm-Co etc. Permanent magnets containing rare earth elements also have obvious disadvantages. They have low corrosion resistance and decrease magnetism with elevated temperatures. Meanwhile, the report found that the rare earth elements have a trend to a crisis in the supply and demand imbalance, that is, the demand is greater than the supply, and the mining to mine these rare earths can also result in environmental problems (Gutfleisch et al., 2011). As a result, research studies to find and develop rare earth free permanent magnets as a new alternative for the improvement of various technologies have begun. Despite the fact that, in theory, rare earth free permanent magnets have a lower energy product  $(BH)_{max}$  value than magnetic materials synthesized from rare earth elements (Poudyal et al., 2013). However, the problems and driving forces to drive various technologies make the search for permanent magnetic materials without rare earth elements very appealing, in which the choice of Mn element as the primary component becomes one of the potential options due to the five valence electrons of Mn element being unpaired (Patel et al., 2018), As a result, the energy of magneto-crystalline anisotropy has a high value and can be used in the synthesizing of many

metal compounds. When considering the price of magnetic materials, MnAl magnetic materials are inexpensive, which makes them especially attractive. Meanwhile, the magnetic properties report shows that the energy product  $(BH)_{\max}$  of the MnBi magnetic materials is higher than MnAl and MnGa magnetic materials (Kramer et al., 2012). This makes MnBi one of the rare earth-free permanent magnet materials with outstanding properties (Poudyal et al., 2016; Zhu et al., 2016; Dutta et al., 2016; Cao et al., 2011). It has a hexagonal structure with the arrangement of Nickel Arsenide (NiAs) form and the lattice value is  $a = 4.29 \text{ \AA}$  and  $c = 6.11 \text{ \AA}$ . It also has magneto-crystalline anisotropy up to  $1.6 \times 10^6 \text{ Jm}^{-3}$  (Kronmuller et al., 2014; Guo et al., 1992; Yang et al., 2001) caused by the effect of the spin-orbital interaction, a strong hybridization between Mn 3d and Bi 6p states and a high curie temperature value, including it has a higher coercivity with increasing temperatures, which shows that it has a positive temperature coefficient (Ma et al., 2016; Cui et al., 2014; Junjie et al., 2016; Chen et al., 1974; Zhang et al., 2011; Kharel et al., 2013; Saha et al., 2000; Yang et al., 2011; Yang et al., 2013; Yang et al., 2002). Hence, it is a permanent magnet material suitable for use at high temperatures. They are mostly used at an average temperature of about  $200 \text{ }^\circ\text{C}$  (Cui et al., 2014) in the application mentioned above. Because of the remarkable properties of LTP-MnBi magnetic materials, this makes coercivity values increase with increasing temperatures, but when the temperature reaches a certain point, the coercivity of LTP-MnBi is higher than that of Nd-Fe-B. The synthesis of MnBi magnetic materials can be studied for the optimum ratio from Bi-Mn diagrams in figure 1.1 (Cui et al., 2014), (Xie et al., 2016). In which, we know in the magnetic materials network that the MnBi magnetic materials can be divided into two phases as follows: in the first part, the synthesis of MnBi magnetic materials using a temperature higher than  $340 \text{ }^\circ\text{C}$  will have a phase transition to High Temperature Phase (HTP)-MnBi. On the other hand, if used below the temperature of  $340 \text{ }^\circ\text{C}$ , the phase transition is Low Temperature Phase (LTP)-MnBi (Narayan et al., 2016). The synthesis of MnBi magnetic materials in a practical way to obtain high purity and single phase can be very difficult due to the large difference in melting point between Mn ( $1,246 \text{ }^\circ\text{C}$ ) and Bi ( $271 \text{ }^\circ\text{C}$ ). As a result, the Mn in solid state is dissociated because of peritectic reaction (Cui et al., 2014). The

dissociated Mn will diffusely react with Bi in a liquid state, which will cause there to always remain Bi from the interaction. In the theory, the high purity and single-phase form of LTP-MnBi can provide a maximum energy product  $(BH)_{\max}$  value up to 17.7 MGOe (Cui et al., 2014), while in the experimental report, it has been reported that the maximum energy product  $(BH)_{\max}$  of its single-phase form and nanometer scale has exceeded 10 MGOe at room temperatures (Jihoon et al., 2014). However, the development of MnBi magnetic materials synthesis techniques has various techniques such as arc-melting (Li et al., 2018; Poudyal et al., 2016; Cui et al., 2014; Truong et al., 2015), rapid solidification (Nithya et al., 2013; Guo et al., 1990), chemical methods (Liu et al., 2018; Junjie et al., 2016; Kirkemind et al., 2011) and sintering techniques (Cao et al., 2018). The report found that the sintering techniques are simple methods for the synthesis process based on the diffusion of solid-state particles, causing the particles to bond together, making them suitable for commercial production due to their use of less time and energy than other techniques. Furthermore, it was also found that MnBi magnets prepared by sintering techniques still exhibited fewer magnetic properties than other techniques due to their purity and particle size. Each particle contains a magnetic domain which has magnetostatic energy (Yang et al., 2013). A single domain has a high static magnetostatic energy value, but if there is a subdomain of magnetism, the value of the static magnetism will be reduced due to the offset. Another important issue is that the purity content of MnBi magnetic materials is not enough because, after the synthesis interaction, there are other residual phases of Mn and Bi.

This research has a primary objective of developing the magnetic properties of MnBi magnetic materials compounds with vacuum sintering techniques and towards to high magnetic performance. The main interest is the development of the instrument for synthesized MnBi. The unique technique is sintering under pressure based on  $10^{-8}$  mbar. The reduction of Mn particle size and MnO is a challenge to improving magnetic performance. composite materials have been used as a hard phase magnetic material of LTP-MnBi for the induction with Co. The sintered materials will be characterized by X-ray diffraction (XRD), Scanning Electron Microscope & Energy

Dispersive x-ray Spectrometer (SEM & EDS), X-ray Photoelectron Spectroscopy (XPS), and vibrating sample magnetometer (VSM).

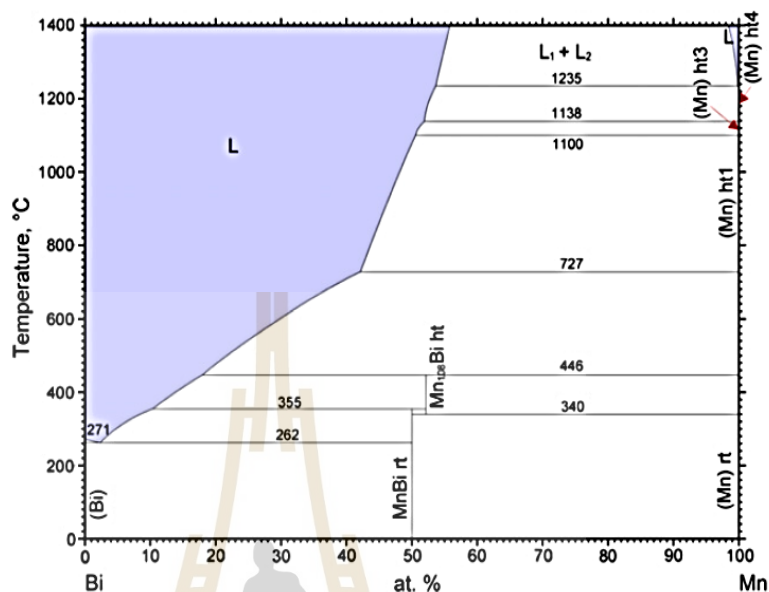


Figure 1.1 Mn-Bi phase diagram. (Cui et al., 2014).

## 1.2 Research objectives

The goal of this research is to synthesize low-temperature phase manganese bismuth (LTP-MnBi) magnetic materials and to understand the reaction mechanism that converts Mn and Bi into LTP-MnBi, including its hybridization with Cobalt. The LTP-MnBi was synthesized at 275 °C using vacuum sintering techniques under various conditions such as temperature control and hold times, particle size of materials (Mn particles powder and MnBi powder), pressure on magnetic properties of MnBi, influence of glycine addition on formation, effect of MnBi composite with Co, and the design and construction of an oxides reduction system to remove excess oxides for the high magnetic performance of LTP-MnBi. This technique was fabricated and improved at the Synchrotron Light Research Institute (SLRI), Nakhon Ratchasima province, Thailand. The work related to the characterization of the specimen was carried out to grasp the effect of various conditions with the investigated magnetic properties were measured using a VSM (Quantum Design, VersaLab) at VersaLab Laboratory, Department of Physics, Faculty of Science, Khon Kaen University, Khon

Kaen province, Thailand, examined the morphology and chemical composition via XPS and SEM & EDS at SLRI; and the analysis of the structure and phase of the sample using XRD at The Center for Science and Technological Equipment, Suranaree University of Technology, Nakhon Ratchasima province, Thailand. The effect of various conditions was methodically and discussed in this research.

### 1.3 Outline of the thesis

This dissertation is divided into five chapters as follows. The first chapter provides details of the introduction to the motivation, development, and application of permanent magnetic materials in this thesis. Chapter II presents the general information on manganese bismuth (MnBi), the discovery and development of the MnBi magnetic materials synthesis process, the relationship between oxide content and MnBi properties, and the study of MnBi composite with the Co element. Chapter III provides details of the fundamental and insight theories of magnetics; the techniques to produce MnBi magnetic materials; the theory and method for the dilution of the third element into MnBi magnetic materials; the development of the sintering in vacuum technique; and the experiments for the synthesizing and characterization of MnBi magnetic materials and MnBi/Co composites. Chapter IV presents the experimental results and discussions obtained during this thesis research. The primary task focuses on the development of a vacuum sintering system, the investigation of mechanisms for the magnetization of MnBi magnetic materials, the determination of the optimum condition, the studies and design, including the establishment of an oxide reduction system, and the investigation of exchange coupling of MnBi/Co composites. The main parameters investigated were particle size of MnBi particles, pressure, particle size of Mn powder prior to synthesis into MnBi form, and the effect of glycine addition during the Mn ball milling process. Finally, the conclusions, recommendations, and future approach of this research.

## CHAPTER II

### THEORY AND LITERATURE REVIEWS

This chapter explains the theory of magnetic materials, motivation, and literature reviews in this thesis. The primary task focuses on the magnetization, induction hysteresis loop, classification of magnetic materials, magnetic domain, properties of LTP-MnBi, the synthesis techniques for LTP-MnBi, dilution of LTP-MnBi magnetic materials with the third element, correlation between oxide content and MnBi properties, and the effect of hard and soft magnet composites.

#### 2.1 Magnetization

The magnetization ( $M$ ) is the indication value of the magnetic materials, that is, the magnetic moment per volume. It can be explained from the equation as follows:

$$\vec{M} = \frac{\vec{m}}{V}$$

When  $\vec{M}$  is Interaction between magnetic moment per volume of materials (cgs unit is emu/cm<sup>3</sup> and SI unit is A/m)

$\vec{m}$  is Magnetic flux (Wb)

$V$  is the area perpendicular with magnetic field lines (m<sup>2</sup>)

When a magnetic material is placed in an area with a magnetic field, as a result of magnetic moment response to the external magnetic field, the high magnetic field can be defined by the value of magnetic permeability ( $\mu$ ) as following. (Borsup et al., 2022)

$$B = \mu H$$

The area is in a vacuum condition, so that

$$B = \mu_0 H$$

When  $\mu_0$  permeability value in vacuum condition ( $4\pi \times 10^{-7}$  H/m)

When consider to the correlation between magnetic field (H), magnetic induction (B) and the magnetization (M) can be explained as following equation.

In the SI unit system, the magnetic induction is

$$\vec{B} = \mu_0 \vec{H} + \mu_0 \vec{M}$$

$$\vec{B} = \mu_0 (\vec{H} + \vec{M})$$

When  $\vec{B}$  is magnetic induction (Wb/m<sup>2</sup> or Tesla, T)

$\vec{H}$  is magnetic field (A/m)

$\vec{M}$  is magnetization (A/m)

While the CGS unit system as a show

$$\vec{B} = \vec{H} + 4\pi\vec{M}$$

When  $\vec{B}$  is magnetic induction (G)

$\vec{H}$  is magnetic field (Oe)

$\vec{M}$  is magnetization (emu/cm<sup>3</sup>)

## 2.2 Induction hysteresis loop and magnetic properties

The hysteresis is the effect of the response of the exterior magnetic field, causing magnetic induction to the nonlinear saturation point. When the magnetic field (H) increases to a certain point, it also increases the magnetization (M), but when reducing the magnetic field (H), the magnetization does not reverse to the original line. This can be explained by the B-H lines illustrated in figure 2.1. Starting at (0,0) is the starting point where no magnetic flux density exists. When increasing the magnetic field H, causing magnetization to keep increasing along the dotted line, there's not going to be a straight line along that line. After that, increase the magnetic field H to a point and the magnetic flux density B will reach the saturation point (point A). There will not be any more changes even if the magnetic field H increases. The saturation point is referred to as the saturation magnet ( $M_s$ ) (point A). When the magnetic field H is reduced, the magnetic flux density is also reduced, with the magnetic flux density decreasing along the curve from point A to point B. which clearly shows that there is still a pending magnetic flux density, so point B is called remanence ( $M_r$ ). And when the direction (opposite negative) changes and the magnitude of the magnetic field H

increases, the density of magnetic flux  $B$  decreases from point B to point C by this point called coercivity force ( $H_c$ ) which is the negative value of the magnetic field of a magnetic material. If a magnetic material has a high coercivity (wide loop), it is classified as a hard magnetic material, and if a magnetic material has a low coercivity (narrow loop), it is classified as a soft magnetic material. If the magnitude of the magnetic field ( $H$ ) continues to increase from point C to point D, saturation magnetization ( $M_s$ ) is the saturation point. In the opposite direction, with negative values. The magnetic field  $H$  is then reduced along the DE curve, and the remanence value ( $M_r$ ) at E, and then increased in the positive direction.  $H$  in the positive direction of the EF curve, there will be a coercivity force ( $H_c$ ) at point F. However, if the magnetic field  $H$  continues to increase, it will return to saturation point A again. The change of B-H curves is called the hysteresis loop (Kramer et al., 2012)

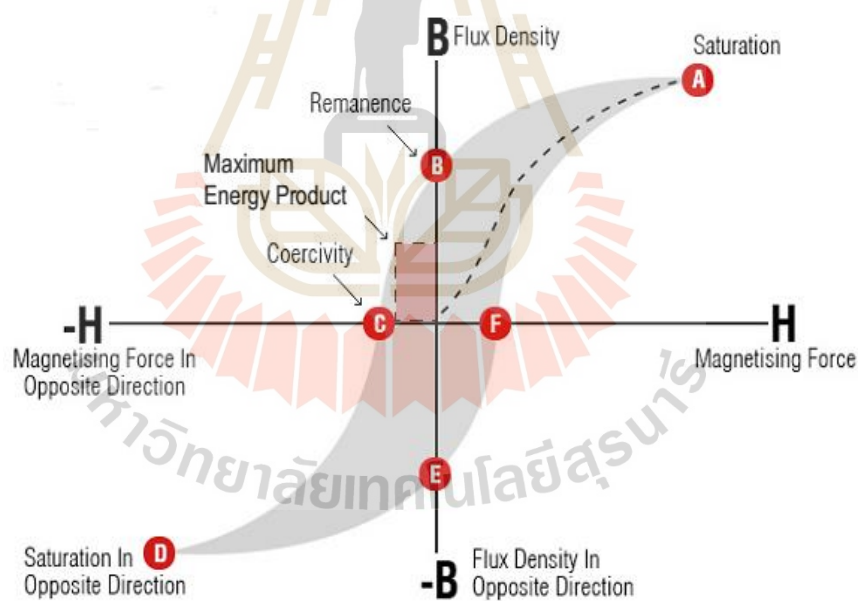


**Figure 2.1** Induction hysteresis loop. (Jha et al., 2015)

The hysteresis loops are graphs indicating the magnetic properties of each magnetic material or the energy storage capacity of the magnetic material (maximum energy product;  $(BH)_{max}$ ). That quantity can be obtained from the area under the graph

in the 2<sup>nd</sup> quadrant. If the area under the graph in the second quadrant is large, then the greater the accumulated energy in the magnetic material, is known.

## 2.3 Classification of magnetic materials

All magnetic materials can be classified as a function of their response to an external magnetic field as in figure 2.2.

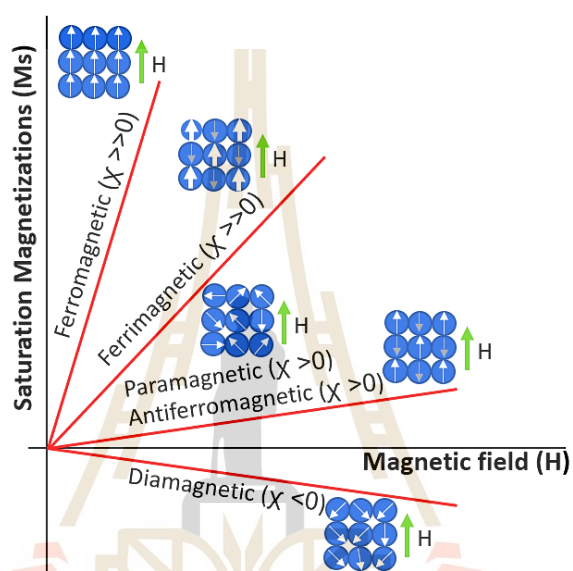


Figure 2.2 shows the external magnetic field response of various magnetic materials.

### 2.3.1 Diamagnetic materials

Diamagnetic materials are magnetic materials with weak magnetic properties (with very little strength compared with other magnets) as shown figure 2.3. Because diamagnetic materials exhibit magnetic value in the opposite direction to a magnetic field, their volume susceptibility ( $\chi$ ) value is very low, around  $-10^{-5}$ . The magnetic moment arrangement of diamagnetic is aligned in the opposite direction of the external magnetic field, which the correlation with the electron orbital around the atomic nucleus has incurred a loss of balance, resulting in a magnet in the negative direction. Therefore, the magnetic properties can occur in all magnetic materials, which the observations in materials with atoms that have only complete pairs of electrons, such as inert gases (He, Ne, Ar),  $H_2$ ,  $N_2$ , etc.

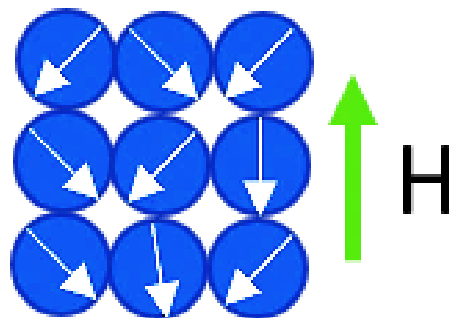


Figure 2.3 schematic diagram of direction of diamagnetic materials.

### 2.3.2 Paramagnetic materials

Paramagnetic materials are magnetic materials with a slight positive magnetic moment in each atom. There is very little interaction as shown in figure 2.4. The magnetic moment is not in arrangement thus the magnetic moment is in balance. For this reason, some magnetic moments offset each other. When the external magnetic field enters, the magnetic moment tries to align itself in the same direction as the magnetic field but will be the arrangement alignment takes place only a little. However, even though an external magnetic field is inserted, if in a state of high temperature, it will cause the magnetic moment to return to the same disordered arrangement due to the magnetic moment interaction of the paramagnetic material being small in the range of  $10^{-5}$ - $10^{-3}$ , such as Al ( $2.07 \times 10^{-5}$ ), Cr ( $3.13 \times 10^{-4}$ ) and Zr ( $1.09 \times 10^{-4}$ ) etc.



Figure 2.4 schematic diagram of direction of paramagnetic materials.

### 2.3.3 Ferromagnetic materials

Ferromagnetic materials are magnetic materials that have very high interactions between the magnetic moments of each atom, which is called the magnetic domain. When there is an external magnetic field, the magnetic moment is a result of an arrangement in a direction parallel to the magnetic field and continues to maintain its magnetic hold as shown in figure 2.5. even without a magnetic field to act upon. However, the magnetic properties of ferro are inversely proportional to the temperature. When the temperature is higher, the magnetic ferro will be reduced. Due to the thermal energy, as a result, the magnetic moment is disordered. The ferromagnetic materials are considered to have the strongest magnetic properties when compared with other magnetic materials, which have a very high response value between  $10^2$ - $10^4$ .

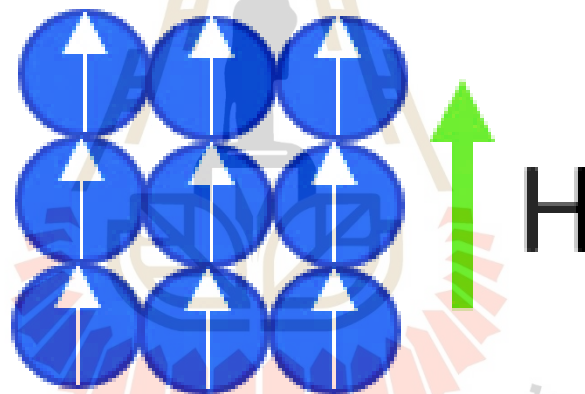


Figure 2.5 schematic diagram of direction of ferromagnetic materials.

### 2.3.4 Anti-ferromagnetic materials

Anti-ferromagnetic materials are magnetic materials with the magnetic moments of atoms arranged in an ordered manner. The magnetic moments of the atoms nearby are opposite as shown in figure 2.6. which causes the magnetic states to offset each other. So, antiferromagnetic magnetic materials are similar to paramagnetic materials. However, when considering the arrangement of the magnetic moment, you will find that there is a clear difference in that the paramagnetic material has a disordered arrangement. Therefore, when the external magnetic field  $H$  enters the magnetic moment of the magnetic material, the antiferromagnetic tries to align in the

direction of the H magnetic field, but the opposite alignment energy is very high. Thus, the arrangement of most magnetic moments follows a slight magnetic field.

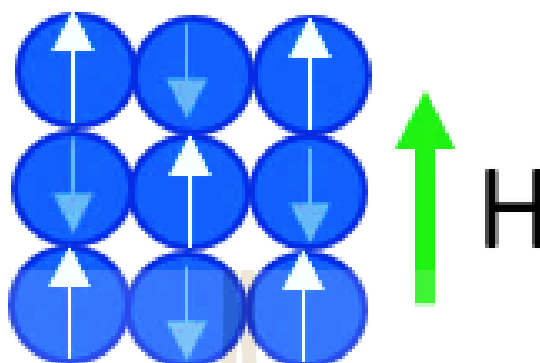


Figure 2.6 schematic diagram of direction of anti-ferromagnetic materials.

### 2.3.5 Ferrimagnetic materials

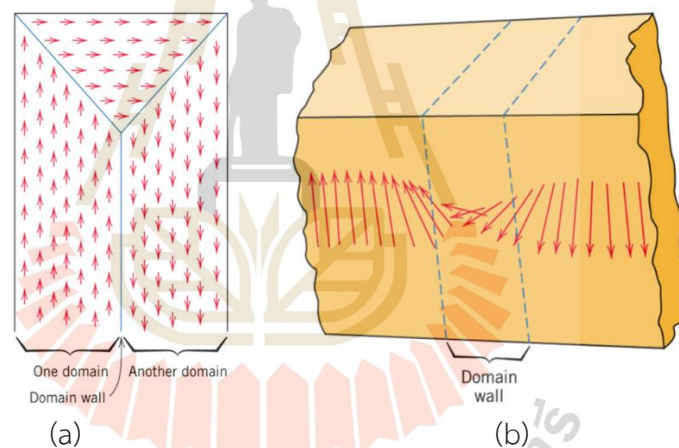
Ferrimagnetic materials are magnetic materials with properties similar to both ferromagnetic materials and antiferromagnetic materials. The ferromagnetic materials consisted of atoms of more than one element or ion. So, the magnetic moments of each atom are not the same. As a result, the offset is not equal to zero, causing the magnetic moment and the response to the magnetic field to produce a very positive value as shown in figure 2.7. Most ferromagnetic materials have dielectric properties. (สุปรีย์ดี พินิจสุนทร., 2558)



Figure 2.7 schematic diagram of direction of ferrimagnetic materials.

## 2.4 Magnetic domain

The magnetic domains are areas where the magnetic moments of the atoms point in the same direction throughout the area. They point out that a material, such as ferromagnetic materials, contains a large number of magnetic moments. The magnetic domains are in a saturated magnetic state, each magnetic domain is divided by a domain boundary, also called a domain wall, shown in figure 2.8. The interior of the domain has the direction of the magnetic state gradually modified as in figure 2.8(b). However, each magnetic domain is most stable when its total energy is lowest. The domain shape depends on the sum of the four energy types as follows: 1) exchange energy, 2) magnetostatic energy, 3) magneto-crystalline anisotropy energy, and 4) magnetoelastic energy are the four types of energy. (Nicola et al., 2011)



**Figure 2.8** (a) schematic depiction of domain wall and (b) gradual change in dipole orientation across a domain wall. (ธีระพงษ์ พวงมะลิ., 2015)

When an external magnetic field is applied to a magnetic material, the balance is upset. Consequently, the total energy of the system is unbalanced. This causes the domains to rearrange to achieve balance. Therefore, this process with the change of energy is referred to as the magnetization process.

The magnetization process is a process through which the ferromagnetic material is subjected to complete magnetization. It is the process of producing permanent magnets and the study of changes in the magnetic domain when exposed to an external magnetic field. This magnetization process consists of two parts: domain

wall motion and domain rotation. When the two parts are mixed together, the change in magnetization at each step can be explained by the magnetization curve as a figure 2.9. Initially, the magnetic materials were in a demagnetized state in which the sum of the magnetization of each domain was completely offset, making its net value equal to zero. When a magnetic field is inserted, the domain wall begins to shift slightly, but does not fall from the barrier. Hence, the initial M-H curve will have a very small slope. If the increasing magnitude of the magnetic field steadily increases until it falls out of the barrier, the walls of the domain move rapidly. Domain walls in motion whose domains are directed upwards and to the right have more power than other domains.

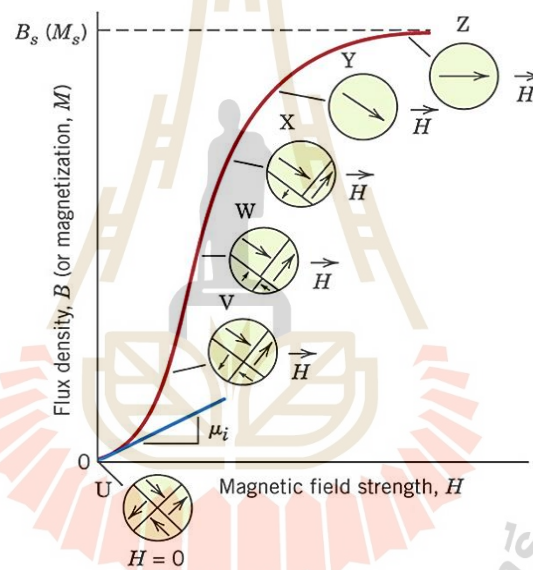


**Figure 2.9** The magnetization process at each step is compared with the magnetization curve. (ธีระพงษ์ พวงมะลิ., 2015)

Finally, the domain changes are diminished accordingly until no change occurs. This point is called saturation magnetic flux density ( $B_s$ ). When reducing the size of the magnetic field to zero, the M-H curves are reduced, but they do not follow the original path due to the residual magnetic within the magnetic materials. The investigation of the magnetic domain can be done using various techniques. Here we would like to briefly explain the principles of inspection by the magnetic force microscope (MFM) technique. It is a way to observe the magnetic domain with a magnetic force microscope using a sharp needle coated with magnetic material. The needle moves

along with the sample surface. The needle is subjected to magnetic force from the magnetic domain region. The MFM is a very high-resolution technique that can detect magnetic domains and some tiny magnetic nanoparticles.

## 2.5 LTP-MnBi compound

Many permanent magnetic materials were discovered in the last century. those magnets have been established and developed techniques to effectively production. The design of the apparatus using such magnets several active and inactive utilization makes the most of it. The energy product  $(BH)_{\max}$  is the main factor of the permanent magnets has been heightened, beginning from the steel provide the energy product about 1 MGOe which it has detected the first part, rising to about 56 MGOe for neodymium-iron-boron magnets during the previous ten to fifteen years show in figure 2.10. For this reason, the neodymium-iron-boron phase have high energy product enough for can be the produce in a commercially. (Mohapatra et al., 2018)

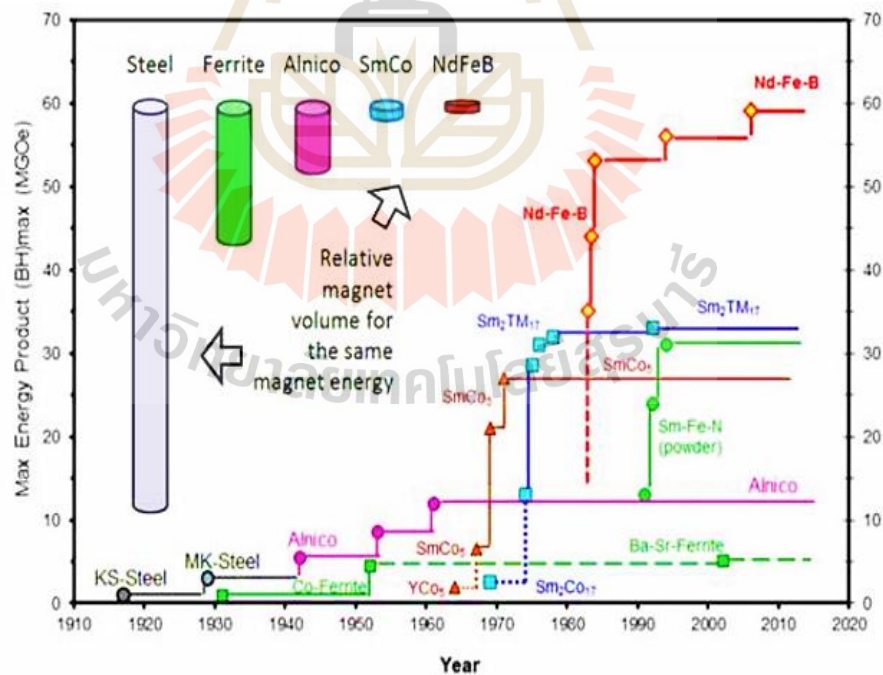


**Figure 2.10** The energy density  $(BH)_{\max}$  at room temperature of hard magnetic materials increased during the twentieth century, as did the introduction of new materials with comparable energy density. (Abdelbasir et al., 2019).

Permanent magnets can be used in many technological applications such as e-mobility, wind turbines and motor etc. The most of permanent magnets can applied to the motro/generator in a hybrid electric vehicle which this appcation is grow between 10-20 million in 2018 and the current are increase grow about 850 million vehicle are hybrids worldwide. the neodymium-iron-boron (NdFeB) this is the rare earth element, it is the difficult to be used at high temperature due to the magnetization reversal of the NdFeB at high temperature as demonstrate that in figure 2.11. However, if we want to use its at high temp and enough tempareture stability, we have to add another rare earth element, this is Dysposium (Dy) for the coating of grain boundary diffusion process but Dy more difficult to find in the nature than the Nd, Another problem of the rare earth element is crisis scarce in the global.

However, according to in a 2011, the report of Department of Energy US, the composition of rare elements, especially Nd and Sm which are rare earth elements in a supply crisis hav tend to increase. And in order to avoid this critical problem, it is imperative to find alternative permanent magnets free of rare earth elements. Challenging many group of researcher to pay attention to this problem. Hence, we can not longer use rare earth based permanent magnets in the future.

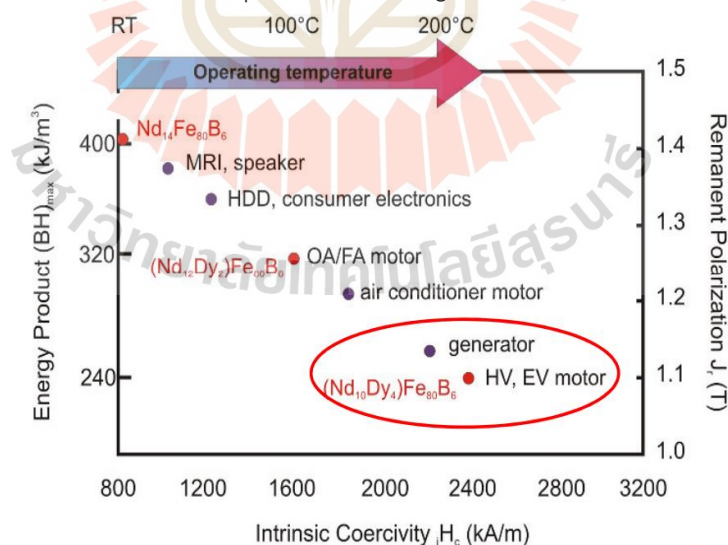


**Figure 2.11** Show the magnetic properties of rare earth elements with a high-performance device compared to the temperature. (Gutfleisch et al., 2011)

However, we are look to avoid utilization those rare earth materials and the find to the alternative materials such as rare earth free permanent magnets. In previous mention, in this research focusing on the MnBi based permanent magnets composite with Cobalt for increase the magnetic properties which as a show magnetic diagram in figure 2.12.

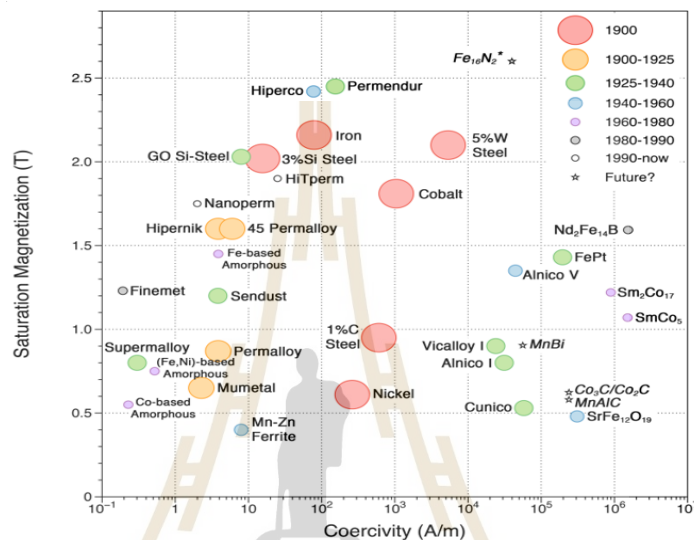


**Figure 2.12** The magnetic properties of rare earth elements compared with MnBi. (Antonov et al., 2020)

Rare earth permanent magnetic materials, such as Nd-Fe-B and Dy., have high magnetic properties at room temperature and can be widely used to produce high performance magnets for a variety of applications, including electric vehicles (electric bikes and electric bicycles, electric cars and hybrid cars, electric trains, electric planes, and electric buses, etc.), renewable energy sources (wind turbines, hydropower, photovoltaic, etc.), and future refrigerators (high performance refrigerators). (Cui et al., 2014). However, rare earth permanent magnetic materials have some disadvantages, such as the reduction of the low energy product  $(BH)_{max}$  with high temperature, poor corrosion resistance, and low curie temperature. The current state of the art of rare earth permanent magnets encounters the supply crisis, as shown in figure 2.13. As a result, rare earth free permanent magnets become appealing. (Bingbing et al., 2018).

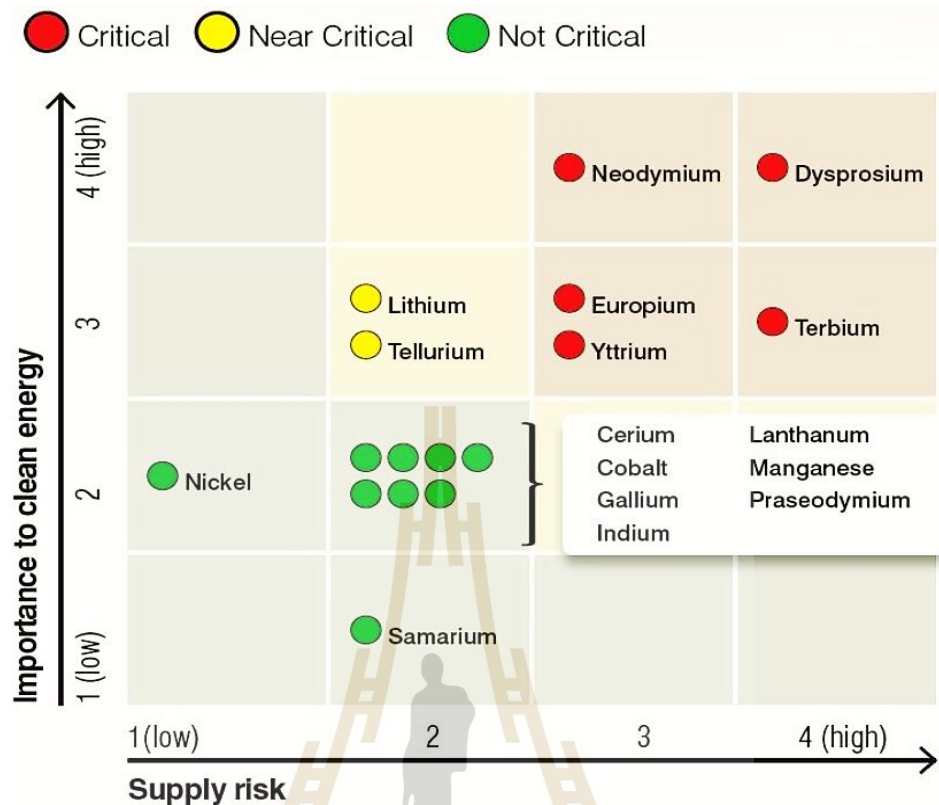
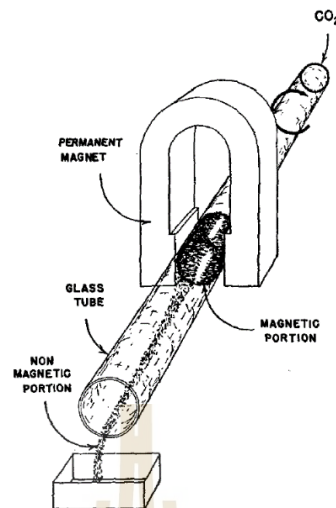


Figure 2.13 Critically matrix of permanent magnetic materials (Voncken et al., 2016).

Manganese bitmus (MnBi) was first detected as a permanent magnet by Adams' team, synthesized by thermal compression at 700 °C under a helium atmosphere for 5 hr. The furnace rotates at approximately 20 rpm, then cools down at 65 °C/h to 440 °C, stops spinning, and holds for 16 hrs. Subsequently, it cools down to 320 °C at 40 °C/h. At this temperature, the furnace is rotated 180° so that the semi-solid substance is at the top of the crucible. causing excess bismuth to drop to the bottom of the crucible. In this condition, it will hold for 8 hours and finally cool down to room temperature. The research team then grinded and separated the MnBi magnetic material by using a magnetic separator process as shown in figure 2.14, together with the formed MnBi magnetic material using low pressure (up to 3000 psi). Under the magnetic field to align the magnetic domains in the same direction, it was found that the coercivity value ( $H_c$ ) was 3.4 kOe, the maximum energy yield (BH) max was 4.3 MGOe, and the flux density was 4.3 MGOe. The residual magnetism ( $B_r$ ) is 4.3 kG. (Adams et al., 1952).



**Figure 2.14** A simulation of the magnetic separator process. (Adams et al., 1952).

MnBi has a glinting alternative to permanent magnetic materials due to its increase in coercivity with temperature, high curie temperature, high magneto crystalline anisotropy and promising hard phase materials for nanocomposite. (Cui et al., 2014). Moreover, it is challenging to synthesize MnBi because of the peritectic reaction between Mn and Bi. In addition, Mn reacts rapidly with oxygen. Thus, it is very difficult to obtain single phase MnBi. (Bingbing et al., 2018; Yang et al., 2002)

According to the research report, it is extremely difficult to synthesize LTP-MnBi magnetic materials for high purity and single domain in a practical manner. Due to the large difference in melting temperatures of manganese (melting point at 1246 °C) and bismuth (melting point at 271 °C). As a result, there may be a peritectic reaction between the two elements. The segregation of Mn is one of the main problems with the peritectic reactions. Various groups of researchers have invented and developed various techniques for the synthesis of high purity LTP-MnBi magnetic materials to increase their magnetic properties. There are many techniques that are regularly used in general, such as induction-melting, melt spinning, chemical methods, sintering, etc. (Cui et al., 2014).

### 2.5.1 Properties of LTP-MnBi

In 2014, J Cui et al. report that the development of MnBi magnets using the basic principles of as an exchange-coupled material, the first factor to focus on is the preparation of the MnBi compound to the highest purity. The first thing to understand

is the manganese and bismuth state diagram (Mn-Bi phase diagram) as shown in figure 1.1. It can be seen that the synthesis of MnBi magnets to achieve high purity and phase one is very difficult. Due to the relatively large melting point differences between Mn (1246 °C) and Bi (271 °C), there are currently a variety of techniques attempting to provide single-phase, high-purity MnBi magnets, such as induction melting. (Cui et al., 2014). Spin Forge (melt-spinning) (Yang et al., 2011), chemical process (Shoufa et al., 2018). and sintering (Borsup et al., 2022; Ngamsomrit et al., 2021). In addition to the synthesis of MnBi to achieve high purity, The uncomplicated synthesis method and consideration of the feasibility of industrial production are also areas of interest.

In 2016, Narayan et al. report that the effect of microstructure to enhanced energy product of MnBi sample. However, the preparation of a single phase of LTP-MnBi alloy is one of the major challenges due to the segregation of Mn from the reaction between Mn and Bi that is peritectic. The low-temperature low-energy efficaciously reduce particles and enhance the coercivity without significant drop in LTP-MnBi content. The XRD pattern of LTP-MnBi powder after low-temperature low-energy ball milling for 150 minutes found that the phase up to 96 % wt., result in to the increase of magnetic performance, the particle size of LTP-MnBi has average of 1-7 microns which the coercivity up to 12 kOe and the maximum energy product  $(BH)_{max}$  can able up to 8.4 MGOe whereof the bulk magnetic materials consist of the orientation uniform nanoscale of approximately 50 nanometer.

In January 2020, V.N. Antonov and V.P. Antropov report that the interaction to magnet of the hybridization between Mn 3d states and Bi 6p states which the large spin orbital coupling of Bi. However, the magneto-crystalline anisotropy depend on the temperatures can be describe taking relation the spin orbit interaction together with forceful coulomb electron-electron interaction. MnBi magnetic materials has exhibits a first order of the structural transition between the temperatures of 340 °C to 355 °C. The synthesized of MnBi magnetic materials via sintering technique have the mainly because of the segregate of Mn from Mn-Bi interaction below the peritectic temperature 446 °C. hitherto, the various methods have tried to avoid the segregation.

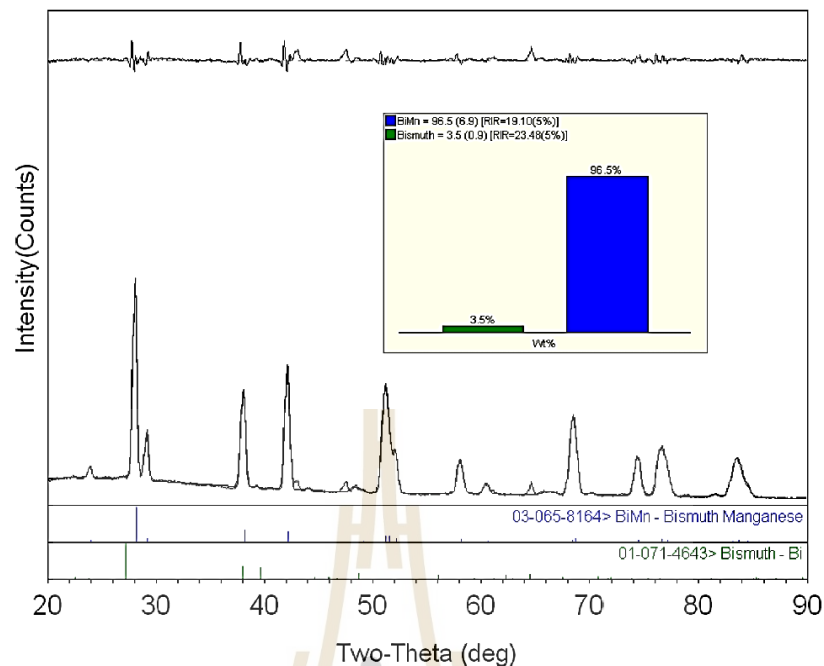


**Figure 2.15** XRD pattern of LTP-MnBi achieved after low temperature ball milling. (Poudyal et al., 2016).

MnBi magnetic materials, also known as low temperature manganese bismuth phase (LTP-MnBi), is a magnetic substance that exhibits ferromagnetic properties at low temperatures and paramagnetic properties at high temperatures. At room temperature (300 K), it has a hexagonal arrangement, Nickel arsenide (NiAs) has a  $P6_3/mmc$  lattice structure, with lattice parameters  $a = b = 4.29 \text{ \AA}$  and  $c = 6.13 \text{ \AA}$ . At low temperatures (20 K), MnBi magnets undergo a  $Cmcm$  transformation. At temperatures above 630 K, MnBi undergoes a manganese-bismuth phase transition to a high-temperature phase (high-temperature phase MnBi, HTP-MnBi), which has a  $Pm\bar{m}a$  (Cui et al., 2018) structure. Phase shifts in a wide range of temperatures. As shown in figure 2.16 from the schematic phase diagram, shows a phase change. Peritectic reactions and eutectic reactions occur over a range of temperatures as follows: 1. At temperature  $262 \text{ }^\circ\text{C}$  Liquid-rich Bi  $\leftrightarrow$  Bi + MnBi (eutectic reaction), 2. At temperature  $340 \text{ }^\circ\text{C}$  MnBi + Mn  $\leftrightarrow$   $Mn_{1.08}Bi$  (eutectic reaction), 3. At temperature  $355 \text{ }^\circ\text{C}$  Liquid-rich Bi  $\leftrightarrow$   $Mn_{1.08}Bi$  (peritectic reaction) and 4. At temperature  $446 \text{ }^\circ\text{C}$  Mn + liquid-rich Bi  $\leftrightarrow$   $Mn_{1.08}Bi$  (peritectic reaction) (Cui et al., 2014).

From the phase diagram above, it is possible to synthesize MnBi at temperatures above the melting point of Bi (271 °C) but lower than the HTP-MnBi formation temperature (340 °C). (Borsup et al., 2022) synthesized MnBi magnets by a vacuum sintering technique at 275 °C, 325 °C, and 375°C. It was found that LTP-MnBi formation can occur at this temperature range. The research team describes the mechanism of MnBi formation by the diffusion mechanism and drug interaction between Bi liquid and Mn particles greater than 100 nm and consisted of numerous cracks. After sintering at different temperatures, a white band was formed, indicating the MnBi layer. The thickness of the MnBi layer tends to increase with the sintering temperature. From the experimental results, the diffusion coefficient ( $D_c$ ) can be calculated by using the equation  $D_c = D_0 \exp(-E_a/KBT)$ . The activation energy ( $E_a$ ) was 0.45 eV, and the pre-exponential diffusion coefficient ( $D_0$ ) was  $5.33 \times 10^{-10} \text{ cm}^2/\text{s}$ . (Borsup et al., 2022).

Theoretically, single-phase MnBi magnets can yield a (BH) max as high as 17.7 MGOe (Mohapatra et al., 2018) at room temperature. While the part of the MnBi magnetic synthesis experiment to achieve high magnetic efficiency and obtain single phase particles is very difficult, this is due to the preparation technique and the control of variables such as the atomic ratio between Mn and Bi, atmospheric pressure during the synthesis process, and particle size, etc. The chemical process is the one that can synthesize high purity LTP-MnBi nanoparticles with very good magnetic properties. On the contrary, the disadvantage of this technique is that when there is a large demand for LTP-MnBi magnetic material, this is quite difficult. And most importantly, the chemical process is very costly, and the process is complicated. It requires a lot of expertise.

## 2.5.2 Synthesis Techniques for LTP-MnBi

### 2.5.2.1 Induction melting technique

It is a popular technique for LTP-MnBi magnetic materials because Mn and Bi are rapidly fused together via an electric arc under an inert gas atmosphere or a vacuum, as shown in figure 2.16, followed by annealing in vacuum and grinding to powder. The report of LTP-MnBi magnetic synthesis with this technique found that it can be to a purity of up to 98 wt.% (Bingbing et al., 2018), but the disadvantage of this

technique is that it requires many steps to use energy and is time-consuming for the synthesized.

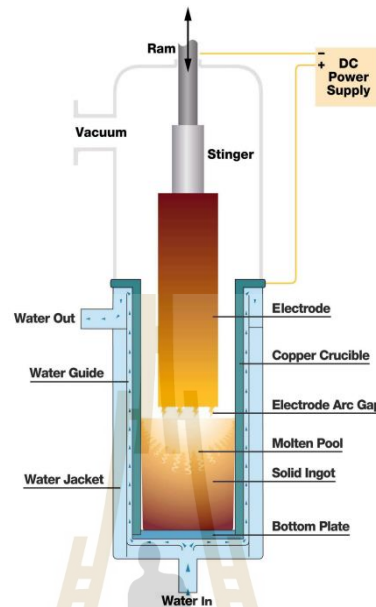


**Figure 2.16** Induction melting process. (Lopez et al., 2012)

In 2015, Rama Rao et al. conducted a study on how grinding processes affect particle size, MnBi phase formation, and magnetic properties. It was synthesized by the arc-melting technique under an argon atmosphere. This was followed by heat treatment at 300 °C for 24 h in a vacuum. to obtain a low-temperature phase MnBi magnetic substance. It was then made into powder by jet milling under pressures of 20, 40, 60, and 80 psi. The negative magnetic field ( $H_c$ ) was obtained as high as 1.8 T at the grinding process under 60 psi, the  $M_s$  value. In the range of 41-51 emu/g, the  $M_s$ ,  $H_c$ , and demagnetizing curves are shown in figure 2.17. From the high-speed grinding conditions, the powder under different pressures indicates that phase decay occurs. The smaller the size of the particles, which directly affects the magnetic properties. When the pressure was increased during the grinding process, the MnBi phase decayed to the Bi and Mn phases, where the percentage weight of MnBi was reduced from 81% to 43% as shown in figure 2.18. 80 psi rapidly shrinks particle sizes to about 1  $\mu\text{m}$ .

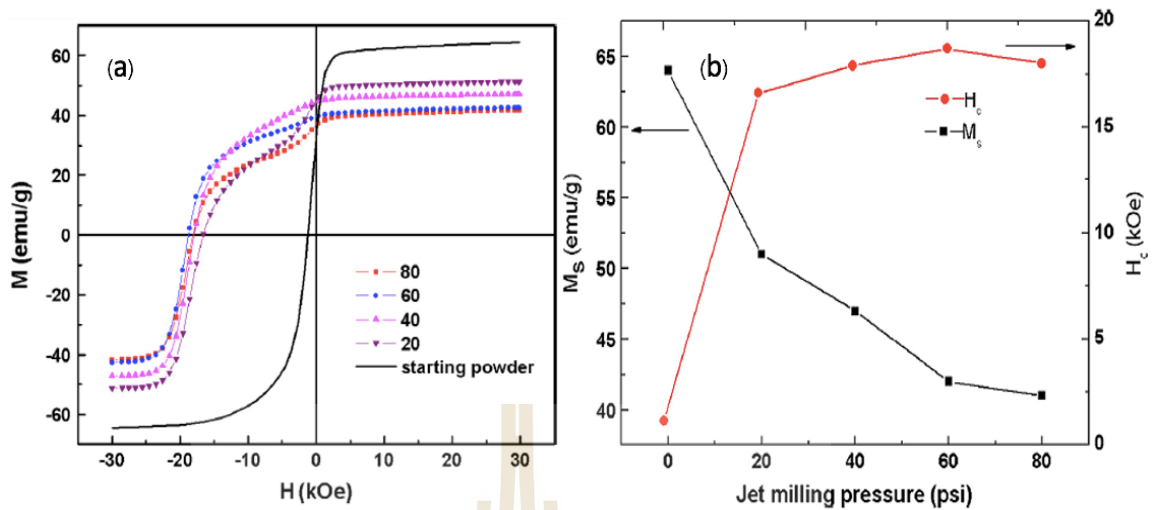


Figure 2.17 (a) Coercivity curve (b)  $M_s$  and  $H_c$  of MnBi at different jet milling pressures. (Antonov et al., 2015)

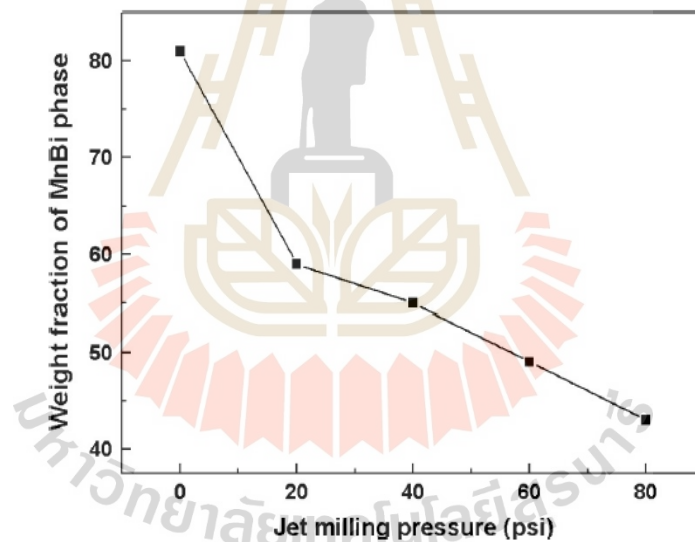
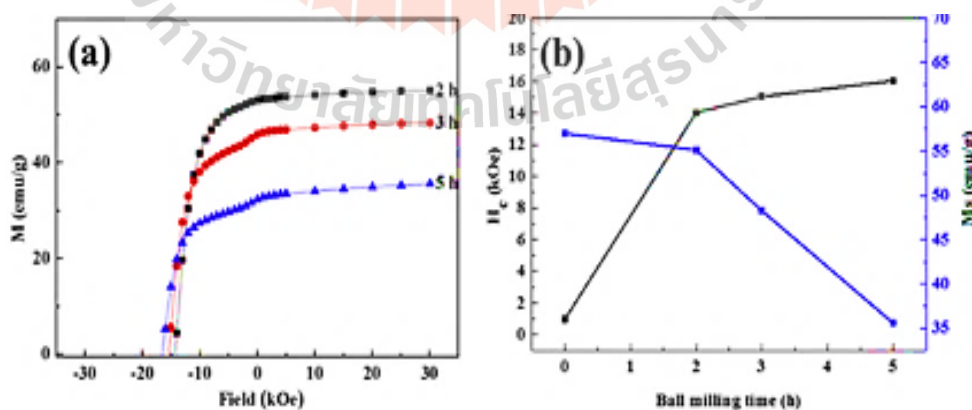


Figure 2.18 MnBi phase weight ratio at various jet milling pressures. (Antonov et al., 2015)

The following year, in 2016, Narayan Poudyal et al. synthesized LTP-MnBi magnets by arc-melting followed by heat treatment at 300 °C and crushing the LTP-MnBi magnetic powder down to approximately 1–7  $\mu\text{m}$ . The low energy ball milling method produces a degaussing value of up to 12 kOe and when the magnet is formed, the residual magnetic flux (remanence,  $B_r$ ) is 6 KG. The demagnetization value is up to 6.2 kOe and the maximum energy yield  $(BH)_{\text{max}}$  is 8.4 MGOe at room temperature. And

at 127 °C, the demagnetization increased to 16.2 kOe, the residual magnetic flux (remanence, Br) was 5.3 KG, and the peak energy yield  $(BH)_{\max}$  was 6.8 MGOe. The LTP-MnBi magnets are thermally stable in normal atmospheres at temperatures up to 200 °C. However, the ball milling process results in heat, which tends to decrease the  $M_s$  value (Poudyal et al., 2016)

In 2018, B. Li and colleagues synthesized MnBi magnets ( $Mn_{50}Bi_{50}$ ) by the arc-melting technique followed by ball annealing and grinding. The prepared magnetic bar was taken. Annealed at 573 K at different times and ball milling for 2–5 hours showed that the MnBi particles were significantly smaller in size. After 2 hrs of grinding, the MnBi particle size was approximately 2  $\mu\text{m}$  and after 5 h of grinding, the MnBi particle size was approximately 1  $\mu\text{m}$ . After that, the MnBi magnetic sample was mixed with epoxy resin and treated. The research team then took the material through various processes under a magnetic field of 1.8 T. To measure the magnetic properties, it was found that  $M_s$  of 55.1 emu/g,  $H_c$  of 14.1 kOe and  $M_r/M_s$  of 96.2% were obtained in 2019. Huang et al. prepared the  $Mn_{60}Bi_{40}$  alloy with the same technique. and heated under an argon atmosphere. After annealing at 535–613 K (262–340 °C) for 6–12 h, after grinding for 0.5–9 h, the magnetite sample had a  $H_c$  of 7.11 kOe at 300 K (27 °C). and  $H_c$  increased to 21.97 kOe when measured at 500 K (227 °C), as shown in figure 2.19.



**Figure 2.19** (a) Demagnetization curve (b)  $M_s$  and  $H_c$  values for MnBi ball grinding function prepared. (Li et al., 2018)

Y.B. Yang et al., investigated the structure and temperature-dependent coercivity ( $H_c$ ) of MnBi compounds by the arc melting process. It was found that the lattice parameter ( $c/a$ ) of MnBi magnets increased with increasing temperature and up to 1.433 at approximately 600 K and no structural phase change at 633 K. As shown,  $H_c$  tends to increase with temperature, reaching 2.5 T at 540 K and decreasing to 1.8 T at 610 K, as indicates an increase in  $H_c$ . This research indicates that magneto crystalline anisotropy increases with smaller MnBi size (Yang et al., 2013) shown in figure 2.20.

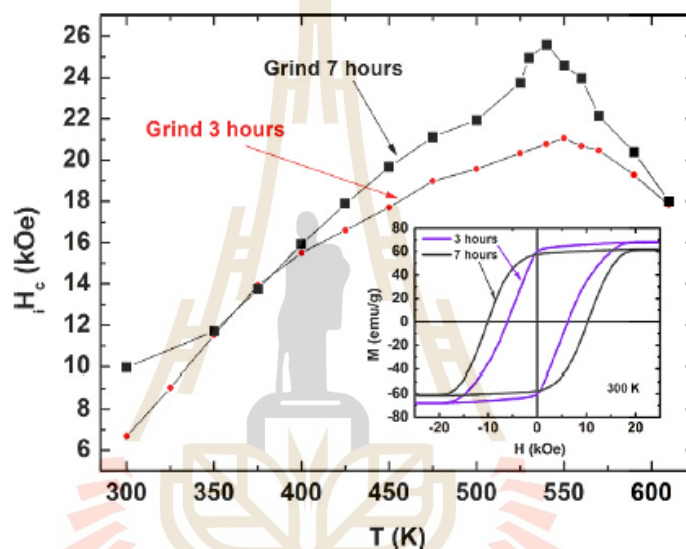


**Figure 2.20** The relationship between magnetic properties at different temperatures the thumbnail shows the M-H loop hysteresis of MnBi material ball mill for 3 and 7 h. (Yang et al., 2013)

### 2.5.2.2 Melt spinning technique

It is a technique that fuses Mn and Bi first and then injects them onto a rotating copper wheel that has been cooled to allow for rapid coagulation. This technique can reduce the segregation of Mn while it is synthesized. As a result, there is almost no residue of Mn due to the control of a reasonable cooling rate. As a result, the purity is up to 95 wt.%. The disadvantage of this technique is that the LTP-MnBi magnetic synthesis is relatively small and difficult enough to be applied at the industrial level.

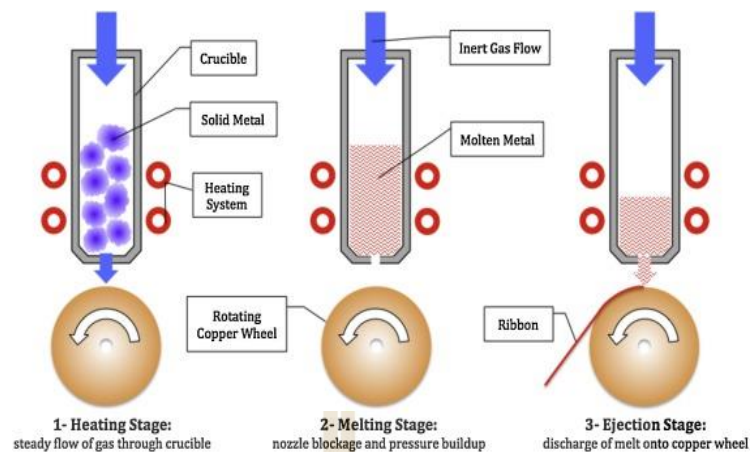


Figure 2.21 Melt-spinning process. (Shizadi, A.A. et al., 2019)

In 2017, Sumin Kim et al. synthesized MnBi magnets by the spin melting technique, followed by cold compression, annealing, magnetic separation, and grinding to smaller sizes at different times. The reduction of the MnBi particle size was carried out using planetary milling and jet milling. By ball milling, the grinding time was 1, 2, and 2.5 hours. The speed was 150 rpm, and jet milling were performed at a pressure of 0.34 MPa under a nitrogen atmosphere. The crushed MnBi powder was forged by 650 MPa compression under a 2 T magnetic field, in an argon atmosphere at room temperature. As shown in figure 2.22, the sample was measured for magnetic properties.

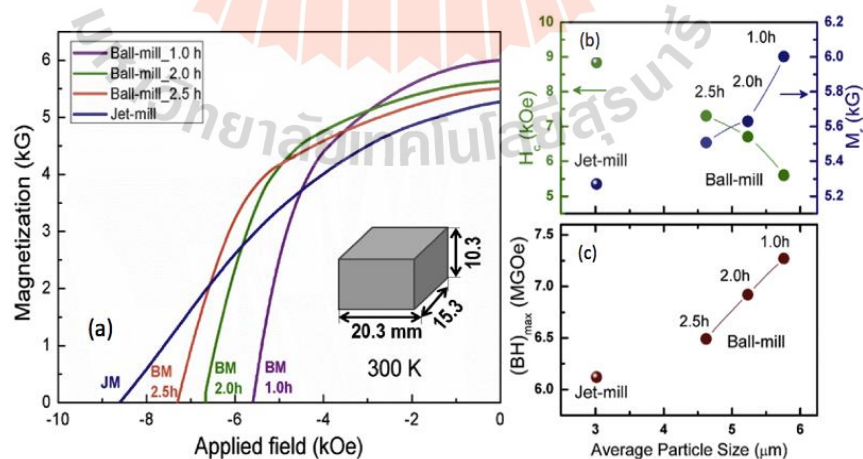


Figure 2.22 (a) Coercivity value graph (demagnetizing curve) of crushed MnBi materials; (b)  $H_c$  and  $M_r$  (c)  $(BH)_{\text{max}}$  of crushed MnBi materials of different particle sizes. (Kim et al., 2017).

### 2.5.2.3 Chemical method

A method for the synthesis of LTP-MnBi magnetic materials is obtained by obtaining the magnetic properties closest to the theoretical values. The chemical process is one of the most flexible and versatile methods that can synthesize the precursor to particles at the nanometer level before mixing, as shown in figure 2.23, which can generate LTP-MnBi magnetic substances at the nanometer level and have a very high purity. This results in very good magnetic properties. Using complex mechanisms for chemical synthesis, such as mechanochemical processes, liquid chemical processes, and metal redox synthesis, etc. However, because of the chemical complexity and processes involved, considerable expertise is required in the manufacture of LTP-MnBi magnetic compounds. In this way, it is quite expensive and can be obtained in small quantities. Therefore, it is not suitable for commercial production.

In 2014, Rama Rao et al. reported the synthesis of MnBi magnets with sizes in the 100-300 nm range by mixing  $\text{Bi}_2\text{O}_3$  with Mn powder and using Ca as a catalyst in a mechanistic process ( $\text{Bi}_2\text{O}_3 + 2\text{Mn}$ ). This process produces a magnetic substance ( $+ 3\text{Ca} = 2\text{MnBi} + 3\text{CaO}$ ). It was grinded using a planetary mill under an argon atmosphere for 4 h and then annealed in two steps as follows: annealed at 1075 K for 10 min, and then reduced to 575 K was held for 15 hours, then reduced to room temperature. The samples obtained after curing were washed off with DI water, ethanol, and acid. The magnetic properties of the samples were then magnetically aligned at a magnetic field of 80 kOe. MnBi magnets the prepared nanoparticles had a negative field value (coercivity,  $H_c$ ) up to 16.3 kOe (Zhang et al., 2015).

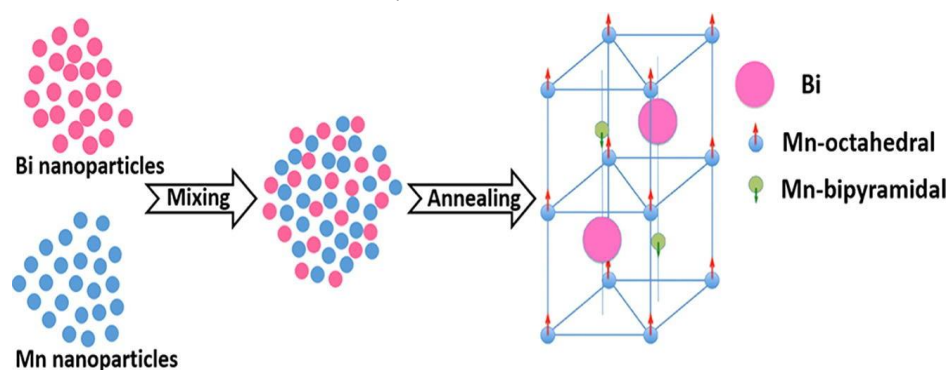
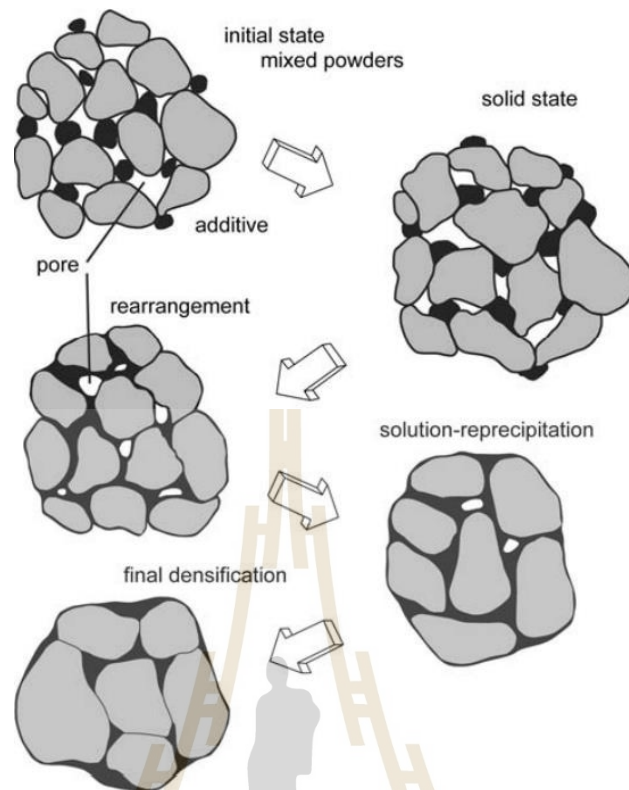


Figure 2.23 Chemical method. (Liu et al., 2018).

#### 2.5.2.4 Sintering technique

It is an LTP-MnBi magnetic synthesis technique based on particle bonding and the diffusion process shown in figure 2.24. The sintering technique can be classified into four categories as follows: (1) solid state sintering, in that case, the substance will stay in a solid state throughout the process. (2) Liquid phase sintering: a substance in a liquid state combined with a substance or mixture in a solid state. (3) Viscous sintering, the reactive sintering is in liquid form and has a high ratio. This type of sinter has a surface tension factor relative to its density, shape, and size. And the last type is transient liquid phase sintering, the start of substances contained in a liquid state and then to complete the solid state. In which, vacuum sintering techniques are a simple synthesis process. It has small steps and low power consumption, as shown in figure 2.24, and is suitable for industrial applications.

In 2002, Yang's research team developed and improved the synthesis of LTP-MnBi magnets by sintering under an argon atmosphere at 1000 °C for 1-10 h, then cooling to room temperature, grinding to a powder, followed by magnetic separation to increase the MnBi phase ratio. Oriented the magnetic domains and formed a permanent magnet under a magnetic field of 10 kOe in epoxy resin. It was found that at 127 °C, the LTP-MnBi magnetic substance had a  $(BH)_{max}$  of 4.6 MGOe and a  $H_c$  of up to 20 kOe, as shown in the figure 2.25 and at room temperature,  $(BH)_{max}$  was 7.7 MGOe, and  $H_c$  was 14 kOe. The development of MnBi magnetic properties occurred through the synthesis process. The research team pointed out that synthesizing pure MnBi is quite difficult.



**Figure 2.24** A schematic of the microstructure changes during LPS. (German et al., 2009)

It was found that a peritectic reaction between Mn and Bi occurred during the synthesis. The traditional synthesis process (casting at high temperatures) will result in the precipitation of Mn from liquid Bi, resulting in partial diffusion of Mn or Bi to become MnBi. However, the process of obtaining pure MnBi (single phase) is very challenging. due to a peritectic reaction. The dissociation between MnBi and Bi includes oxide formation. During the synthesis, Currently, the method of separating the contaminated phase from MnBi magnets is through magnetic separation. Using this method, the purity of the synthesized MnBi has been found. It has been reported to have a purity of up to 90% (Yang et al., 2002).

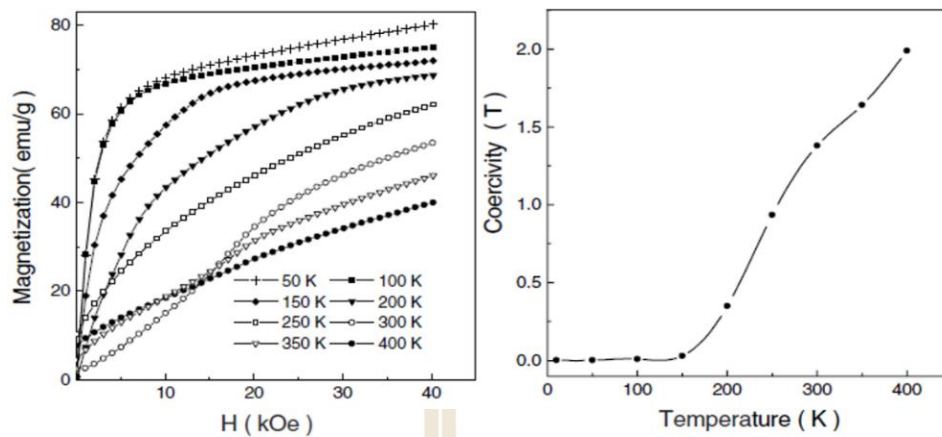


**Figure 2.25** The demagnetization value of temperature-dependent LTP-MnBi. (Yang et al., 2002)

In addition, in 2018, Cao and colleagues synthesized LTP-MnBi magnets using spark plasma sintering (SPS) technique in an argon atmosphere. This was followed by heat treatment at 673 K for 30 min in a vacuum. After that, fine grinding at 0.5–28 h at a speed of 200 rpm showed that the proportion of LTP-MnBi was as high as 86.91 wt.%,  $H_c$  was 7.11 kOe,  $M_s$  was 26 emu/g, and the  $(BH)_{max}$  value is 1.53 MGOe at room temperature [b5]. However, many research groups are currently trying to find new techniques to synthesize MnBi magnets with high purity and efficacy. permanent magnets with theoretical values as close to those used today (Cui et al., 2014).

However, literature reviews revealed that magnetic properties are not as good as the previously mentioned techniques. Consequently, it is necessary to develop this technique in order to obtain magnetism performances comparable to other techniques. The contamination of excess material remaining after the synthesis process or decreased purity of excessive substitution, particle size, and chemical interactions such as oxidation on the surface, are the primary factors affecting the magnetic properties of the preparation using vacuum sintering techniques. For these reasons, many groups of researchers have tried to investigate the effects and develop this technique for increasing the magnetic properties of LTP-MnBi magnetic materials. In the first part, we try to purify the LTP-MnBi magnetic materials by separating the excess of Bi from the LTP-MnBi magnetic material via the magnetic field [ref.] Due to the Bi element's diamagnetic materials, reduce particle size using the ball milling method.

The ball milling method can be divided into seven types: (1) ball mill (2) attrition mill (3) jet mill (4) vibration mill (5) pendula mill and (6). Muller mill [ref]. In the first case, it is the material grinding by using the rotary principle of the mill, which has a ball inside. This type of grinding can be performed both by dry milling and wet milling as shown in figure 2.26. The attrition mill method is a very fine grinding technique with a very low distribution of particles. The particle size of this technique is less than 1 micrometer. The Jet mill method is a grinding method based on the principle of grinding materials in which the materials are moving at a very high speed. In this kind of grinding, balls are not used. The next case is the vibration mill method. It is a grinding tool that relies on the vibration of a magnetic bar that is used to grind and the bumps into the desired material, including the grinding of the material itself. The Pendula mill method is a dry mill using the hammer head to strike horizontally parallel to the ground. And the last case is the Muller mill method. It is grinding using a large stone or steel wheel spinning along a large tray. The weight of the wheel crushed material to a smaller size.



**Figure 2.26** Planetary mill (FRITSCH, PULVERISETTE (P7)).

In 1951, Par M. Charles GUILLAUD, and in 1952, EDMOND ADAMS et al., the study of a new permanent magnet from manganese bismuth magnetic materials. Heusler reported the ferromagnetic nature of manganese bismuth in 1904, which was confirmed by Arrivaut in 1905, and Bekier in 1914 considered information of probable manganese bismuth phase, which was produced of MnBi at 445 °C by the reaction of a kind of crystalline form at 597 °C out of the molten alloy shown in figure 3. In 1912,

Hilpert and Dieckmann also noted the strong ferromagnetic of MnBi alloy at 360-380 °C of curie temperature.

### 2.5.3 Dilution of LTP-MnBi magnetic materials with third element

The study of the LTP-MnBi magnetic preparation was carried out by the arc-melting technique, followed by annealing and ball milling, and then doped with the third element such as NdFeB, Al, and Cu, etc., and found that the change in the proportion of LTP-MnBi particles was small. Meanwhile, the magnetic interaction between Mn atoms in the crystal structure of Mn atoms inserted into a crystal structure (interstitial Mn) has a tendency to decrease. The report on the addition of a third element into LTP-MnBi powders discovered that doping LTP-MnBi with rare earth elements results in improved thermal stability. The results also found that the dilution with C, Fe, Ni, B, Hf, Tb, and Sm elements into a LTP-MnBi powder prepared by the melt-spinning technique, the coercivity value has a tendency to decrease, but the ignored doping with Hf element makes the coercivity value increase. The application of LTP-MnBi magnetic materials may not be suitable due to the relatively low energy product value and problems with environmental degradation resistance. Therefore, the challenge for researchers in many groups is to develop LTP-MnBi particles that are more effective, which makes them suitable for applications in a wide variety of conditions. In the future, they may use MnBi magnetic materials as a component, which has adopted the magnetic exchange coupling principles as a guideline for the development of magnetic material composites. It is a technique for preparing a suitable combination of two magnetic materials, where the first is a material called soft magnetic materials. It is a magnetic material that easily induces and demagnetizes in a magnetic state and shows that the M-H curves have a small loop with a low coercivity value. As shown in figure 2.27, the second type of magnetic material that is difficult to induce magnetism or demagnetization has a relatively high coercivity and remanence value. (ประยูร ส่งสิริฤทธิกุล., 2020)

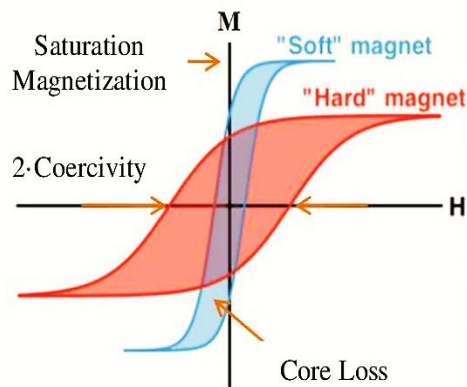


Figure 2.27 M-H curves of soft and hard magnet. (Martone et al., (2017).

The combination of hard magnetic materials and soft magnetic materials results in higher energy yields. It is understood that hard magnetic phase materials can coercivity value increase and soft magnetic phase materials can increase the magnetization. This combination is called a soft and hard magnetic composite or exchange magnet, as shown in figure 2.28.

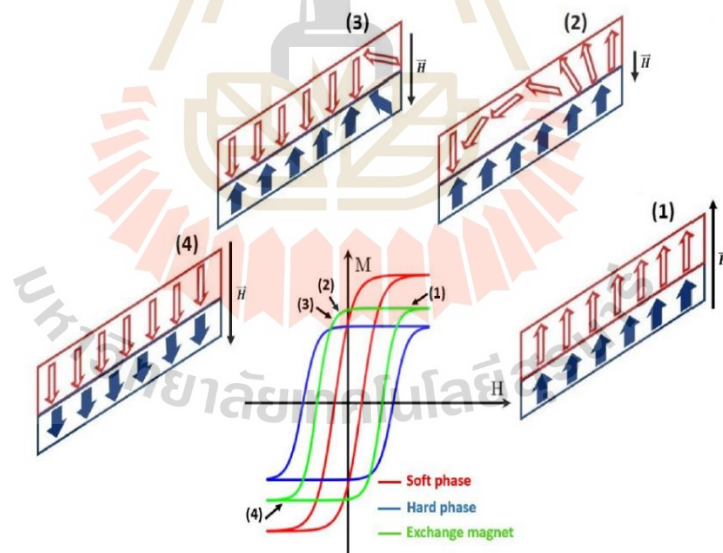
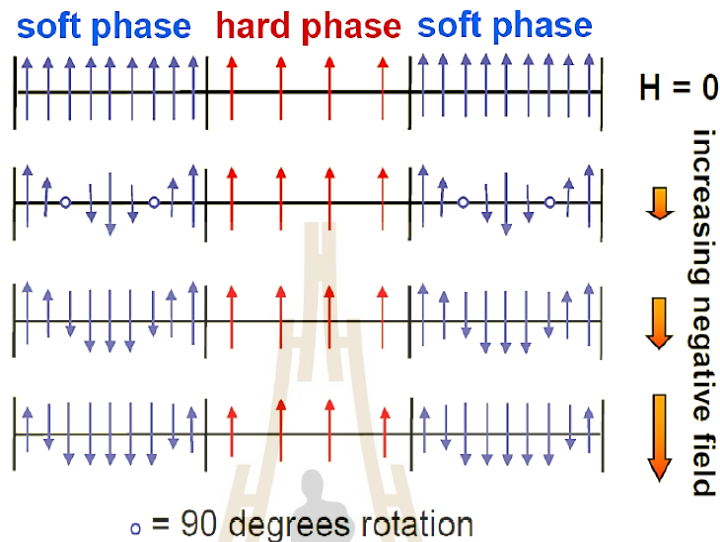


Figure 2.28 M-H curves of soft and hard phase with exchange coupling magnet. (Sabet et al., 2018).

The exchange spring concept has the need for the soft phase to be sufficiently small such that domain walls do not form in it. It is toward magnetic turnaround. There is the critical thickness for the soft phase, which should be about twofold the width

of domain walls in the hard phase. The smaller the hard phase, the larger the volume fraction of the soft phase, and thus the larger the magnetization and the energy product.



**Figure 2.29** Magnetic exchange spring: hard phase stiffness response of soft high – magnetization phase in magnetic nano-composite. (Li et al., 2017)

The magnetic materials are classified as soft magnetic materials such as Fe, Ni, Si, Al, and Co, etc. According to the study, when MnBi magnetic materials are mixed with a soft magnetic phase like cobalt, which among the various soft magnetic materials, Cobalt is an excellent material for improving the magnetic properties of MnBi. According to a research paper on composite magnetic materials, MnBi/Co is a permanent magnetic material with a higher  $(BH)_{\max}$  than LTP-MnBi (Nguyen et al., 2017). the energy product increases with the compared MnBi particles. However, the development of synthetic materials on the nanoscale and research studies are still needed to obtain appropriate methods and proportions. There will be a magnetic interaction between the hard-magnetic phase and the soft magnetic phase in order to obtain the theoretical  $(BH)_{\max}$  value.

The magnetic materials have been developed until now for the commercial field. The permanent magnet was made from neodymium, which is the rare earth element. It is known that the neodymium magnet is difficult to use at high temperatures. However, if we want to use it at a high temperature, we must add

another rare earth element. This is dysprosium to reduce the magnetization reversal of the grain boundary diffusion process by the coating, but dysprosium is more difficult to find in nature than neodymium (inserted in figure 2.30) due to a report that the large mines in China found that the excavation Dy has very low content (Gutfleisch et al., 2011). When it comes to applications for permanent magnetic materials, it can be used in electric machines that require a high saturation magnetization and a low coercivity value. Most of the soft magnetic materials have a coercivity value of lower than 1 kA/m and the hard-magnetic materials have a coercivity value of up to about 2800 kA/m as shown in figure 2.30.

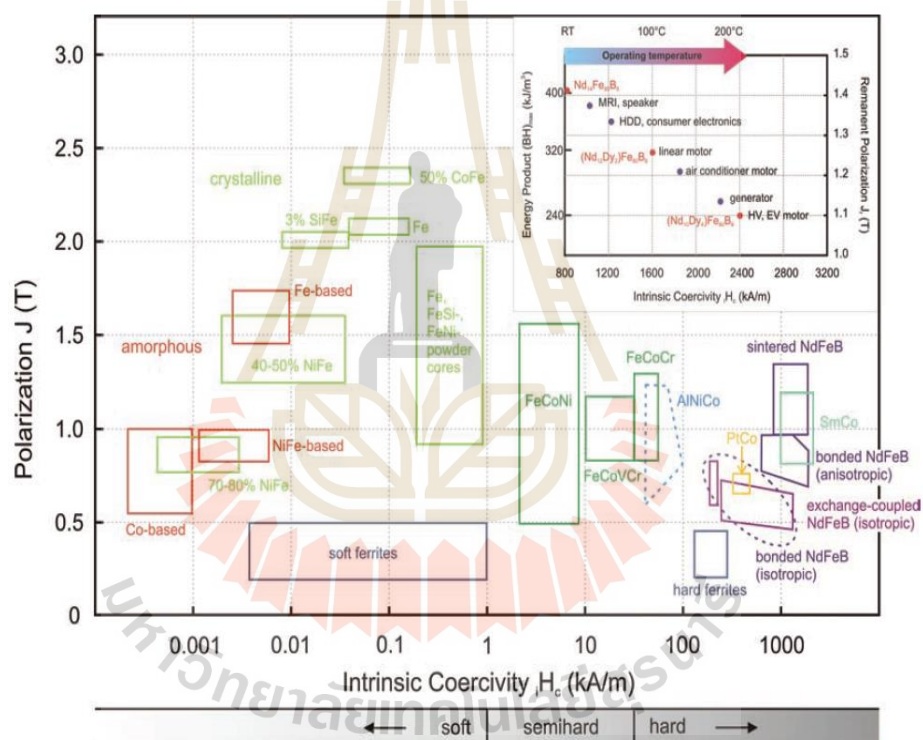


**Figure 2.30** Intrinsic coercivity versus polarization of soft and hard magnetic materials. A closer look at high energy density NdFeB-type magnets is shown in the inset. (Gutfleisch et al., 2011).

#### 2.5.4 Relation between oxide content and MnBi properties

The synthesis of MnBi magnets depends on many factors to achieve high magnetic efficiency. And since the large melting points between Mn and Bi are 1519 K and 544 K, respectively, the manganese-bismuth phase diagram (Mn-Bi phase diagram) has to be studied. There is also a eutectic reaction at 535 K. This reaction has a rather

limited high temperature. Although this eutectic temperature is approximately 473 K higher than the required temperature, it is a relatively low temperature. In practice, large quantities of Bi-containing sample powder are used for typical high-volume magnetic synthesis methods, such as sintering and thermal compression. As a result of the peritectic reaction, when the magnetic synthesis temperature of MnBi is higher than the eutectic temperature of 535 K, part of the MnBi is converted to an excess of Bi liquid. It may react with the Mn atoms in the liquid, resulting in manganese oxide (MnO) forming. Even in the lower temperature hydrogen atmosphere, MnO can revert to Mn metal. 535K (Antonov et al., 2020). It has been shown that MnBi compounds are sensitive to oxygen and temperature. Oxygen is one of the variables causing the decay of the MnBi phase at temperatures above 473 K. When MnBi decays, the remaining Mn reacts with oxygen to form MnO, resulting in a loss of magnetic properties. Conversely, if the synthesis temperature is above or below 473 K, MnBi is stable. As observed from the Mn-Bi phase diagram, in addition, if the MnBi magnetic synthesis process can control the oxygen content, it will stabilize the magnetic substance up to 473 K. (Cui et al., 2014)

J. Cao et al. MnBi was synthesized by the spark plasma sintering technique under an argon atmosphere. followed by annealing at 673 K for 30 min, and finally ground to powder. When the magnetic properties were measured, it was found that the suitable samples The coercivity ( $H_c$ ) was 7.11 kOe, the residual magnetism (remanence,  $M_r$ ) was 26.0 emu/g, and the maximum energy product  $(BH)_{max}$  was 1.53 MGOe at room temperature. When X-ray diffraction was analyzed, it was found that the synthesized MnBi sample consisted of four components: LTP-MnBi, Bi, Mn, and MnO. (Cao et al., 2014)

The study of the crystal structure by the X-ray diffraction (XRD) technique can be calculated from the Rietveld refinement method and compared with the experimental results of the MnBi magnetic material. It is found that the magnetic material contains the LTP-MnBi, Bi, and Mn phases. A small amount of the MnO phase was also found. As shown in figure 2.31(a), and from figure 2.31(b), it is clear that the phase content of LTP-MnBi magnetic material with increasing grinding time resulted in a significant decrease in LTP-MnBi phase content. Importantly, while the phase content

of Bi and MnO has been directed towards increasing, it is known that the Mn phase and Mn atoms in LTP-MnBi magnetic materials are easily oxidized and form MnO. It is an inevitable variable in ball milling and sintering processes. In general, the Bi and Mn phases are left over from the forming and decomposition reactions of the LTP-MnBi phases. It is a non-magnetic phase, so if residual in a large quantity of LTP-MnBi magnetic material, it will directly affect its magnetic properties.

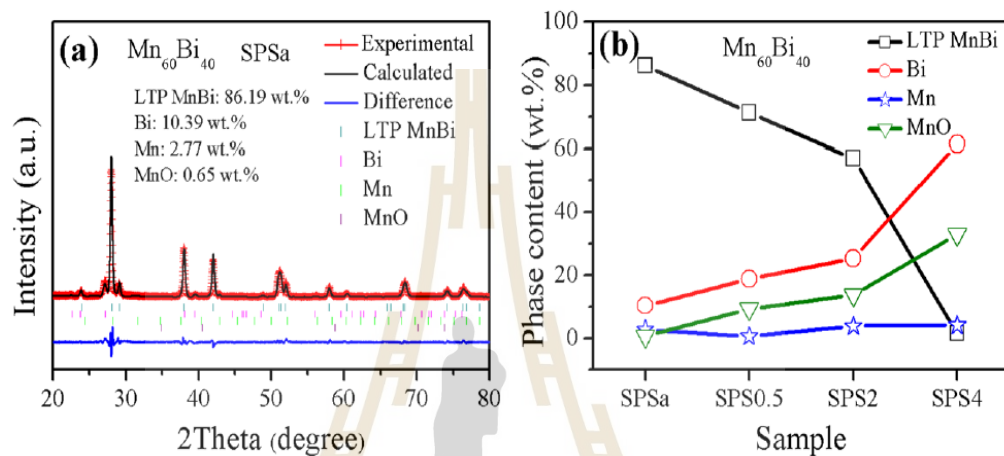


**Figure 2.31** (a) XRD analysis of  $Mn_{60}Bi_{40}$  material (b) The phase ratio under different preparation conditions. (Cao et al., 2018)

Figure 2.32(a) and (b) are the M-H curves and magnetic properties of MnBi magnetic materials measured at room temperature, respectively. It can be seen that the SPSa magnetic material has a magnetic saturation value ( $M_s$ ) of 69.5 emu/g. under a magnetic field strength of 8.5 T. Moreover, it was found that in this study, the MnBi magnetic material was prepared using the SPS technique. The LTP-MnBi content was as high as 86.19% wt. Considering the magnetic properties of the SPS0.5 sample, the residual magnetic saturation ( $M_r$ ) was 26.0 emu/g, the demagnetization value ( $H_c$ ) was 7.11 kOe, and the maximum energy yield  $(BH)_{max}$  was 1.53 MGOe, while the SPS2 sample had a residual magnetic saturation ( $M_r$ ) of 22.7 emu/g, the demagnetization value ( $H_c$ ) is 9.52 kOe, and the maximum energy yield  $(BH)_{max}$  is 0.90 MGOe. It is known that reducing the MnBi magnetic particle size will provide a higher magnetic efficiency. maximum but on the other hand, grinding too long may deteriorate the magnetic properties. It can be seen from figure 2.33(a) that the M-H curves of the second quadrant SPS2 magnetic material are distorted from the loop curve. indicated that the

volume-MnBi The  $(BH)_{\max}$  and  $H_c$  values tended to decrease after more than 0.5 h of grinding, possibly due to phase decay. LTP-MnBi to Bi and Mn phases during the MnBi particle size reduction process by the ball milling method. (Cao et al., 2018).

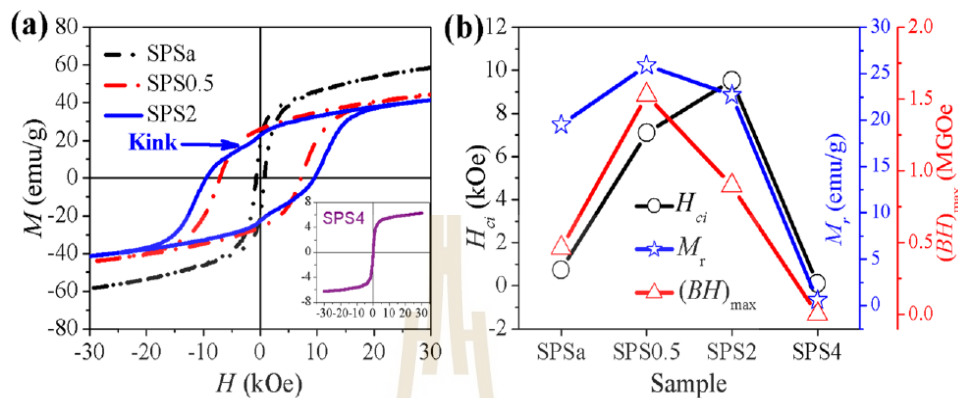


**Figure 2.32** M-H curves (a) Magnetic properties (b) MnBi magnetic material  $(BH)_{\max}$  at 300 K. (Cao et al., 2018).

From the literature review in this section, it was found that the MnBi material synthesis process, particle size, and oxide content have been studied by many research groups, and that these factors greatly affect the properties of MnBi materials. Most of the finished MnBi materials are taken from conventional processes such as arc melting or melt-spinning. From the report, it can be understood that increasing the process, especially the grinding, which induces heat into the system, causes the MnBi material to undergo peritectic transformation. Or oxide formation. What is interesting is that a review of past research revealed that no studies have been conducted to study the relationship between the initial Mn particle size and the MnBi properties synthesized by the sintering method.

### 2.5.5 MnBi based hard/soft composited magnet

Previous studies have demonstrated that the development high magnetic performance of MnBi magnetic materials. In order to obtain MnBi intermetallic compound with high coercivity, high magnetization and large energy density, a lot effort has been spent to develop processes to prepare MnBi (Ma et al., 2014) The theoretical energy product  $(BH)_{\max}$  of about 17.6 MGOe is still lower than current neodymium magnet. This is due to the low saturated magnetization of the MnBi.

To produce high energy product magnet, MnBi shall be used as a hard phase material to composite with soft phase magnetic materials such Fe, Co, Sm and Ni.

In 2014, Ma et al. reported the study of the composite between MnBi and Co Nanowires or Fe nanoflakes. The MnBi powder was prepared by arc-melting, low energy and then ball mill. Co Nanowires and Fe nanoflakes were prepared by melt spinning. The obtained MnBi powder particle size was about 0.5-5  $\mu\text{m}$ . MnBi was mixed with Co Nanowires 0, 5, 10, 15, and 20 wt% and then aligned in a magnetic field of 1.8 T and pressed under pressure of 200 MPa. After that, the sample was sintered in an argon atmosphere at 220-300  $^{\circ}\text{C}$  for 30 min. The demagnetization curves at room temperature of the MnBi composite with Co Nanowires with difference contents are shown in figure 2.33. The coercivity almost unchanged but the saturated magnetization slightly increases with the content of Co Nanowires. However, the energy product was found to decrease with increasing Co Nanowires content.

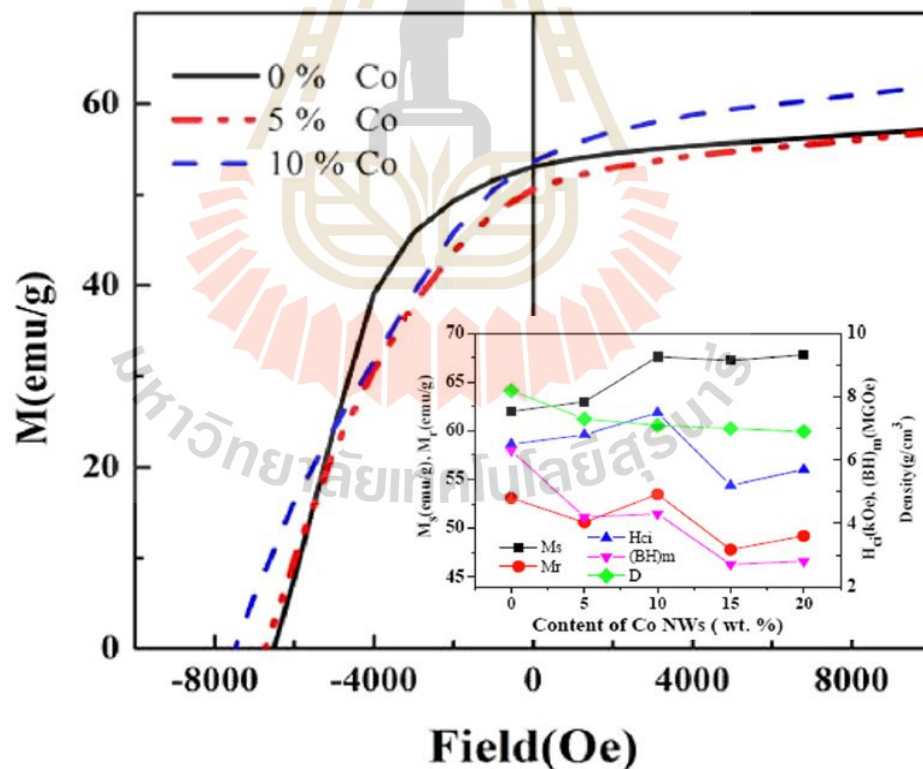


**Figure 2.33** Demagnetization curves at RT for MnBi/Co NWs magnet with difference Co NWs contents. (Ma et al., 2014).

In 2015, Xia Xu et al. reported the magnetic exchange coupled between arc-melt MnBi with Fe and Co composite. Fe and Co nanoparticles were prepared by chemical method. The hysteresis loop, XRD pattern and TEM of FE-Co nanoparticle are shown in figure 2.34. The coercivity value  $\sim 41$ Oe and the magnetization value  $\sim 151$  emu/g by particle size between 5-10 nm.

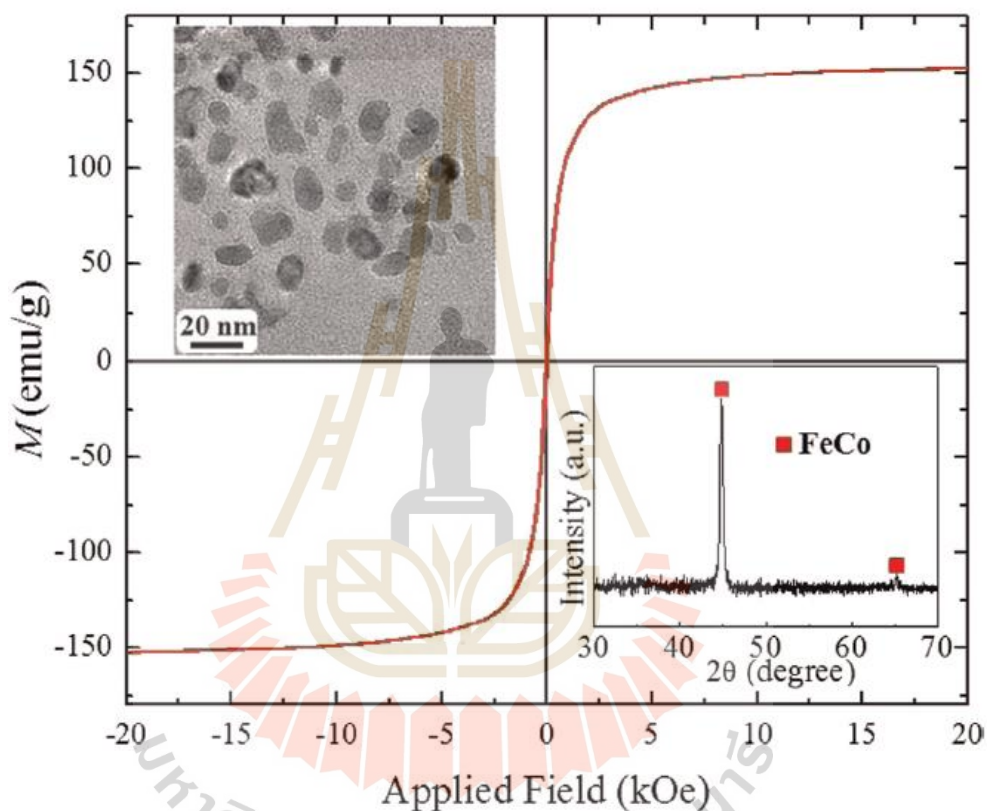
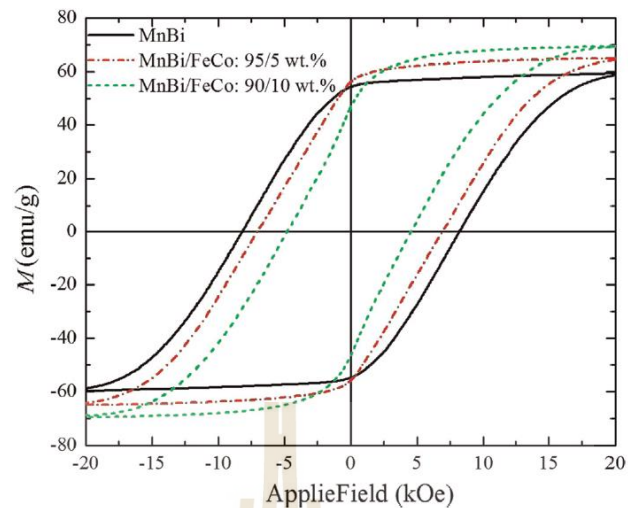


Figure 2.34 Demagnetization curves MnBi/Co NWs magnet. (Xia et al., 2015).

MnBi powder was mixed with the Fe-Co nanoparticles with two weight ratios (MnBi/Fe-Co: 95/5 and MnBi/Fe-Co: 90/10 respectively.) composite was ground for 5 min with hexane 20 mL in the glove box. Figure 2.35 shows hysteresis loops of MnBi, MnBi/Fe-Co (95/5 wt.%) and MnBi/Fe-Co (90/10 wt.%) composite. The saturation magnetization was found to increase, while the the coercivity was found to decrease, with the Fe-Co content.



**Figure 2.35** The hysteresis loop of MnBi, MnBi/Fe-Co (95/5 wt.%) and MnBi/Fe-Co (90/10 wt.%). (Xia et al., 2015).

In 2016, Y.L. Ma et al. studied the MnBi/NdFeB magnetic composite. MnBi alloy prepared by arc-melting in argon atmosphere. The ingot MnBi was then annealed at 563 K for 20 h, and then crushed to powder. MnBi powder particle size was about 0.5 – 5  $\mu\text{m}$ . MnBi was mixed with NdFeB (0, 20, 30, 50, 70, and 100 wt. %) and then aligned in a magnetic field of 1.8 T under pressure of 200 MPa. After that, the samples were sintered in argon atmosphere at 573 K for 30 min. The coercivity and remanence of the composite samples increase gradually with increase NdFeB content, as shown in figure 2.36.

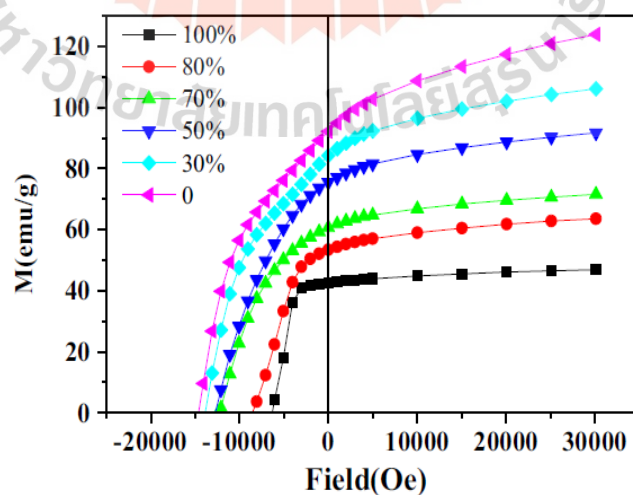


**Figure 2.36** Demagnetization curves MnBi/NdFeB magnet with MnBi content at RT. (Ma et al., 2016).

In 2017, TRUONG XUAN NGUYEN et al. reported the study of MnBi/Co nanocomposite. Co NWs was synthesized by solvothermal method for at different temperature for 60 min. The FESEM images of the prepared Co NWs are shown in figure 2.37.

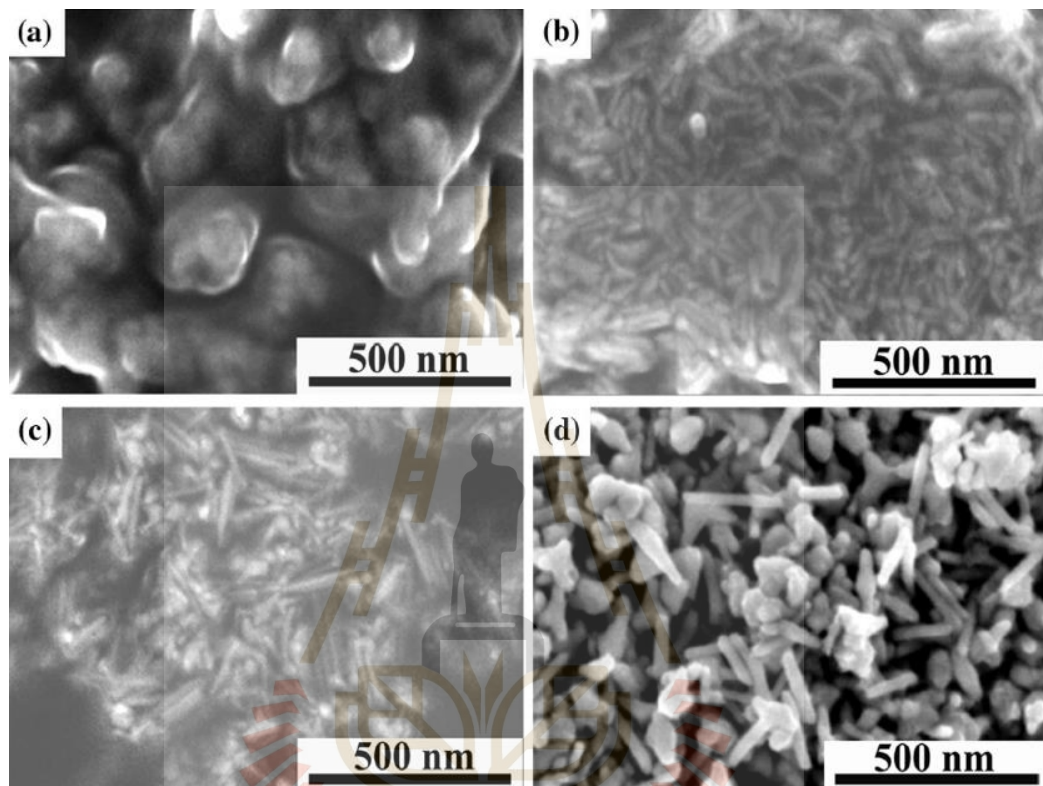


**Figure 2.37** The morphology of Co NWs by solvothermal method for 60 min (a) 200°C, (b) 225°C, (c) 250°C, (d) 260°C. (Truong et al., 2017).

The magnetic properties of Co NWs with difference temperature at 60 min observing by Hysteresis loop, Which, the synthesis Co NWs by solvothermal method at low temperature less than  $\sim 230$  °C is low magnetization ( $< 80$  emu/g), low coercivity ( $< 1$  kOe) and the high temperature more than is high magnetization ( $\sim 110$  emu/g), coercivity value  $\sim 2.6$  kOe. demonstrate the good reaction of Co NWs at higher temperature. show in figure 2.38.

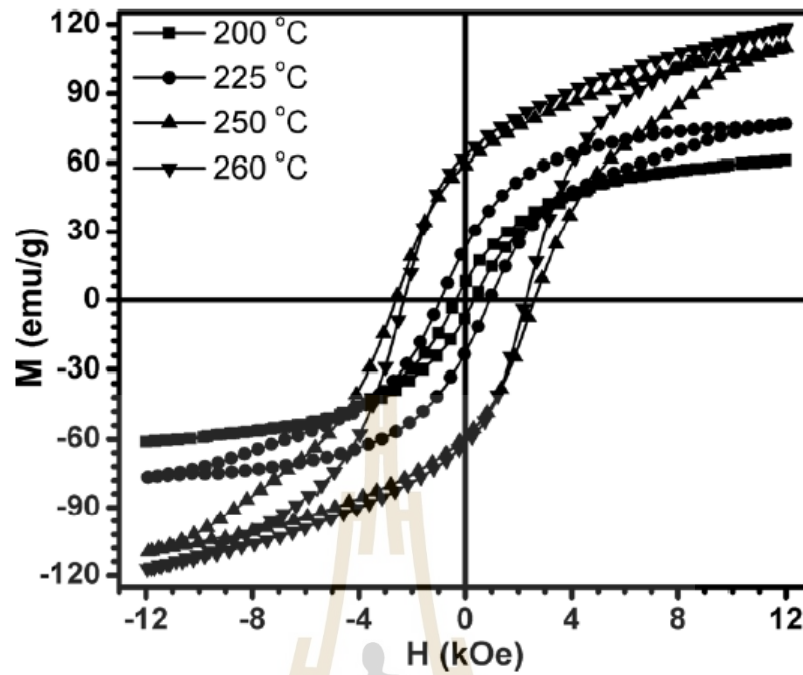


Figure 2.38 The Hysteresis loop of Co NWs for 60 min at difference temperature. (Truong et al., 2017)

## CHAPTER III

### RESEARCH METHODOLOGY

This chapter provides detailed information of vacuum sintering system developed in this work, the experimental procedures to synthesize and characterize MnBi magnetic materials; and MnBi/Co composites.

#### **3.1 Instrument development for vacuum sintering system**

The development of LTP-MnBi magnetic materials synthesis has several techniques. It is very difficult to synthesize LTP-MnBi particles to obtain high purity and single phase. One of the challenges in synthesis is that Mn reacts with oxygen rapidly, which leads to the MnO form as a result of magnetic properties decreasing. Therefore, this research has designed and built a vacuum sintering system for the avoidance of oxides that may be formed during the synthesis process. The vacuum sintering system built into this research was necessary to avoid the existence of oxygen in the system. It's using equipment and components that are available in the laboratory of the synchrotron light research institute. The vacuum sintering system consists of two main components: the vacuum system and the low temperature effusion cell system, as shown in figure 3.1. A small cylindrical vacuum chamber, with a diameter of 8 inches and a length of 16 inches, is connected with a turbomolecular pump (TV 551 NAVIGATOR) with a pumping speed of 500 l/s backed by a scroll pump (ISP-250C model) with a pumping speed of 3.61 l/s. The vacuum pressure is monitored by a pressure gauge with a cold cathode gauge (Pfeiffer PKR251 Compact FullRange™). The vacuum pressure of  $2 \times 10^{-8}$  mbar could be achieved after 24 hours of pumping without baking. The low-temperature effusion cell used in this work is a low-temperature effusion cell (model: NTEZ40-10-22-KS-HL-2118521, by Dr. Eberl MBE-Komponenten GmbH) effusion cell. A commercial low-temperature effusion cell is installed on the CF114 3-way cross fitting. This connection is to prevent accidents that may be dropped

and damage to the turbomolecular pump. The low-temperature effusion cell can be adjusted to control a range of 80 to 800 °C. The temperature of the cell is controlled by a EURO THERM 2408 temperature controller. Finally, the crucible used in this work is a quartz tube with a capacity of 10 cc.

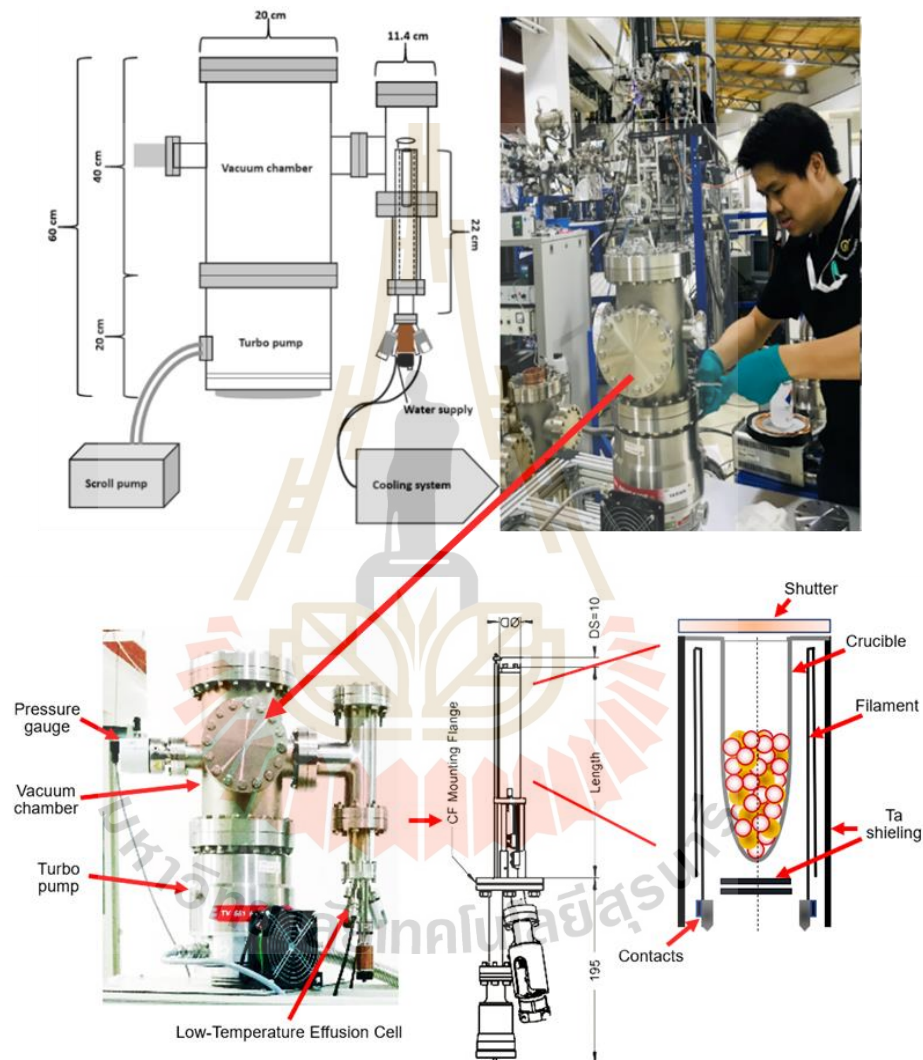


**Figure 3.1** Photo of the vacuum sintering system with draw of the effusion cell. (Ngamsomrit et al., 2020)

### 3.2 Preparation of LTP-MnBi magnetic materials

The preparation of LTP-MnBi particles in this work has been divided into two parts. The first part, high-purity Mn (99+%, powder -40 mesh (size < 420 microns)) and Bi

(99.5%, powder -100 mesh (size<149microns)) powders supplied by ACROS ORGANICS were used as the raw materials in this work, shown in figure 3.2. Mn was ball milled using a planetary micro mill for 3 hours and then sieved through a screen to select Mn powder with a particle size of less than 20 microns. These sieved Mn powders were mixed with Bi powders in an atomic ratio of 1:1, followed by ball milling via mini mill for 40 Hertz for 20 minutes to homogenize, and then sintered in a quartz tube of the effusion cell. The base pressure of this system was about  $2 \times 10^{-8}$  mbar. The temperature of the effusion cell was gradually increased at a  $5 \text{ }^\circ\text{C}/\text{min}$  rate and kept constant from time to time to maintain the vacuum pressure below  $5 \times 10^{-7}$  mbar. It took about 210 min for the effusion cell to reach a temperature of  $275 \text{ }^\circ\text{C}$  from room temperature. After reaching  $275 \text{ }^\circ\text{C}$ , the mixture was sintered for different times (3, 6, 12, 24, and 48 hours). Then, the power to the effusion cell was turned off, letting the cell cool down to room temperature. The sintered samples were crushed and then, grinded to powder.



Figure 3.2 Raw materials of (a) manganese and (b) bismuth.



**Figure 3.3** The procedure for the synthesis of MnBi magnets starts with mixing Mn and Bi powders.

And second part, the research report discovered that smaller MnBi particle sizes on the nanometer scale result in increased magnetism efficiency. As a result, the preparation of the LTP-MnBi magnetic materials in this second section, before the synthesis will be reduce particles size of Mn for the increase the surface area by using a planetary micro mill, the rotational speed was 300 rpm and the ball mill time from 3-15 hours as shown in figure 3.4. Subsequently, the sieve screen of Mn particles with a grid sieve has 3 ranges: less than 20 microns, 20-53 microns, 53-106 microns, and more than 106 microns, as shown in figure 3.5. for selected particle size to be similar and suitable for use in various experimental conditions.



**Figure 3.4** Planetary mill process.



**Figure 3.5** Sieve screen process.

The mixing ratio of Mn and Bi powders used in this second part has an atomic ratio of 1:1, which was calculated from the atomic mass of both elements (Mn: 54.94 g/mol and Bi: 208.98 g/mol). The LTP-MnBi preparation is based on the previous preparation. In this part, the focus was on the synthesis of manganese-bismuth magnetic powder at a low temperature state (LTP-MnBi).

### 3.3 Characterization techniques

In this part, the experiment can be divided into two parts. The first section focused on grinding of Mn powder for different durations and the second section is to examine magnetic properties, chemical composition of MnBi. High purity MnBi powder (99+%, particle size < 420  $\mu\text{m}$ ) and Bi powder (99.5%, particle size < 149  $\mu\text{m}$ ) supplied by Acros Organics were used as the raw materials in this work. Mn particles were obtained using planetary micro mill difference times (3, 7, 11, and 15 hours) and then sieved to obtain Mn powders (< 20 microns). The Mn with different ball mill times and Bi powder were mixed with 1:1 atomic ratio and then sintered in a quartz tube on low temperature effusion cell (Dr. Eberl MBE-Komponenten GmbH, Germany) in ultrahigh vacuum. The base pressure of the system is about  $10^{-8}$  mbar. The temperature of the

effusion cell was gradually increased with 5 °C/min rate and kept constant from time to time to maintain the vacuum pressure to be below  $5 \times 10^{-7}$  mbar. The specimens were sintered at 275 °C and hold for 12 hours. These specimens were labelled as MnBi-M3, MnBi-M7, MnBi-M11 and MnBi-M15 according to the Mn grinding time. After that, sintered samples were grinded using mini ball milling (Mini mill, FRITSCH, PULVERISETTE23) at 40 Hz for 20 min and then sieved with Test Sieve, Retsch, ASTM E11 20  $\mu\text{m}$  to obtain the MnBi particles with the size of less than 20  $\mu\text{m}$ . XRD (Bruker D2 PHASER, Cu  $K_{\alpha}$  radiation, ( $\lambda=1.5406 \text{ \AA}$ )) was used for phase identification. Powder morphology and elemental compositions were characterized using SEM/EDS (QUANTA 450). The magnetic properties were investigated by using VSM (Quantum Design, VersaLab) with applied magnetic field of  $\pm 3\text{T}$ . The elemental composition was investigated by XPS at Beamline 3.2 of the Synchrotron Light Research Institute, Thailand.

#### 3.4 Preparation of MnBi by glycine addition conditions

In this section, the experiment was divided into two parts. The first part focused on the grinding of Mn powder for 3 hours using a planetary mill. The second part focused on the effect of Mn particle size reduction by adding glycine about 0.5 g to prevent particle agglomeration Mn particles during the ball milling process for 1 and 3 hours. The high purity Mn powder (99+%, particle size < 420  $\mu\text{m}$ ) and Bi powder (99.5%, particle size < 149  $\mu\text{m}$ ) supplied by Acros Organics were used as the raw materials in this work. The Mn particles obtained for those different methods were mixed with Bi powder at a 1:1 atomic ratio and then sintered in a quartz tube (60mm (OD) x 52mm (ID) x 1.2m, 4mm (T)) on low temperature effusion cell (Dr. Eberl MBE-Komponenten GmbH, Germany) at ultra-high vacuum. The base pressure of the system is about  $10^{-8}$  mbar. The temperature of the effusion cell was gradually increased with 5°C/min rate and kept constant from time to time to maintain the vacuum pressure to be below  $10^{-7}$  mbar. The samples were sintered at 275 °C for 12 hours. After that, it was grinded to powder form using ball milled (Mini mill, FRITSCH, PULVERISETTE23) at 40 Hz for 20

mins. The phase was identified using XRD technique (Bruker D2 PHASER, Cu  $K\alpha$  radiation, ( $\lambda=1.5406 \text{ \AA}$ )). The morphology powder and elemental compositions were characterized using SEM/EDS (QUANTA 450). The magnetic properties were investigated by using VSM (Quantum Design, VersaLab) with applied magnetic field as  $\pm 3T$ . The elemental composition was investigated by XPS at Beamline 3.2, Synchrotron Light Research Institute.

### 3.5 Preparation of LTP-MnBi and Co composite

In the past, I worked with students from the University of Mandalay to conduct research on the composite materials method, which is divided into two parts as follows: (1) The separation of each element of Mn-Bi-Co composite with an atomic ratio of 1:1 and (2) The synthesized MnBi first followed by composite Co with 1:1 at%. Under the second approach, two more parts were separated by sintering and no sintering (Nguyen et al., 2017) found that MnBi composite with Co demonstrates coercivity and saturation magnetization more than Mn-Bi-Co as shown in the figure 3.6.

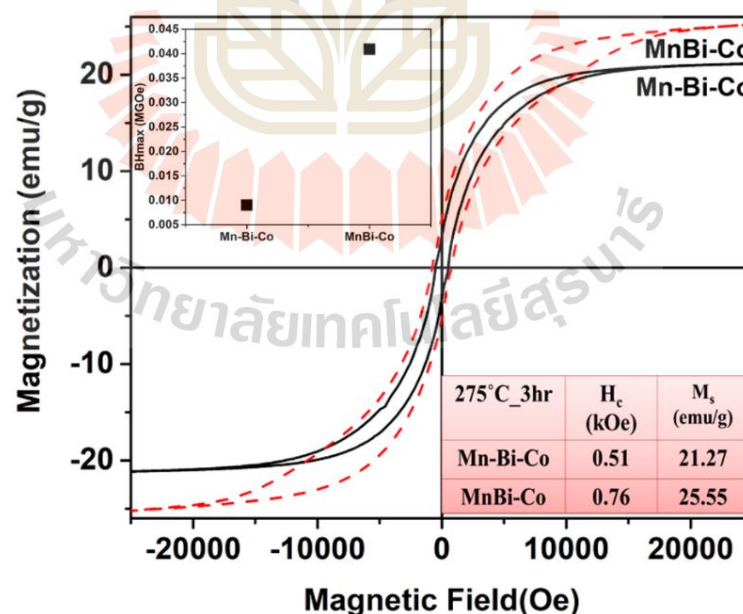


**Figure 3.6** M-H curves of MnBi composite with Co and each element of Mn- Bi-Co composite with an atomic ratio of 1:1 after sintering in a vacuum at 275 °C for 12 hours.

The MnBi/Co sample was then synthesized again and divided into the two other composite tests mentioned above, this demonstrated that the MnBi/Co composite is not sintered and has a higher coercivity and saturation magnetization. The effect of the no sintered composite on the energy product (BH)<sub>max</sub> is 1.139 MGOe, and when the MnBi/Co sintering in vacuum is considered, the effect is 1.139 MGOe, it is obvious that the content of LTP-MnBi is decreasing, and that sintering may also cause oxidation.

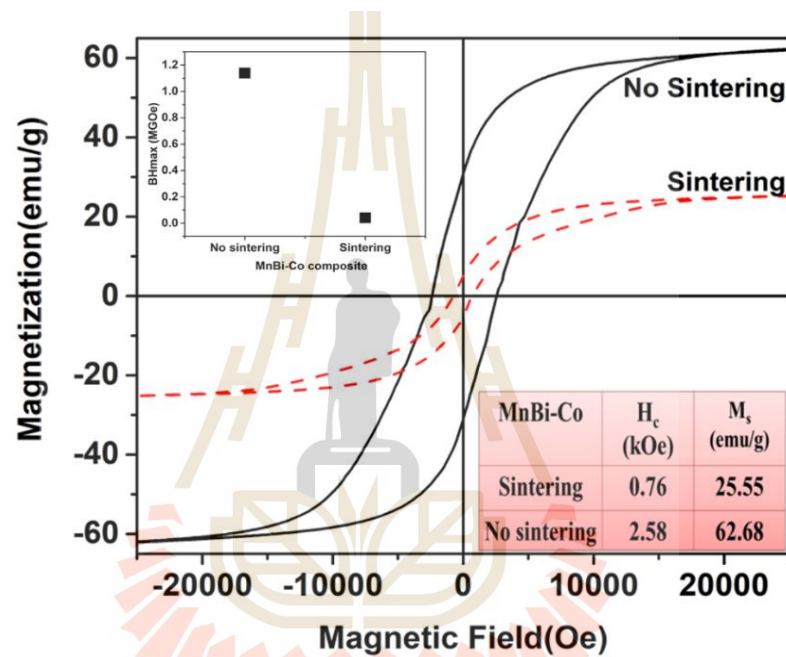


**Figure 3.7** M-H curves of MnBi composite with Co by vacuum sintering at 275 °C for 12 hours and MnBi ball milling at 300 rpm for 30 minutes with Co (no sintering).

According to the results of the tests, the most efficient method was the MnBi/Co sample with no sintering form. hence, in preparation about the composite in this work, we have condition to productions as followed it begins by grinding the Mn element to a smaller grain size for the increase surface to the contact with Bi interaction and become to LTP-MnBi form. The Mn grinding time was 3, 7, 11 and 15 hours, and the Mn particles less than 20  $\mu\text{m}$  were selected using a sieve. Therefrom, it was mixed with Bi element in atomic ratio of 1:1 and sintered for 12 hours as performed in section 3.2, finally, the carry out to the composite between LTP-MnBi

particles and Cobalt powder in atomic ratio of 1:1 (the atomic mass of Co is 58.93 g/mol) followed by ball milling to achieve as much homogenous as possible using planetary micro mill of SLRI with under speed of 300 rpm for 30 minute. Afterwards, sieve screen of LTP-MnBi/Co composite with selected particles less below 20  $\mu\text{m}$ , in order to contribute to inspect the properties and adjust the magnetic direction of LTP-MnBi/Co particles in under a magnetic field of 0.5 T next.

### 3.6 Preparation of MnBi magnetic materials alignment

The composite was formed according to various conditions of LTP-MnBi-Co and the selected particles were sieved to a particle size of less than 20  $\mu\text{m}$  and then mixed with epoxy resin in a ratio of 1:0.05 g. Next, the LTP-MnBi-Co specimen is placed on top of the magnetic rods as shown in figure 3.8 to arrange the magnet under the magnetic field of 0.5 T for 24 hours. The goal of this section of the experiment was to investigate the magnetic domain arrangement of LTP-MnBi and LTP-MnBi/Co magnetic materials.

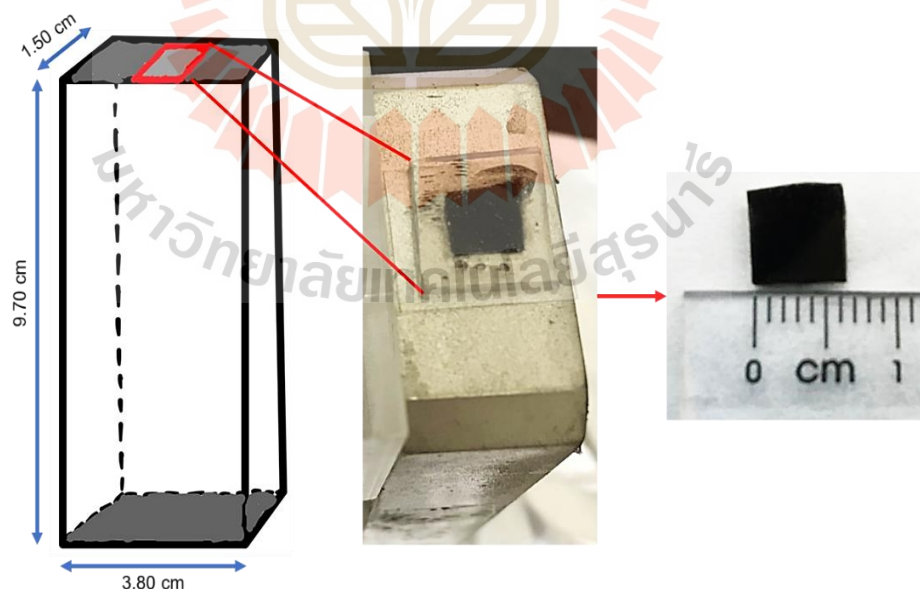


Figure 3.8 MnBi powder placement on bar magnets with a magnetic field of 0.5 T.

**Table 3.1** List of the values of the parameter's studies in this work.

Parameter of the study	Conditions
Temperature	275 °C
Particle size (before sintering)	Avg. 1-5, 5-10 and 10-20 $\mu\text{m}$
Particle size (after sintered)	<20 $\mu\text{m}$ and 20-53 $\mu\text{m}$
Pressure	$10^{-8}$ , $10^{-2}$ mbar and ambient
Ratio of raw materials (Mn and Bi)	1:1, 1.5:1, 2:1, 4:1
Grade materials	Laboratory

### 3.7 Characterization of MnBi magnetic materials

#### 3.7.1 X-ray diffractometry (XRD)

X-ray Diffraction (XRD) is a fundamental technique that can be used for phase identification of crystalline materials and can provide information on the dimensions of the unit cell. The X-rays are produced using the cathode ray tube and are based on the diffraction of X-ray radiation. These X-ray beams will be filtered to provide a monochromatic radiation form and directed toward the object. When the electron beam incident on an object, the reflected beam is refracted at an angle equal to the incident angle. In other words, the interaction between the incident beam and the object generated the constructive interference and the diffracted radiation as shown in figure 3.9. From the XRD measurement results, it is possible to analyze and identify each element type, as each element has its own unique crystal structure pattern, and the distance between the planes of the atoms arranged is also different. This is the same as the fingerprint of different elements. As shown in figure 3.9.

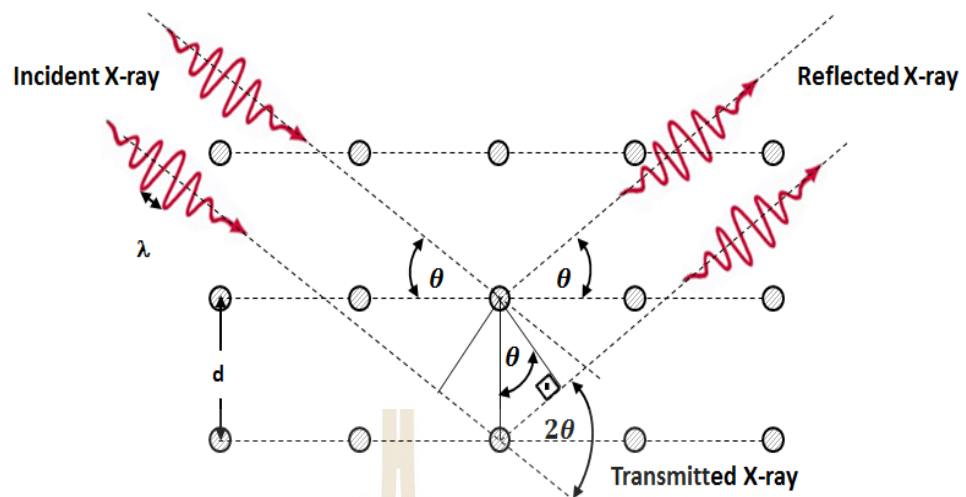


**Figure 3.9** Bragg's law of diffraction condition depicted as lattice planes. (Kot et al., 2014).

The XRD patterns were analyzed based on the Bragg's law, given as the following

$$n\lambda = 2d\sin \theta$$

where:  $n$  is the order diffraction,  $\lambda$  is wavelength of X-ray source,  $d$  is lattice spacing between crystal planes and  $\theta$  is the diffraction of angle incident and diffraction beam. Scanning the sample through range of  $2\theta$  angles to diffraction directions of the lattice.

In this study, the structure of MnBi particles and the MnBi/Co composite were investigated by X-ray diffractometer (Bruker D2 PHASER) using X-ray source with Cu  $K\alpha$  radiation ( $\lambda = 0.15406$  nm). This condition is the step size of 0.02 degree and step times of 0.4 were used to report the XRD patterns in the  $2\theta$  of 20°- 60°. The crystalline material has been identified using XRD patterns with the database examined by the Joint Committee for Powder Diffraction Standards (JCPDS) organization.

The phase identification was investigated by using the XRD technique (Cu  $K\alpha$  radiation ( $\lambda = 1.54056$  Å), Bruker D2 PHASER) at The Center for Scientific and Technological Equipment, Suranaree University of Technology, as seen in figure 3.10. The XRD-D2 used angle incident 2-theta scans range between 20-60 degrees for LTP-

MnBi powder and LTP-MnBi/Co composite powder with a step size of 0.02 degrees, a step time of 0.5 and x-ray diffraction pattern results. The peak intensity standard from JCPDS files.

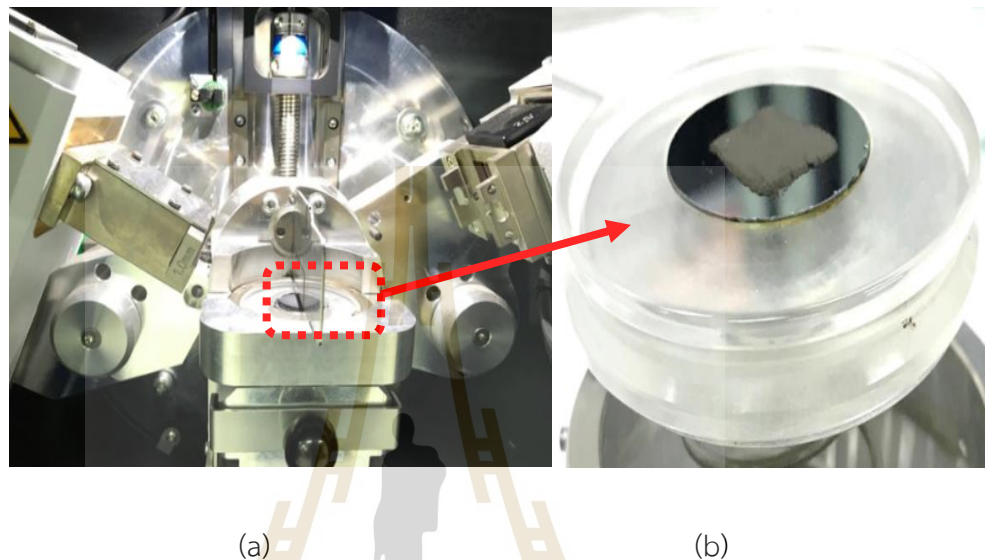


**Figure 3.10** (a) Sample placement for XRD measurements and (b) sample holder.

### 3.7.2. Scanning electron microscope and energy dispersive Spectroscopic (SEM&EDS)

Scanning electron microscopy (SEM) is an advanced technique for characterization, the morphology, and analysis of materials. This technique makes use of electron beams to focus on the specimen and can generate high-resolution images of objects. The electron beam is produced from the electron gun due to thermionic emission under vacuum and the motion of the anode towards the magnetic lens in the vertical direction. The magnet lens has controlled the size to reduce the increased intensity of the electron beam. The electron beam travels downward through the objective lens, which is responsible for adjusting the electron beam to have a focal point on the surface of the object with support by the scanning coil as shown in figure 3.11.(Kannan et al. 2017)

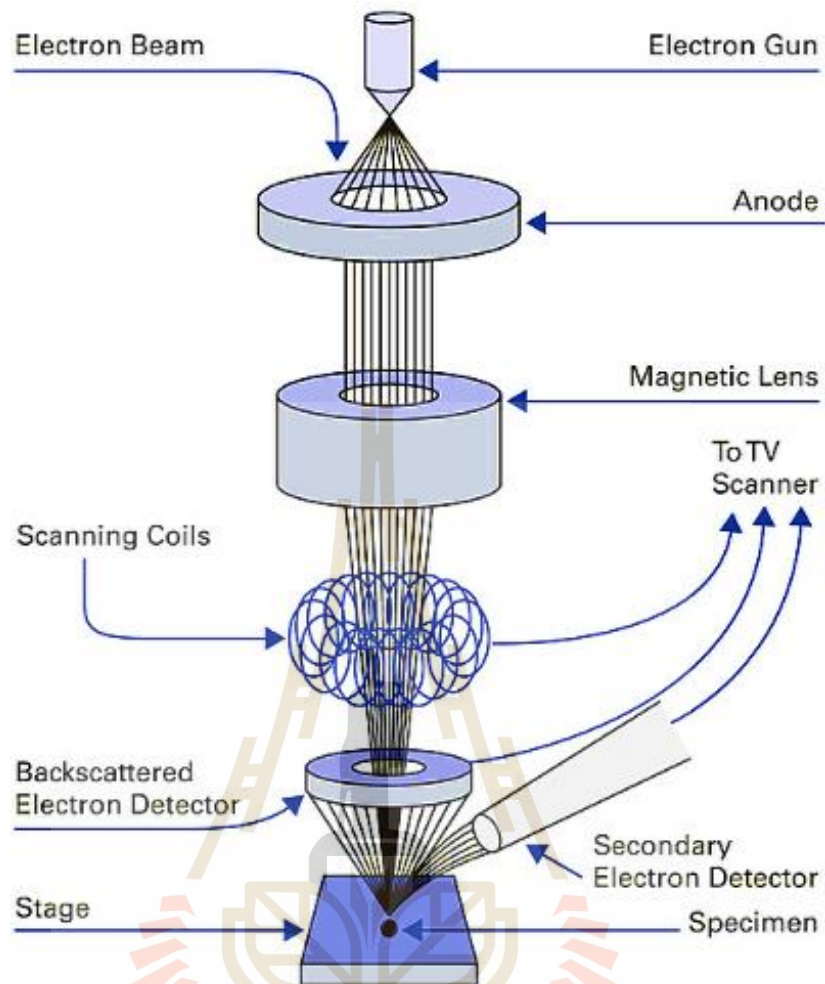


**Figure 3.11** The fundamental diagram of a scanning electron microscope (SEM). (<https://www.pi-usa.us/>)

When the incident electron beam interacts with the specimen, it will emit multiple signals because of the electric charge it interacts with the arriving electrons. The secondary electron image (sei) is a low energy electron that occurred on the surface about 10 nm below the surface and provides surface characterization. The outcome of the secondary electron is producing the backscattered electron, which electrons have some energy loss to the atom in the specimen and the scattering back out. The scattered electron has a higher energy than the secondary electron and happens on the surface deeper than 10 nm. The X-ray radiation excites the electromagnetic waves produced by the electron at different levels, causing the atom to maintain equilibrium with the electron orbital energy level higher than would be

replaced. Excess energy is released in the form of electromagnetic waves (Auger electron). These electromagnetic waves have a specific wavelength of each element and can be the analyzed element. (Kalsoom et al., 2018)

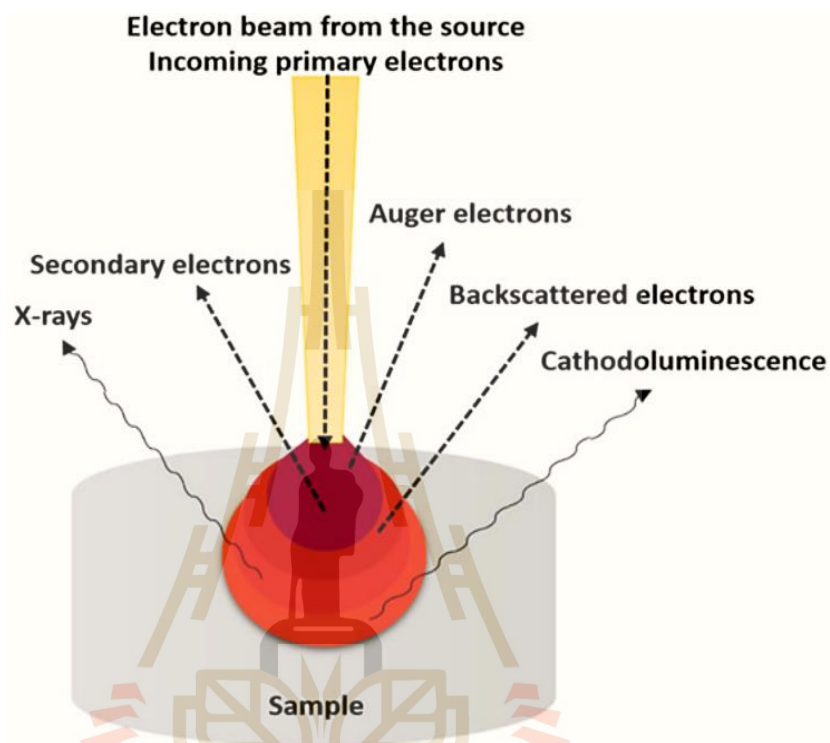


**Figure 3.12** The interaction area of the electron beam and the signal emitted from the specimen. (Akhtar et al., 2018).

The morphology and chemical composition of LTP-MnBi and LTP-MnBi/Co particles were observed by SEM/EDS (FEI, QUANTA 450) at the Synchrotron Light Research Institute as shown in figure 3.13. From these measurements, the image of the particles can be obtained by the interactions between manganese, bismuth, and cobalt after sintered. Energy dispersive spectroscopy uses X-ray beam stimulation of the atom to generate the emission. The energy is a special characteristic of each element.

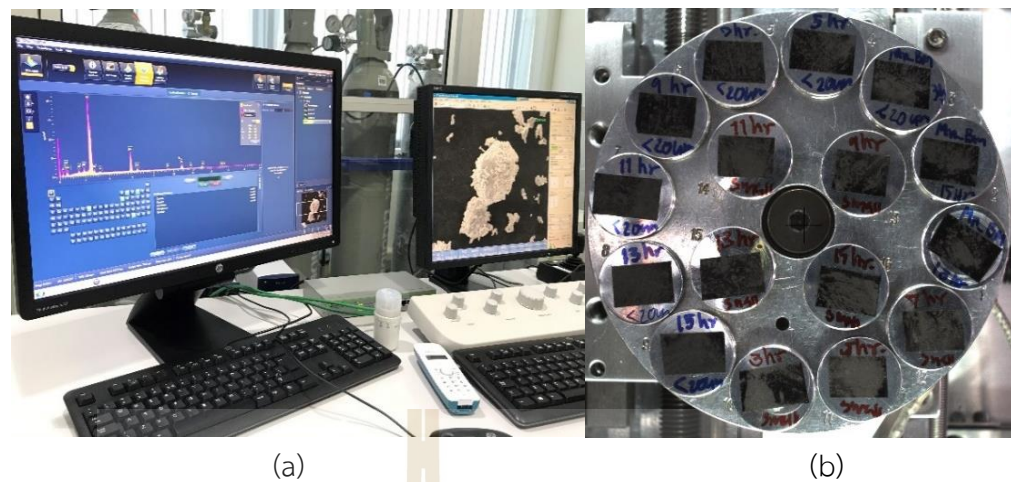


**Figure 3.13** (a) Display during measurement of physical characteristics and chemical composition at various locations and (b) Sample positioning within the SEM machine.

### 3.7.3 Vibrating sample magnetometer (VSM)

The VSM is a measurement instrument that uses the vibrating principle of samples to study the properties of magnetic materials. Simon Foner invented it at the MIT Lincoln Laboratory in 1955, and it was officially published in 1956 with an adaptation of the concept from D.O. Smith's vibrating-coil technique. The principle of the VSM technique is to measure the magnetic moment of a substance. Samples that vibrate perpendicular to a uniform magnetic field by VSM are classified as inductive magnetic measurement techniques. Based on Faraday's Law of induction, the VSM operates by placing the sample in a uniform magnetic field generated by an electromagnet. An electromagnet is connected to the power supply. A magnetic sample is magnetized by an applied magnetic field. Arrange the magnetic domains in the substance. This means that the magnetic polarity of a substance creates its own magnetic field. Subsequently, vibrating the sample in an up down or perpendicular direction to the applied magnetic field induces and generates an electromotive force. electromotive force (emf) in the detection coils according to Faraday's law of inductance. Then this electromotive force will be measured. Noise is detected and eliminated using a lock-in amplifier, where the emf is directly proportional to the magnetite value. Magnetization of the sample It will show results in the form of loop hysteresis.

The magnetization value and the external magnetic field. (M-H hysteresis loop). The vibrating sample magnetometer depends on the sensing of the electromagnetic force induced in the coil of wire as the following equation.

$$\epsilon = -N \frac{d}{dt} (BA \cos \theta)$$

Where

N	is the number of rounds wire in the coil
A	is the coil turn area
B	is the magnetic induction
$\theta$	is the angle between the magnetic induction (B) and the normal direction to the surface of coil

In actual, we are knowledge about the coil parameter as N and A is inessential if the system can be calibrating with well-known specimen.

The vibrating component alters magnetic flux, which creates an electric field within a coil. This electric field can be measured and can provide insight into the changing of the magnetic field. When a sample is placed in a uniform magnetic field, magnetization is induced in the sample, causing it to vibrate sinusoidally. The magnet is enabled first, then the assay is initiated. Hence, if the sample is magnetic material, it will change into higher than the magnetic field is produced. The magnetic field has occurred around the specimen and when the vibration is initiated, the material magnetization can be examined and analyzed as a change takes place in correlation to the time of motion.

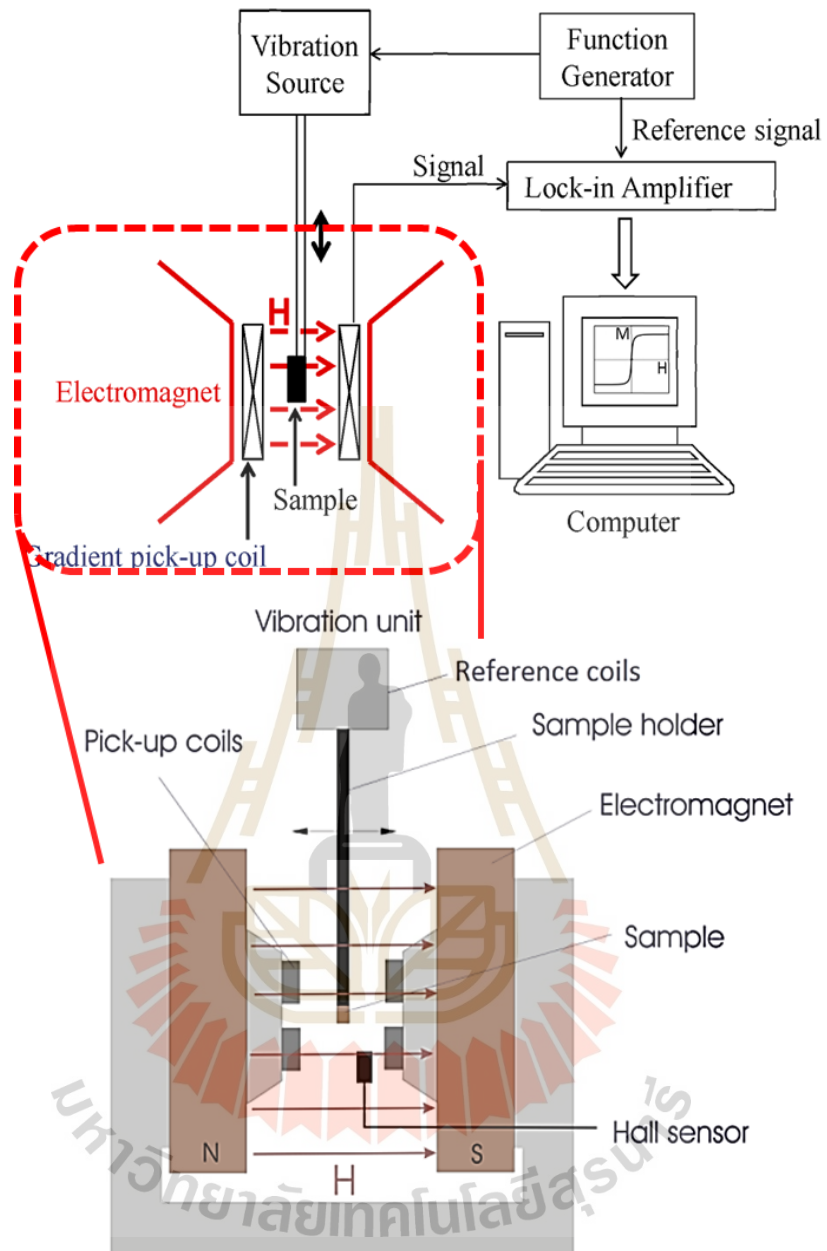


**Figure 3.14** A simplified diagram showing the components of the VSM and an inductive probe region diagram consisting of a sensing coil, sampling and sampling bars under an external magnetic field. (Huang et al., 2015; Rafique et al., 2015).

In this research, the study of the magnetic properties of MnBi, MnBi/Co, and Co particles at room temperature. The prepared sample with an average weight of about 0.0700-0.0800 g was put into the sample holder, The configuration of VSM measurement of the set magnetic field at 200 Oe/sec and up to  $\pm 3$  T.

The magnetic performances of the powder were measured using a vibrating sample magnetometer (Quantum Design, VersaLab) at the Institute of Nanomaterials Research and Innovation for Energy (IN-RIE), Faculty of Science, Khon Kaen University.

The magnetic properties of the powder were measured using a vibrating sample magnetometer (Quantum Design, VersaLab) at the Institute of Nanomaterials Research and Innovation for Energy (IN-RIE), Faculty of Science, Khon Kaen University, as shown in figure 3.15. The vibrating sample magnetometer (VSM) instrument is a fast and sensitive DC magnetometer by oscillating the sample near a detection coil and synchronously detecting the voltage induced by the compact gradiometer pickup coil configuration. With a temperature range of 50-400 K, the oscillation amplitude is large (1-3 mm), and the frequency is 40 Hz.

In this work, the study of the magnetic properties of MnBi, MnBi/Co, and Co particles at room temperature is presented. The configuration of VSM measurement of the set magnetic field at 200 Oe/sec and up to  $\pm 3$  T. The prepared sample with an average weight of about 0.0700-0.0800 g was put into the sample holder.

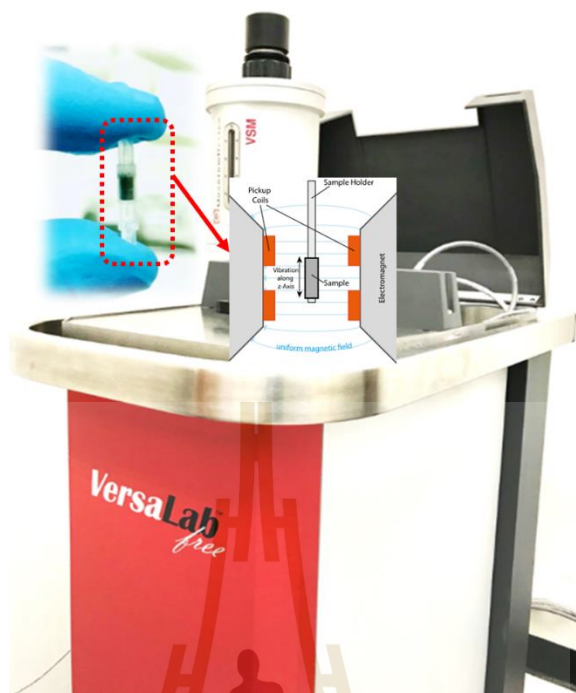


**Figure 3.15** Indicates the position of the sample measurement within the VSM.

### 3.7.4 BL3.2Ua: Photoemission Spectroscopy (PES)

Figure 16 depicts the beamline 3 (BL3), which consists of two branch lines for the PEEM (Photoelectron Emission Spectroscopy) and PES (Photoemission Spectroscopy) experimental stations at the Synchrotron Light Research Institute, Thailand. Electrons are generated by a thermionic electron gun and then accelerated in the linear accelerator by a 2,856 MHz high power microwave (LINAC). The LINAC is used to create a 40 MeV electron accelerator and transport it to the booster synchrotron, where it is accelerated to 1.2 GeV. (Pairsuwan et al., 2007; Songsiriritthigul et al., 2010). This thesis was measured at the BL3.2Ua beamline. The BL3.2Ua employs a plane gratin monochromator with variable line spacing and was designed to detect photon energies ranging from 40-160 to 220-1040 eV, as well as synchrotron light from an undulator. (Nakajima et al., 2013; Songsiriritthigul et al., 2001).

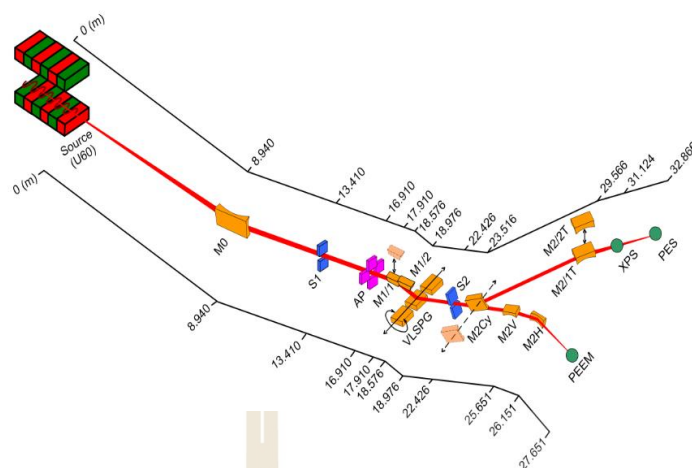


**Figure 3.16** The optical layout of the BL3 beamline. (Songsiririttigul et al., 2007).

### 3.7.4.1 X-ray Photoemission Spectroscopy (XPS)

X-ray Photoemission Spectroscopy (XPS) is a technique that can be analyzed both quantitatively and qualitatively and can provide information about the chemical properties on the surface of materials such as chemical structure, chemical bonding, atomic oxidation state, and number of the element etc. The XPS technique is known as Electron Spectroscopy for Chemical Analysis (ESCA), which uses light energy in the soft X-ray to stimulate photo electrons as shown in figure 3.17. Photoelectron angles, electron spin characteristics, and energy are all obtained from XPS measurements. The focus is on the analysis of the core electron bonding energy because the atomic binding energy is a specific energy. It can identify the type of element and the chemical state of each element that constitutes the surface area. This technique is based on the conservation principle of energy in which the electron is stimulated out of the atom by light energy ( $h\nu$ ) as shown in figure 3.17. These electrons are measured for kinetic energy ( $E_k$ ) via the electron energy analyzer. The kinetic energy values are related to the binding energy;  $E_b$ ) and the value of the work function ( $\phi$ ) as in the following equation.

$$E_k = h\nu - E_b - \phi$$

When  $h\nu$  is the photon energy,  $E_k$  is the kinetic energy of the electron,  $E_b$  is the binding energy of the electron and  $\phi$  is the work function

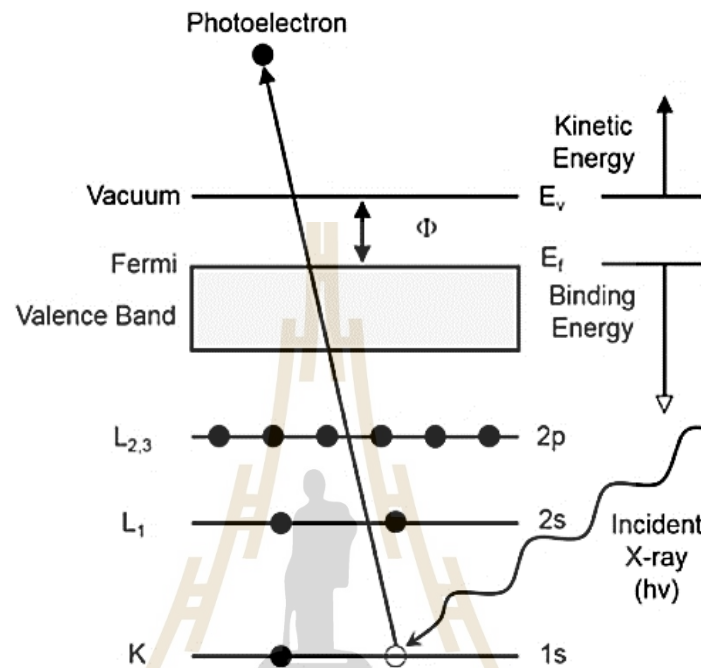
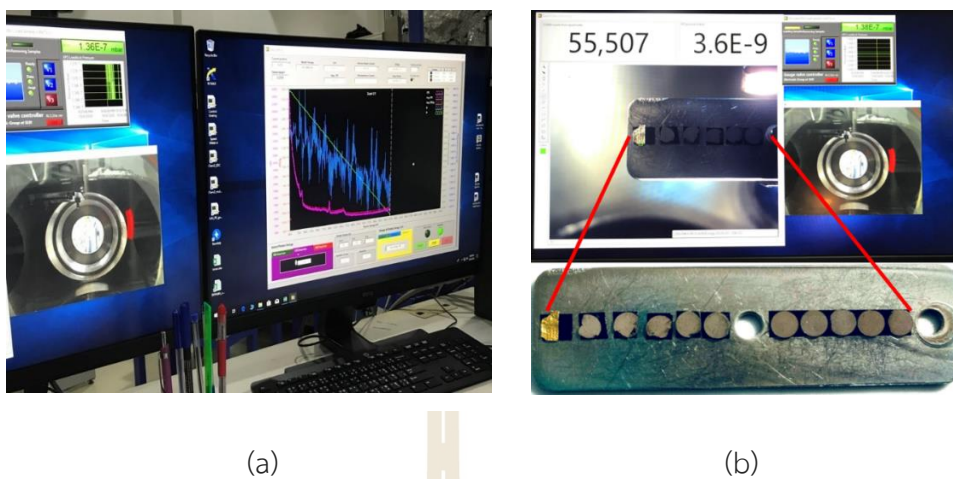


Figure 3.17 XPS principle. (Qiu et al., 2019).

XPS spectra were used to identify the chemical bonding states of MnBi magnetic materials. The XPS measurements were carried out at the Synchrotron Light Research Institute of Thailand's BL3.2Ua: PES (Photoelectron Emission Spectroscopy) beamline, The MnBi powder was prepared on the substrate holder, and the sample scale area must be greater than  $5 \times 5 \text{ mm}^2$  when compared to the beam size as shown in figure 3.18(b). The XPS technique is sensitive on the surface of materials, but it requires an ultra-high vacuum to avoid collisions with air molecules.



**Figure 3.18** (a) Display during measurement of the chemical composition at the surface of the sample and (b) Sample positioning within the XPS system.

## CHAPTER IV

### RESULTS AND DISCUSSIONS

This chapter presents the experimental results and discussions obtained during this thesis research. The primary task focuses on the development of a vacuum sintering system, the determination of the optimum condition, the development of an oxide reduction system, and the investigation of exchange coupling of MnBi/Co composites. The effects of Mn particle size, vacuum pressure, and the effect of glycine addition during the Mn ball milling process.

#### 4.1 Commissioning of vacuum sintering system

The primary purpose of this research was to synthesize MnBi magnetic materials and optimize their magnetic properties. However, because the Gibbs free energy of the reaction between Mn and Bi is negative, manganese elements can quickly convert to manganese oxide form when exposed to oxygen. Since the assembled sintering system was used to synthesize MnBi magnetic materials in this study, it was necessary to avoid the presence of oxygen in the system during the reaction. Initially, a vacuum system with a large vacuum chamber mainly 16 inches in diameter by 32 inches long was assembled. The vacuum was created by 3 types of pumps: ion pumps, turbomolecular pumps with a pumping speed of 500 l/s, which when connected in series with the scroll pump has a pumping speed of 3.61 l/s. The vacuum pressure of the system was measured via a cold cathode gauge (Pfeiffer PKR251 Compact FullRangeTM). The vacuum pressure of the first system assembled was approximately  $10^{-7}$  mbar by the pumping up to one week before sintering in vacuum, which is considered to consume more energy and time than necessary. Due to this issue, the idea of improving the vacuum system to a smaller size was created to reduce the power consumption and synthesis time of MnBi magnetic materials. It started with the design of the existing parts at the Synchrotron Light Research Institute, Nakhon Ratcha-

sima province and assembled a vacuum system that is half the size of the first system, the details of which are described in the chapter III topic. The vacuum pressure of this small system is as low as  $10^{-8}$  mbar after 24 hours without baking.

However, the effusion cell needs to operate at a pressure below  $5 \times 10^{-7}$  mbar. The increased temperature should be increased in an appropriate ratio, At the beginning of the temperature increase, the water is excreted on the surface of the material, and as the temperature increases gradually, until the melting point of the substance. The vapor pressure of that substance increases rapidly, causing the atmospheric pressure to rise. Therefore, in this research, the atmospheric pressure is maintained at no more than  $10^{-7}$  mbar. From the graph, Figure 4.1 shows that the relationship between pressure and temperature as a function of the time taken to increase the temperature. After 24 hours of pumping out the air, in the small vacuum chamber there is a vacuum pressure of about  $2 \times 10^{-8}$  mbar without baking at room temperature. The initial increase in the temperature repels moisture to the surface of the materials, causing the atmospheric pressure to increase. Until the temperature up to about 120-125 °C, it is necessary to break the temperature rise in the first cycle because in this research the atmospheric pressure was not exceed  $10^{-7}$  mbar (blue line) by taking a break to allow the vacuum pump to remove excess moisture or air for about 30-45 minutes, the atmospheric pressure gradually dropped to a level of 10-8 mbar. After that, the gradually increase of the temperature according to the specified conditions to approximately 170-175 °C, 215-220 °C, and 240-245 °C, taking breaks for cycles 2, 3, and 4 respectively. When the temperature is equated to the melting point of Bi (271 °C), the vapor pressure of the substance increases rapidly, but, in this work, the temperature was used slightly above the melting point of Bi and the temperature was maintained according to the conditions. The process in this section takes approximately 240 minutes, after the condition has been held to cool down to room temperature (red line). which takes time to heat up, until it clearly indicates that the rate of temperature increase affects the increase in atmospheric pressure.

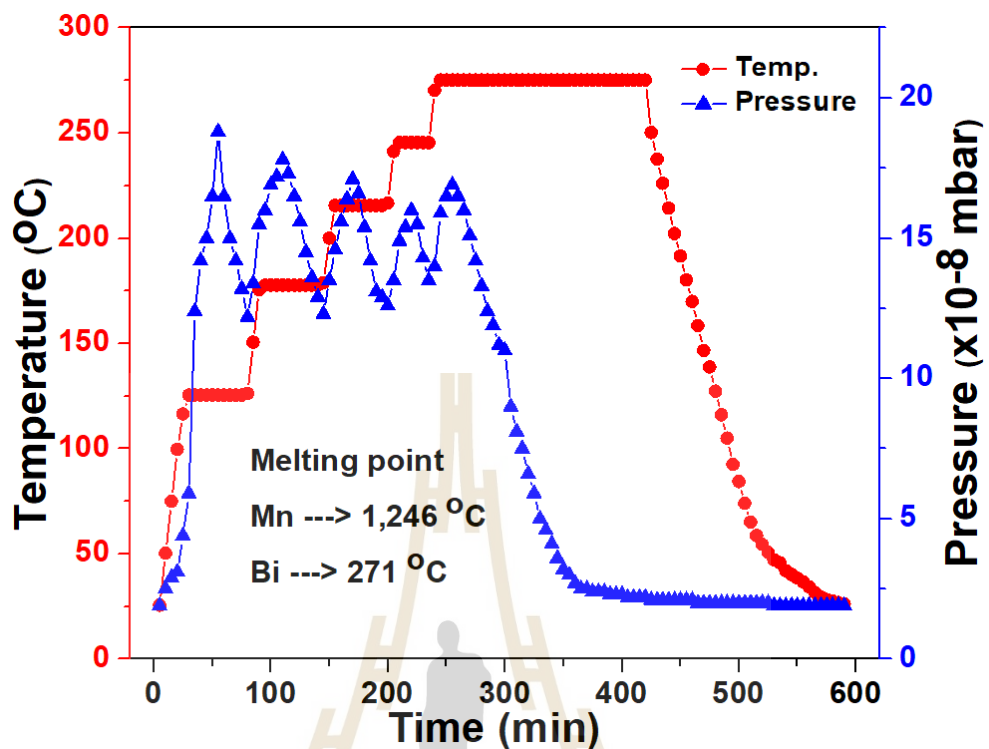


Figure 4.1 Typical graph showing the relationship between vacuum pressure and temperature in the effusion cell during sintering.

#### 4.2 Synthesis of LTP-MnBi

In this work, LTP-MnBi was synthesized by low-temperature liquid-phase sintering in vacuum using the sintering system described above. The LTP-MnBi magnetic materials synthesis is illustrated and explained in detail in chapter III. In this section, the synthetic results shown in figure 4.2 show that the mixture of Mn and Bi at the ratio of 1:1%at. is contained in the quartz tube vertically. The reason for selecting the ratio of 1:1%at. is that the saturation magnetization has a tendency to decrease due to the fact that the magnetic order of Mn element is a paramagnetic phase and is synthesized by vacuum sintering technique. It was found that after the synthesis, a MnBi ingot with a length of about 2 cm and a width of 0.4 cm was obtained, which clearly indicates that this synthesis technique can be used to synthesize LTP-MnBi magnets. It is a simple process, less time-consuming, and energy-saving as well.

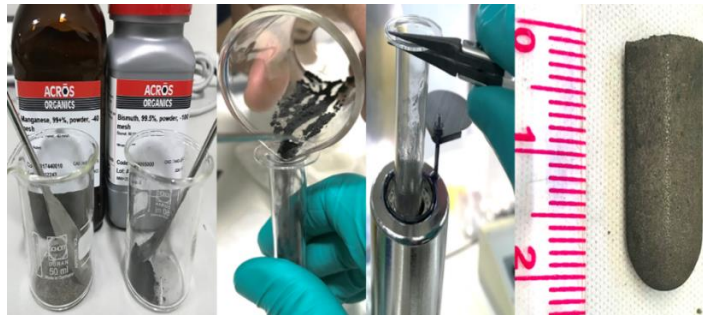
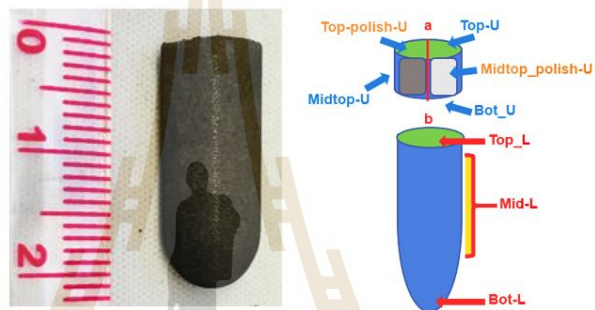
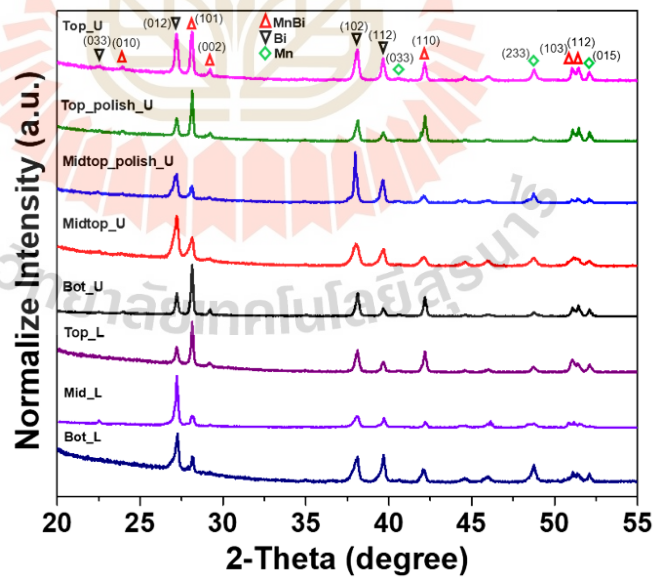


Figure 4.2 MnBi ingot after sintering in vacuum.



(a)



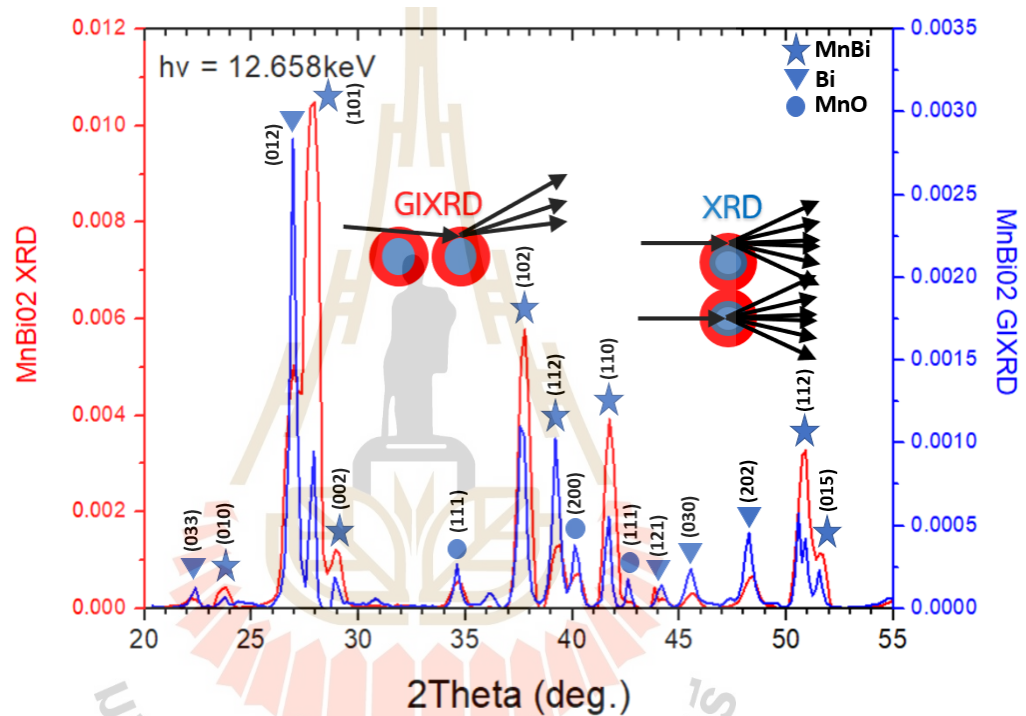
(b)

Figure 4.3 (a) Photo of Mn-Bi Sample after sintering in vacuum at 275 °C and a diagram showing the location on the ingot from where XRD patterns were taken and shown in (b).

Figure 4.3 shows a typical Mn-Bi ingot after sintering in a vacuum at 275 °C and XRD patterns taken from different locations on the ingot sintered at 275 °C for 12 hours. The measured positions are marked as shown in figure 4.3(a). The XRD patterns indicate that there are three main compositions, i.e., LTP-MnBi, Mn and Bi. There are variations in the ratio of the three components at the measured locations. It is interesting to point out that the surface of the sintered Mn-Bi ingot is Bi-rich. It is noted that the quartz tube, Mn-Bi mixture container, was oriented vertically in the effusion cell. During sintering, Mn particles must be immersed in liquid Bi since the sintering temperature is above the melting point of Bi. The amount of detected Bi on the surface of the Mn-Bi ingot is maximum at the bottom and decreases at higher locations. Thus, the outer layer of the sintered Mn-Bi ingot was removed. The remaining part was crushed and ground to be in powder form for further characterization. It is worth noting that no oxides were observed on all samples.

The formation of layers and characterization of MnBi nodules cannot prove that MnBi occurs at the surface by XRD measurements, but it can indicate that it is a component of MnBi due to X-ray radiation being totally penetrating and the angle of incidence is too wide. Therefore, the research group came up with an idea to examine the layers of MnBi pieces using the Grazing incident X-ray diffraction (GIXRD) technique, which was developed to investigate the structure and phase analysis of synthesized magnets. The technique was developed and built at the Beamline 7.2W: MX synchrotron beam system experiment station of the Synchrotron Light Research Institute (Public Organization) using light in the high-energy X-ray region manufactured from 6.5 T Superconducting Wavelength Shifter (SWLS) magnets. The advantage of this technique is that it uses high-intensity synchrotron light and is able to select the appropriate wavelength to avoid energy absorption by the constituent elements of the sample. Another important aspect is that it takes approximately 10 times less measurement time. The X-ray angle of incidence of the sample is rotated by the goniometer. The X-ray is scattered off the sample by an angle of grazing incidence that has a higher value, operate as low as 0.05 degrees, with which GIXRD can reach 0.01-

degree resolution. However, this technique is difficult to adjust the sample height relative to the incident X-ray beam. The application test measures MnBi magnetic samples prepared in this research via mixing Mn and Bi and then sintering in vacuum at 275 °C for 3 hrs and measured in angle of grazing incidence. It found that the structural phase of LTP-MnBi magnets was more effective than the conventional XRD measurement, which was a through-through measurement, resulting in a greater amount of Mn shown in figure 4.4.



**Figure 4.4** XRD curves are measured from magnetic powder MnBi, measured at the BL7.2W: MX optical beam system with two forms of incident X-ray radiation: ricochet (GIXRD) and pass-through (XRD).

The LTP-MnBi magnetic materials synthesis test in this section was blended between Mn and Bi with a ratio of 1:1 %at. Then it was synthesized using a vacuum sintering technique at 275 °C for 3, 6, 9, and 12 hours. In figure 4.5, which shows the XRD patterns of the LTP-MnBi powders, the observed diffraction peaks were similar to those measured from the Mn-Bi ingot, before grinding to powder. No oxides were observed, indicating that ball milling did not cause detectable oxides of Mn or Bi. There

were no obvious big differences in the XRD patterns taken from the samples sintered for different durations. LTP-MnBi and Bi are the major compositions, with a small amount of Mn. The crystal structure of LTP-MnBi with a hexagonal type will have an x-ray diffraction pattern formed at an angle equal to 23.989, 28.136, 29.209, 38.143, 42.195, 49.119, 51.132, 51.486, 52.142, 58.174, 60.568, 66.108, 66.712, 68.383, and 68.681 which related with the plane is (100), (101), (002), (102), (110), (200), (103), (201), (112), (202), (004), (104), (210), (203), and (211) respectively (reference code: 03-065-8164). A detailed investigation of the compositions of the sintered materials was carried out by SEM/EDS measurements.

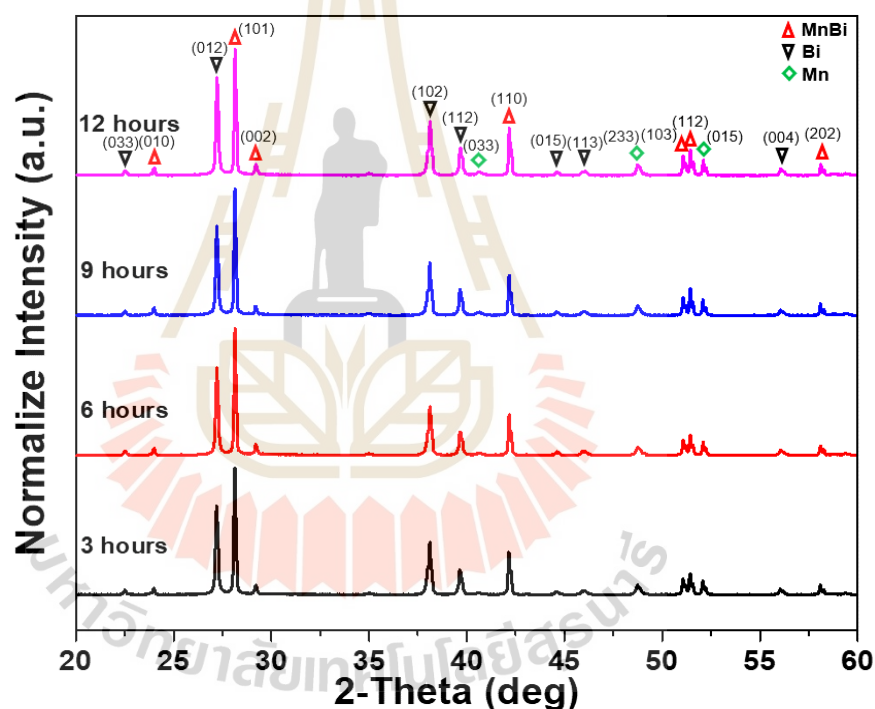


**Figure 4.5** XRD patterns of MnBi powders after sintering in vacuum at 275 °C for 3, 6, 9, and 12 hours.

The morphology of MnBi powder after sintering in a vacuum at 275 °C for 12 hours. The low-resolution SEM image, figure 4.6(a), shows the size distribution of the powder. The particle size is governed by the size of raw Mn powder. Since the sample was sintered just above the melting point of Bi, it is understood that the formation of MnBi occurred by a chemical reaction at the liquid-solid interface. Initially, the Bi

interacts with Mn to form a MnBi layer covering Mn particles. The increase in thickness of the MnBi layer proceeds by the diffusion of Mn through the MnBi layer and, when reaching the liquid-solid interface, reaction with liquid Bi atoms. EDS spectra taken from two different locations on MnBi powder, shown in figure 4.6(b), are plotted in figure 4.6(c) and 4.6(d). The spectrum in figure 4.6(d) is from LTP-MnBi while that in figure 4.6(c) is from Bi. The results from EDS, together with those from XRD, suggest that the sinter materials consist of Bi particles and particles with LTP-MnBi as an outer shell and Mn as an inner core, as shown in figure 4.6.

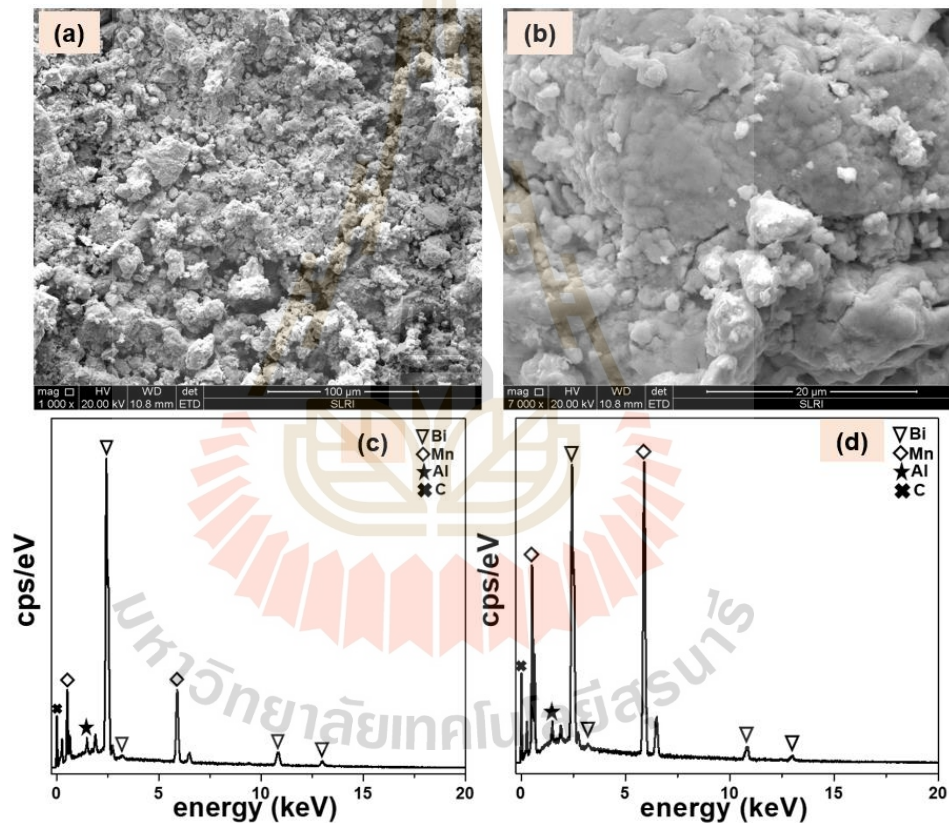


**Figure 4.6** (a) Low- and (b) high-resolution SEM image and (c)-(d) EDS spectra taken from two locations of MnBi powder after sintering in vacuum at 275 °C for 12 hours.

Figure 4.7 shows M-H curves of the sintered LTP-MnBi sample prepared at 275 °C for 3, 6, 9, and 12 hours. The coercivity value ( $H_c$ ) was 2.51, 1.73, 1.36, and 1.57 kOe and the saturation magnetization value ( $M_s$ ) was 42.42, 52.37, 49.79, and 48.57 emu/g respectively. which it is plotted as a function of the sintering time at 275 °C. The sample

sintered for 6 hours exhibits the highest energy product  $(BH)_{\max}$  of 1.7 MGOe, which is much lower than theoretically predicted. The main factor causing low values of the saturated magnetization and energy product is due to the fact that the sintered materials consist of not only the ferromagnetic LTP-MnBi but also paramagnetic Bi and Mn. The materials undergo magnetic purification processes to increase the percentage of LTP-MnBi and thus to improve the performance of the materials.

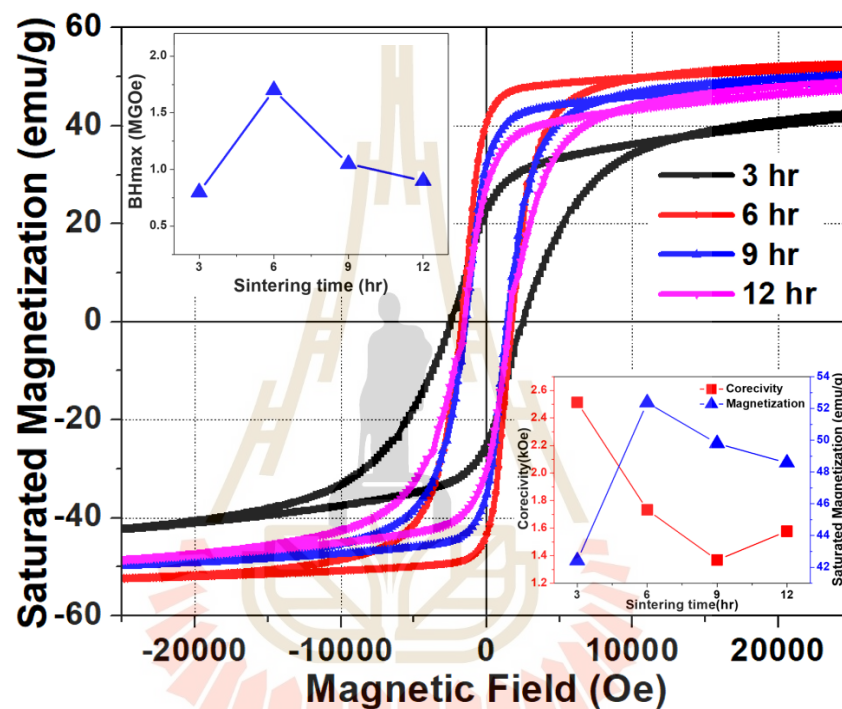


Figure 4.7 M-H curves of 275 °C sintered Mn-Bi sample with different sintering durations. The insets show the maximum energy product (top-left) and coercivity and saturate magnetization (bottom-right).

This work demonstrates that the vacuum sintering technique is capable of synthesizing LTP-MnBi without the formation of oxides. The sintered materials consist of three different materials, i.e., ferromagnetic LTP-MnBi and paramagnetic Bi and Mn. The energy product of the synthesized materials is about 10 times lower than the theoretically predicted value. To improve the performance of the materials, magnetic separation is needed. This will be the subject of further investigations.

### 4.3 Effect of particle size

The sintering of manganese and bismuth powder at temperatures above the melting point of bismuth causes transformation into a liquid state, as a result of which the gravitational flow of the earth penetrates the cracks or gaps of the still solid manganese pellets, creating a surface and chemical interaction between the bismuth liquid and the manganese granules. This results in an LTP-MnBi layer. The thickness of the LTP-MnBi layer tends to increase the time of sintering, which can be calculated using the diffusion relation equation  $D_c=L^2/t$ , where  $t$   $L$  are the diffusion duration time and  $L$  is the diffusion length (thickness of MnBi layers). Therefore, the phase of the sample can be predicted to be composed primarily of LTP-MnBi, Mn and Bi as measured by the XRD technique. The composition of the specimens found after the reaction were LTP-MnBi and Bi, as they were too thick for the x-rays to penetrate, as shown in figure 4.8. The measurement results were divided into two particle size ranges: those smaller than 20 microns (figure 4.8(a)) and those larger than 20 microns (figure 4.8(b)). When observed, the XRD measurements found that the proportion of Bi element or Bi rich was found to be more common in the LTP-MnBi particle range of less than 20 microns, and the peak intensities of LTP-MnBi have increased with the rise of the temperature.

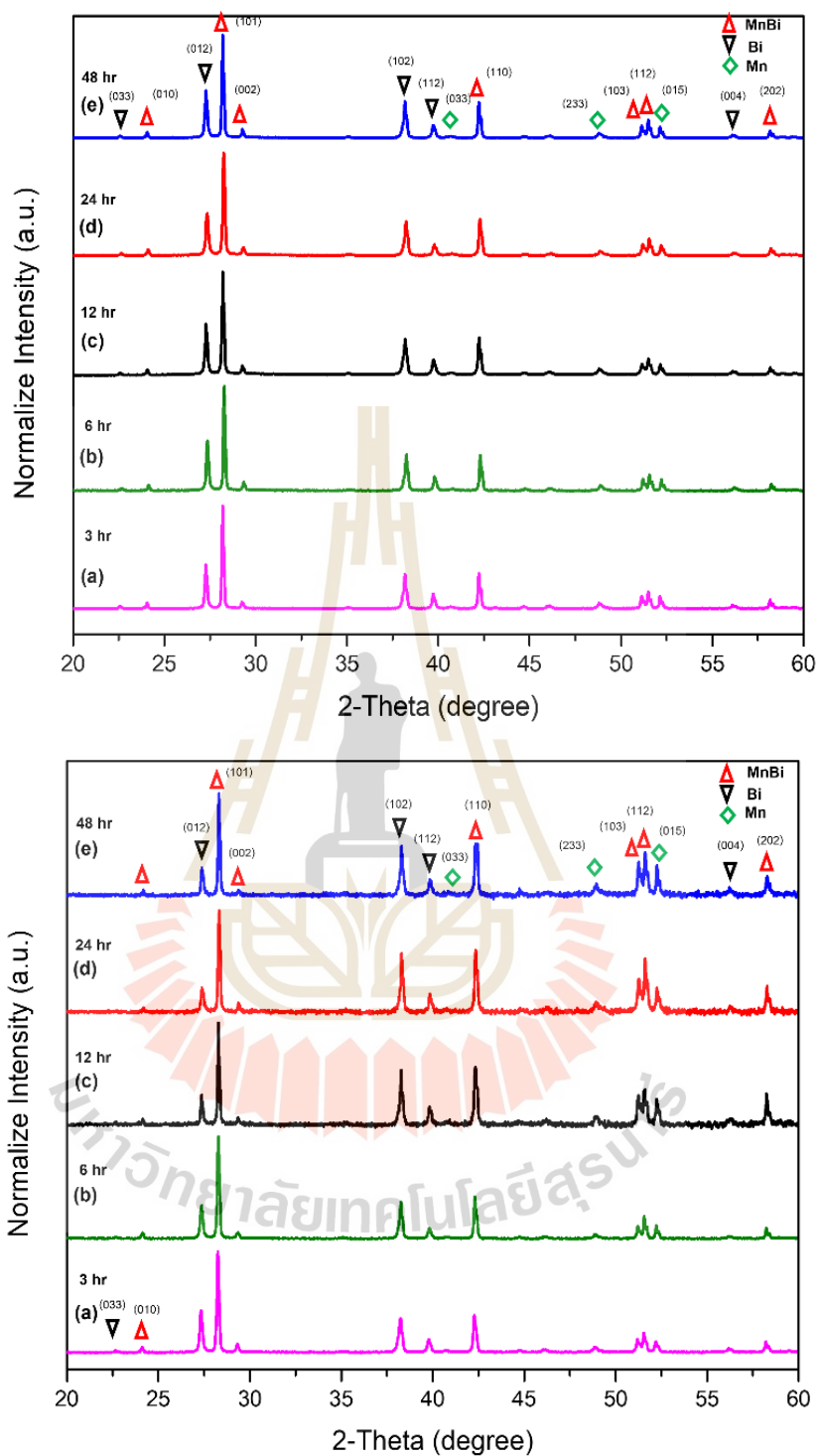


Figure 4.8 XRD patterns of MnBi at 275 °C for 12 hours with particle size of (Top) < 20 μm and (bottom) 20-53 μm.

It is known that MnBi has two phases i.e. the High Temperature Phase (HTP)-MnBi and the Low Temperature Phase (LTP). The MnBi magnetic materials sintered under vacuum at 275 °C for 3 hours and 48 hours (6, 12, and 24 hours, similar) were found to be a Low Temperature Phase (LTP)-MnBi type when compared to the database. The bismuth manganese reference code: 03-065-8164 has the diffraction peaks at 28.136°, 38.143°, 42.195°, 51.132°, 51.486°, 52.142°, 58.174°, and 60.568°, respectively, as shown in figure 4.9.

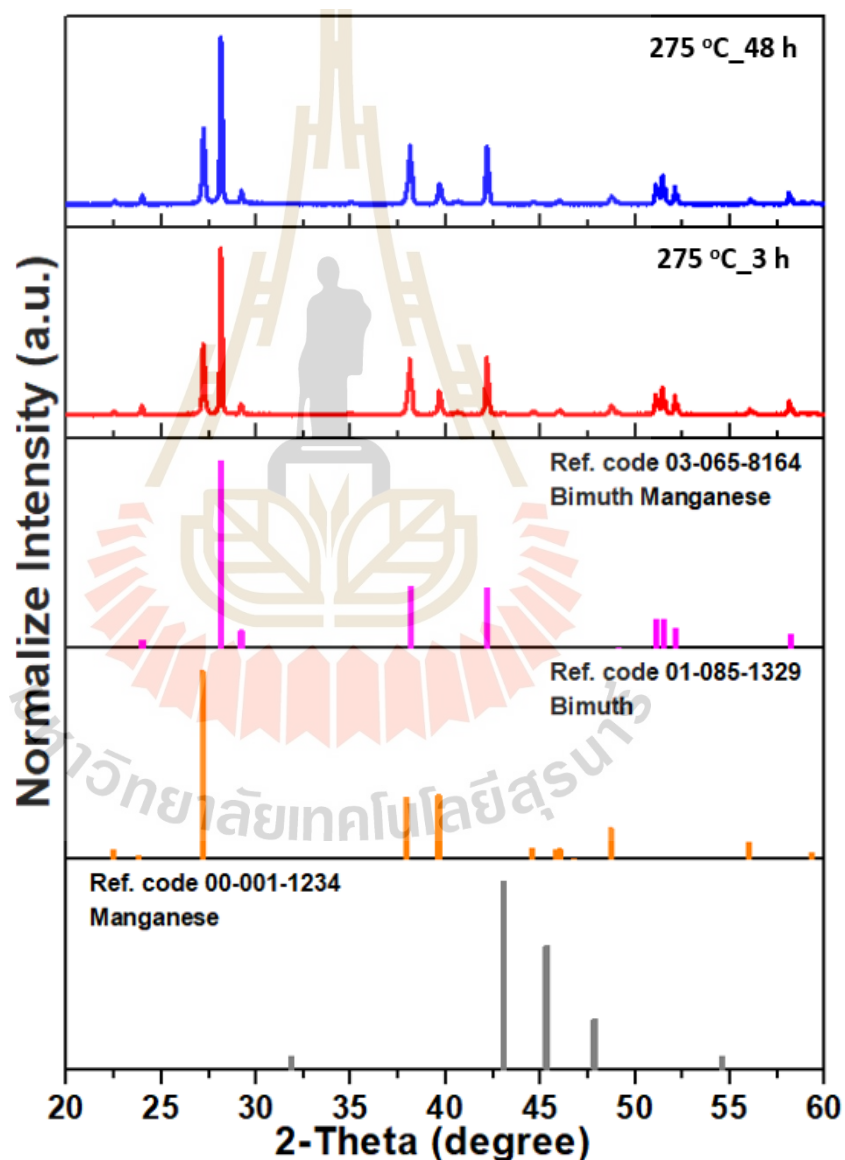


Figure 4.9 XRD patterns of MnBi powder obtained after sintering in vacuum at 548 K for 3 and 48 hours compared with database of MnBi, Bi and Mn phase.

In this research, the Vibrating Sample Magnetometer (VSM) is a technique used to study the magnetic properties of LTP-MnBi magnets. The results of the magnetic property measurements in this section are shown as hysteresis loops or M-H curves, which the magnitude of the induced substance is represented by magnetization ( $M_s$ ) in the y-axis and the magnetic field strength is represented by coercivity ( $H_c$ ) in the x-axis. From the figure 4.10, demonstrating the M-H curve of LTP-MnBi particles synthesized by the vacuum sintering technique at 275 °C for 3, 6, 12, 24, and 48 hours, subsequently, the particle size less than 20 microns and the particle size in the range of 20-53 microns were selected. The LTP-MnBi magnetic particles were smaller than 20 microns, the coercivity ( $H_c$ ) was  $4.95 \pm 0.07$ ,  $5.46 \pm 0.09$ ,  $5.03 \pm 0.13$ ,  $5.16 \pm 0.10$ , and  $4.96 \pm 0.08$  kOe, and the saturation magnetization ( $M_s$ ) was  $38.72 \pm 0.60$ ,  $40.04 \pm 0.73$ ,  $40.19 \pm 0.81$ ,  $41.21 \pm 0.92$ , and  $42.59 \pm 0.95$  emu/g. For LTP-MnBi magnetic particles with sizes in the range of 20-53 microns, the coercivity ( $H_c$ ) was  $2.90 \pm 0.07$ ,  $3.11 \pm 0.06$ ,  $2.53 \pm 0.09$ ,  $2.42 \pm 0.05$ , and  $2.28 \pm 0.08$  kOe, and the saturation magnetization ( $M_s$ ) was  $45.69 \pm 0.90$ ,  $48.20 \pm 0.95$ ,  $44.68 \pm 0.66$ ,  $49.93 \pm 0.75$  and  $49.72 \pm 0.77$  emu/g respectively. Considering the temperature hold,  $M_s$  tends to rise with increased hold time and the coercivity value has slightly transitioned. The difference in M-H curves is due to the magnetic domain of the particle size. Figure 4.10 show the coercivity and magnetization values are plotted as a function of the sintering time (hours).

The coercivity value ( $H_c$ ) of 5.35 kOe of the particle size less than 20 microns and the particle size greater than 20 microns has a maximum coercivity value of 2.91 kOe. We found that there was a slight increase in the change with holding the temperature at 275 °C for 3, 6, 12, 24, and 48 hours, which is insignificant. When considering the coercivity value ( $H_c$ ) and the saturation magnetization value ( $M_s$ ) from fig. 4.10, the maximum energy product  $(BH)_{max}$  of the specimen was calculated. It was initially found that LTP-MnBi particles less than 20 microns, the  $(BH)_{max}$  were  $1.29 \pm 0.05$ ,  $1.36 \pm 0.07$ ,  $1.71 \pm 0.08$ ,  $1.65 \pm 0.05$ , and  $1.49 \pm 0.06$  MGOe, held at 275 °C for 3, 6, 12, 24, and 48 hours, respectively. Until the temperature was maintained for 12 hours, the highest  $(BH)_{max}$  was obtained at  $1.71 \pm 0.08$  MGOe, as shown in figure 4.11. And since the

different melting points of Mn (1,246 °C) and Bi (271 °C), which in the vacuum during heating to more than the melting point of Bi, results in the Bi transforming to the liquid state. The Mn surrounded by the liquid state of Bi causes a portion of the Mn to be isolated due to peritectic reactions to the interaction to form MnBi layers.

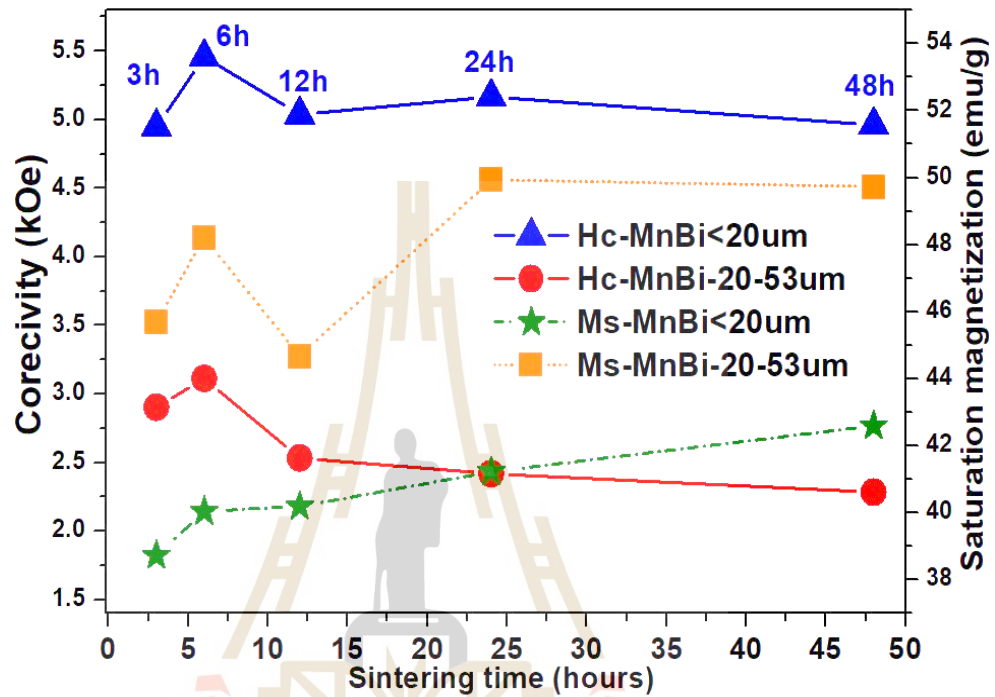


Figure 4.10 shows the magnetic properties of MnBi particles size of < 20  $\mu\text{m}$  and 20-53  $\mu\text{m}$ .

During the formation of MnBi magnetic materials, these reactions result in the formation of oxides. Therefore, it has been shown that sintering in a vacuum at 275 °C for 12 hours is optimal if the temperature is held longer than 12 hours, which will degrade the magnetic properties. However, the LTP-MnBi magnetic particles with sizes in the range of 20-53 microns tended to be in line with the same trend as shown in figure 4.11.

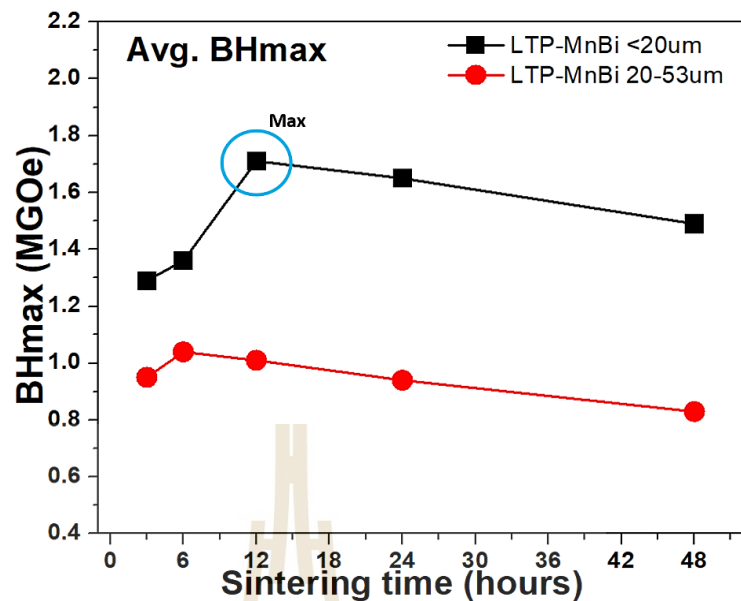


Figure 4.11 shows the maximum energy product  $(BH)_{max}$  of LTP-MnBi particles size of  $< 20 \mu\text{m}$  and  $20\text{-}53 \mu\text{m}$ .

#### 4.4 Effect of pressure during sintering

The samples sintered at different pressures were categorized by base pressure denoted as ultra-high vacuum (UHV,  $10^{-8}$  mbar), low vacuum (LV,  $10^{-2}$  mbar), and ambient pressure (AP, 1 bar). Figure 4.12(a) shows the wide scan XRD patterns of all MnBi powders whose main diffraction peaks could be identified as MnBi phase (JCPDS Card. No. 96-900-8900), Bi phase (JCPDS Card. No. 01-085-1329), cooperated with small peaks of Manganese oxides (MnO; JCPDS Card. No. 96-101-0394,  $\alpha$ -MnO<sub>2</sub>; JCPDS Card. No. 44-0141 and  $\beta$ -MnO<sub>2</sub>; JCPDS Card. No. 024-0735). The MnBi/(MnBi+Bi) ratio extracted from the XRD peaks were calculated to be 54.9, 54.5, and 70.6% for UHV-MnBi, LV-MnBi and AP-MnBi, respectively. It should be noted that this ratio does not fully represent the MnBi concentration in the sample. Since the Mn peaks could not be detected due to the limit of X-ray penetration. It could be implied that the MnBi concentration in the Mn-rich AP-MnBi (the sample was taken from the MnBi (black) region shown in figure 4.12(a) might be far less than this value. As expected, the oxidation rate depends on the oxygen partial pressure during sintering (Li et al., 2018)

and thus, the lowest number of oxides is observed for the UHV-MnBi. It is noted that  $\alpha$ -MnO<sub>2</sub> and  $\beta$ -MnO<sub>2</sub> are pronounced for the sample sintered in a low vacuum, i.e., LV-MnBi sample. These oxides are formed on the surface of the MnBi powder particles. The quantitative comparison of surface oxides composition could be further investigated by the XPS technique.

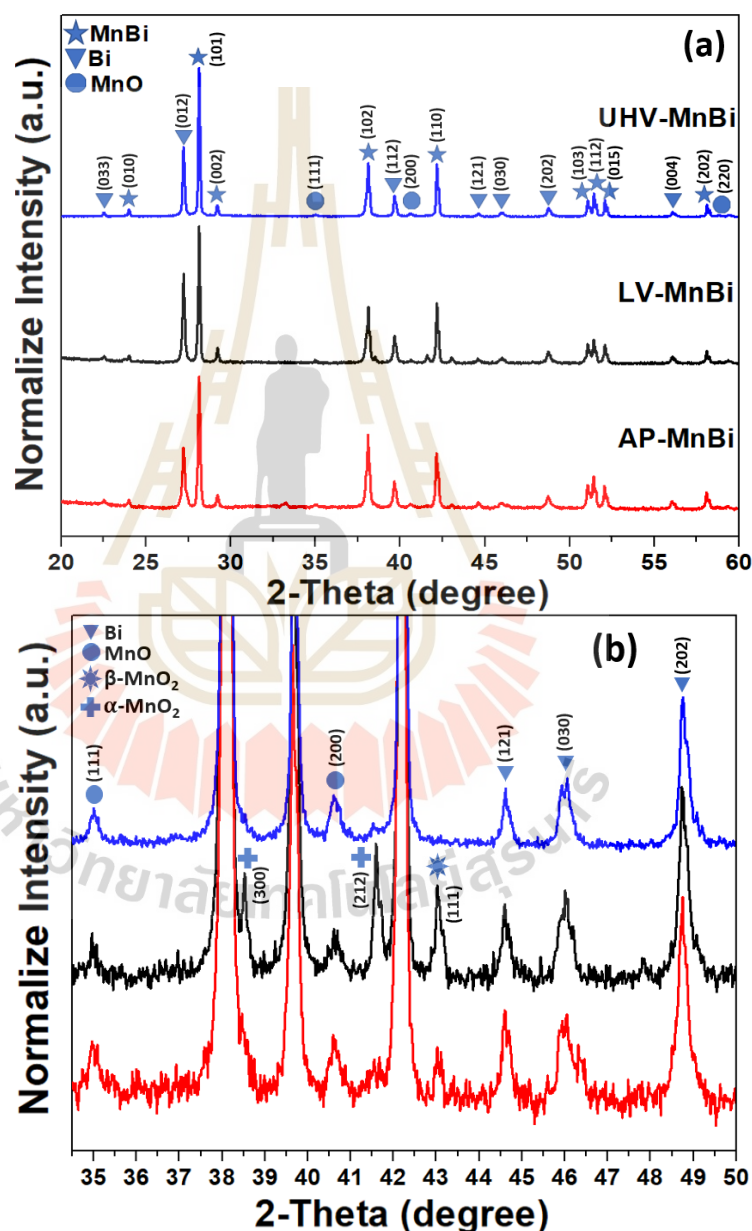


Figure 4.12 XRD patterns of (a) UHV-MnBi, LV-MnBi and AP-MnBi and (b) Zoom in: 2-theta range of 34.5°-50.0°.

Firstly, the M-H curves were corrected by using a demagnetization factor ( $N$ ) which is dependent on the shape and orientation of the ferromagnetic materials to the external field. This can be calculated by,  $N^{-1} = 2 + \frac{1}{\sqrt{2}} \frac{a}{b}$ , according to the transverse-cylindrical geometry (Prozorov et al., 2018). The  $N$  value of 0.4 was calculated from  $\frac{a}{b} = \frac{1}{\sqrt{2}}$ , where  $a$  is a length and  $b$  is a diameter of the sample. Figure 4.13(a) shows the room temperature hysteresis loop of the sintered MnBi specimens prepared at 375°C for 12 hours under ultra-high vacuum (UHV), low vacuum (LV), and ambient pressure (AP). The changes of demagnetization curves of raw  $M$  ( $N = 0$ ) and corrected  $M$  ( $N = 0.4$ ) of UHV-MnBi are seen in the bottom-right inset of figure 4.13(a). The magnetic measurements were repeated 3 times in each sample giving the corrected  $H_c$  of  $2.42 \pm 0.07$ ,  $0.68 \pm 0.06$ , and  $0.87 \pm 0.04$  kOe and  $M_s$  of  $48.46 \pm 0.90$ ,  $56.54 \pm 0.95$ ,  $49.80 \pm 0.66$  emu/g for UHV-MnBi, LV-MnBi and AP-MnBi samples, respectively (summarized in Table 1). It should be noted that the UHV-MnBi exhibits the hard magnetic behavior with up to 3.5 times of  $H_c$  compared to LV-MnBi and AP-MnBi. Even the slightly less  $M_s$  value of UHV-MnBi (up to 14% compared to the LV-MnBi) consistent with the observed MnBi concentration measured from XRD, the UHV-MnBi remains the highest  $(BH)_{max}$  of  $1.82 \pm 0.05$  MGOe among others which is due to its notably high  $H_c$  as shown in figure 4.13(b).

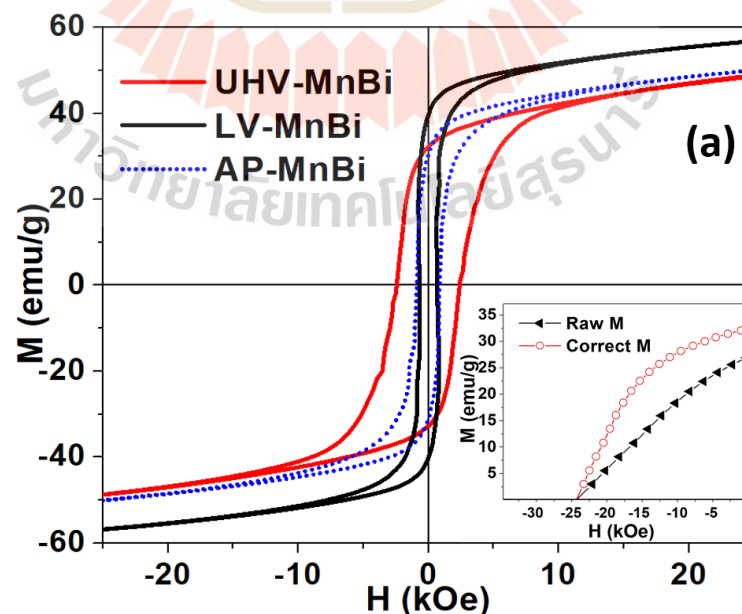
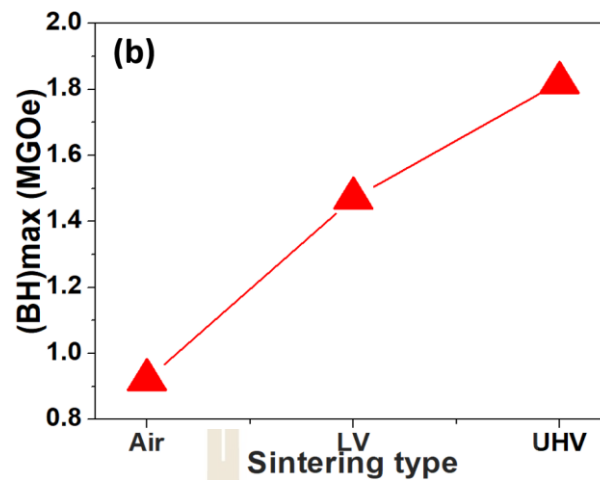


Figure 4.13 (a) M-H curves after demagnetizing field correction of UHV-MnBi, LV-MnBi and AP-MnBi.



**Figure 4.13** (Continued)(a) M-H curves after demagnetizing field correction of UHV-MnBi, LV-MnBi and AP-MnBi.

The inset of (a) shows the demagnetization curves of raw M ( $N = 0$ ) and correct M ( $N = 0.4$ ) of the UHV-MnBi (bottom-right). (b) shows the maximum energy product ( $(BH)_{\max}$ ) of all samples.

**Table 4.1** Magnetic properties of different pressure samples.

Samples	$H_c$ (kOe)	$M_s$ (emu/g)	$(BH)_{\max}$ (MGOe)
UHV-MnBi	2.42 ± 0.07	48.46 ± 0.90	1.82 ± 0.05
LV-MnBi	0.68 ± 0.06	56.54 ± 0.95	1.47 ± 0.08
AP-MnBi	0.87 ± 0.04	49.80 ± 0.66	0.92 ± 0.04

Figures 4.14(a) and 4.14(e) show the physical appearances of AP-MnBi and UHV-MnBi ingot obtained immediately after the sintering process. It is clearly seen that the AP-MnBi is inhomogeneous with noticeably separated layers of Bi (white region) and MnBi (black region) which are shown in the inset of (figure 4.14(a)), while the UHV-MnBi ingot is relatively homogeneous. It is understood that the formation of MnBi by a chemical reaction at the liquid phase sintering (LPS) (German et al., 2009) and atmospheric pressure. Initially, the Bi liquid reacts with Mn particle powders to form a MnBi layer coating Mn inner core. Moreover, the atmospheric pressure is an important

factor that suppresses the MnBi formation due to the oxide formation. The high-resolution SEM images of AP-MnBi ingot are shown in figure 4.14(b). It is confirmed that the surface composition is inhomogeneous, as shown in the EDS results in figure 4.14(c) and (d). It was found that the top area and surface of the as-sintered AP-MnBi are Bi-rich and oxygen-rich (Yoshida et al., 1999). This could be explained by the incomplete formation and hindering of the MnBi phase during sintering in the ambient condition either by the formation of oxides or peritectic reaction. The Mn:Bi:O ratio of 40.8:33.6:21.2 and 16.2:67.2:10.4 %wt were observed in the black and white regions of AP-MnBi. While the ratio of 45.2:44:4.9 and 33.2:54.1:9.2 were carried out from region 1 and 2 of the UHV-MnBi. This result strongly confirms the more homogeneous and less oxides coverage of the UHV-MnBi than AP-MnBi.

This work demonstrates the success in preparing MnBi in ultra-high vacuum, low vacuum, and ambient pressure. The vacuum pressure plays an important role in the formation of MnBi during liquid phase sintering (LPS). After the sintering process, the AP-MnBi ingot is inhomogeneous, containing the separated layers of Bi and MnBi, while the UHV-MnBi ingot is rather homogeneous. The formation of different kinds of oxides is found in LV-MnBi and AP-MnBi more than in UHV-MnBi. Thus, it could be concluded that the inhomogeneity and oxides play an important role in the magnetic properties of MnBi. UHV-MnBi presented the highest  $(BH)_{\max}$  of up to  $1.82 \pm 0.05$  MGOe. Finally, we showed here that the MnBi can be prepared even in atmospheric pressure. However, further studies and system optimization are required to obtain acceptable magnetic performance.

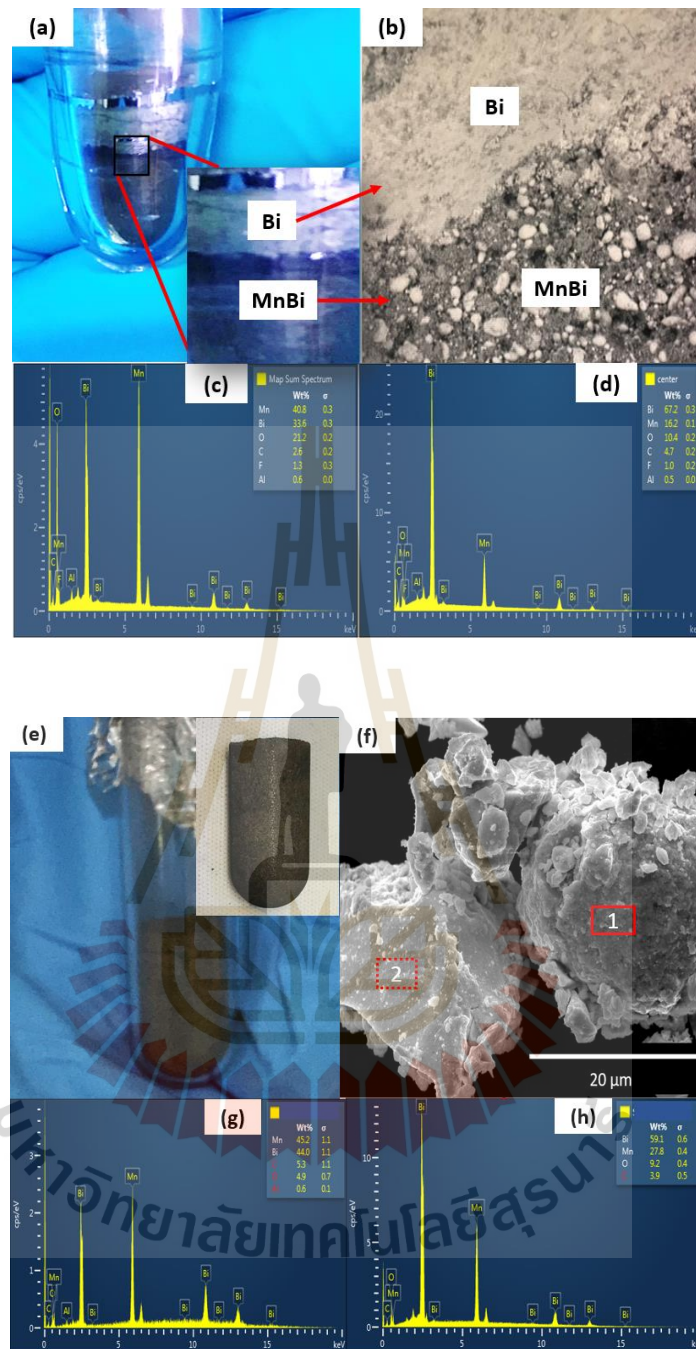


**Figure 4.14** (a) camera image (b) high-resolution SEM images (c) EDS spectra taken at MnBi region (black region) and (d) Bi region (white) of AP-MnBi ingot. (e) camera image (f) high-resolution SEM images (g) EDS spectra taken at region 1 and (h) region 2 of UHV-MnBi ingot.

#### 4.5 Effect of prolonged ball milling

Ball-milling was used, in this work, for reducing the particle size of the Mn powder before the sintering processes. Longer milling time, small particle size was expected. The Mn particle distributions as a function of ball milling time measured by SEM are shown in figure 4.15(a)-(d). It is seen that the shapes of Mn particles are similar in all ball-milled samples containing circular shapes of small and big particles. Some big particles are formed by small particles. The particle size is  $8.02 \pm 0.44 \mu\text{m}$  for 3 hr ball-milled samples. The particle size decreases to  $5.81 \pm 0.81 \mu\text{m}$  for 7hr ball milling time. The particle size gradually decreases after longer grinding time.

The magnetic properties of MnBi materials were shown by M-H curves measured at 300 K. MnBi magnetic materials were prepared with Mn particles treated via ball milling technique. It was found that the  $H_c$  value were  $4.28 \pm 0.07$ ,  $3.98 \pm 0.06$ ,  $3.87 \pm 0.04$  and  $4.02 \pm 0.09$  kOe,  $M_s$  value were  $53.42 \pm 0.90$ ,  $50.95 \pm 0.95$ ,  $48.87 \pm 0.66$  and  $44.32 \pm 0.72$  emu/g and  $(BH)_{\text{max}}$  value were  $1.98 \pm 0.05$ ,  $1.89 \pm 0.08$ ,  $1.86 \pm 0.04$  and  $1.59 \pm 0.07$  MGOe for MnBi-M3, MnBi-M7, MnBi-M11 and MnBi-M15, respectively, as shown in figure 4.16(a) and Table 2. The coercivity value ( $H_c$ ) are similar, while the saturation magnetizations ( $M_s$ ) are slightly decreased as ball milling time increases. The  $M_s$ ,  $H_c$  and  $(BH)_{\text{max}}$  are summarized in figure 4.16. It is noteworthy that the MnBi-M3 exhibit the highest  $(BH)_{\text{max}}$ . The squareness ratio ( $M_r/M_s$ ) of MnBi sample indicates that the energy product  $(BH)_{\text{max}}$  trend should be decreased. In figure 4.16(b), the  $(BH)_{\text{max}}$  is plotted as a function of the Mn ball milling time (hours) and it has different value about 5-25%. The saturation magnetization ( $M_s$ ) value tends to decrease with Mn ball milling time. Magnetic properties slightly change. This means the products are similar (does not affect to phase transition). This result shows that ball milling time affect to the decreases of overall magnetic properties of MnBi.

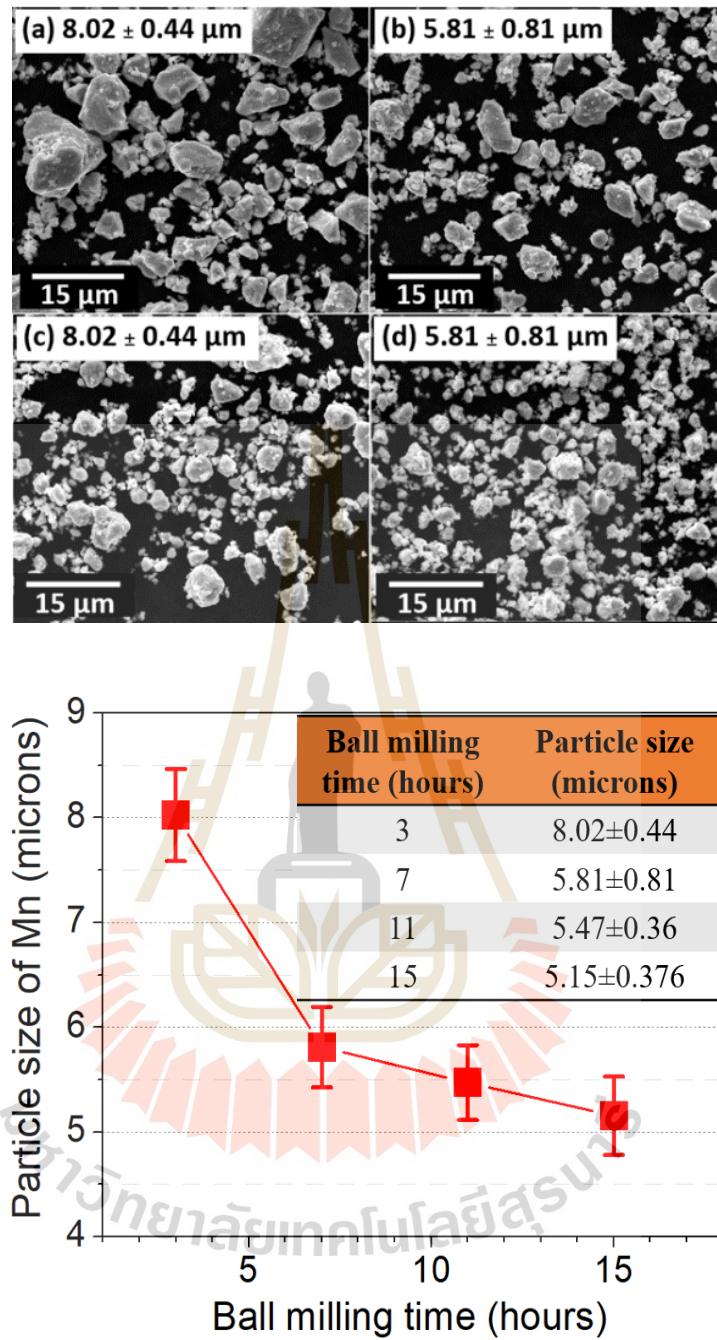


**Figure 4.15** The low-resolution SEM images of Mn ball milling (a) 3 hours, (b) 7 hours, (c) 11 hours and (d) 15 hours. The average Mn particle size are shown in the right figure.

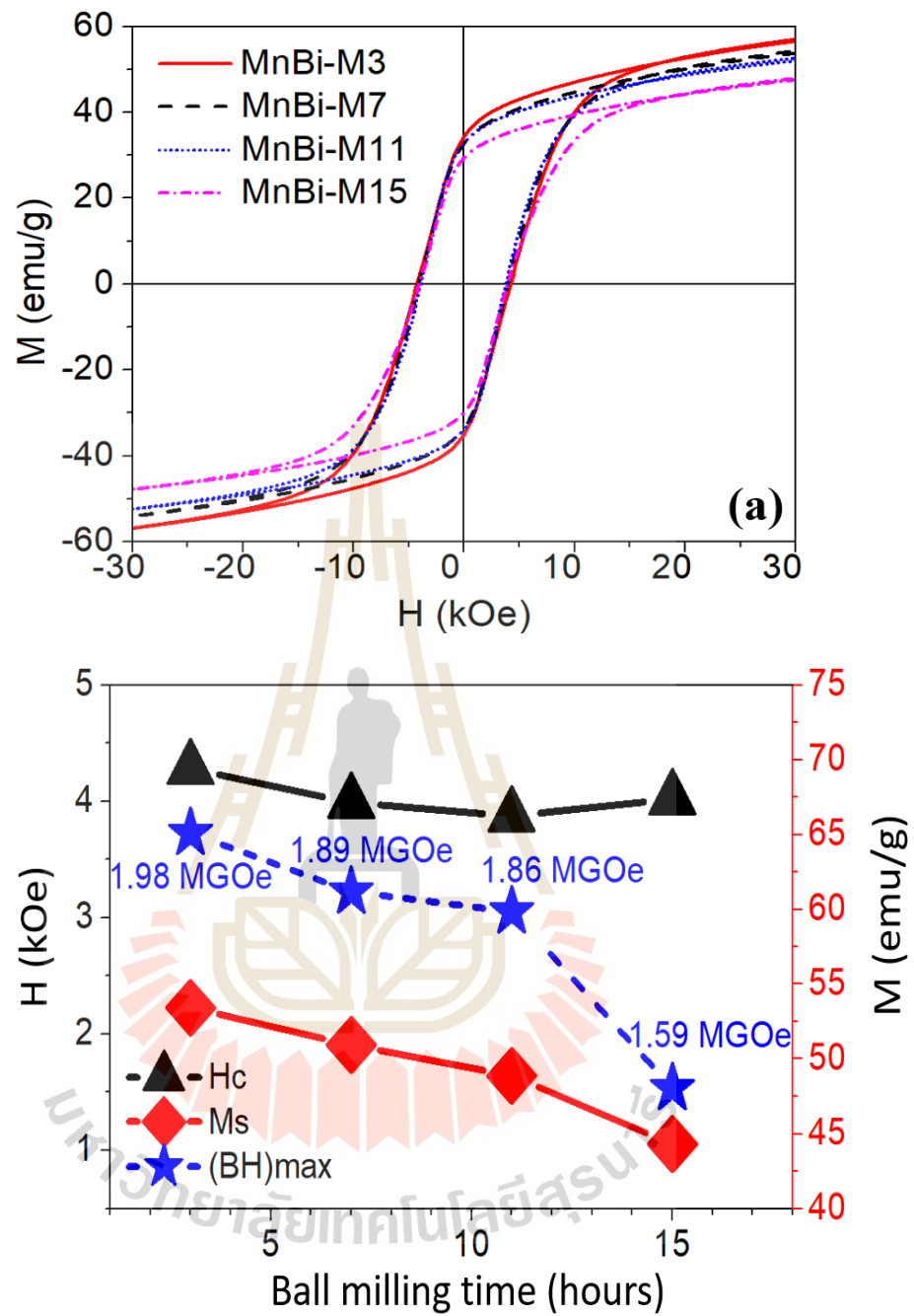
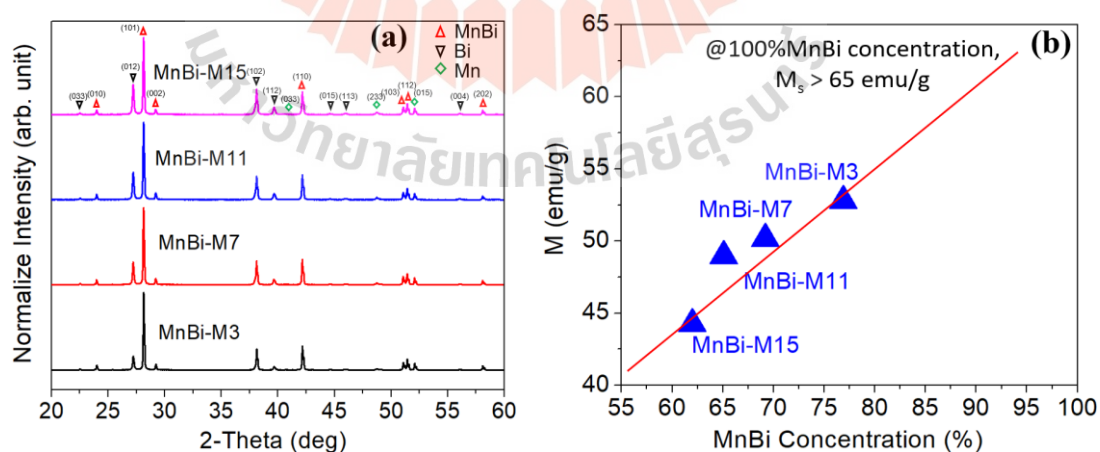


Figure 4.16 (a) shows the M-H curves of the sintered samples prepared using Mn powder particle from ball milling different time and (b) magnetic properties of MnBi powder.

**Table 4.2** Magnetic properties of MnBi using Mn grinding time samples.

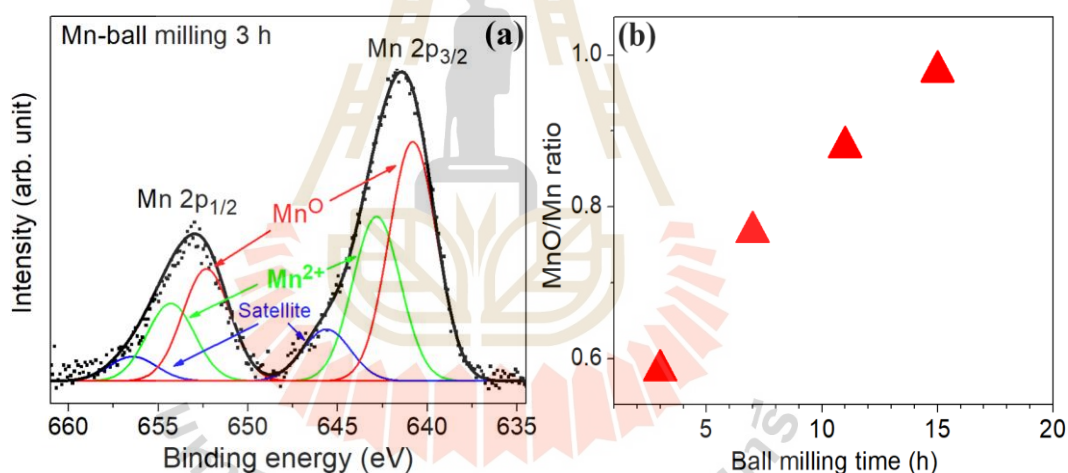
Samples	$H_c$ (kOe)	$M_s$ (emu/g)	$(BH)_{max}$ (MGOe)
MnBi-M3	$4.28 \pm 0.07$	$53.42 \pm 0.90$	$1.98 \pm 0.05$
MnBi-M7	$3.98 \pm 0.06$	$50.95 \pm 0.95$	$1.89 \pm 0.08$
MnBi-M11	$3.87 \pm 0.04$	$48.87 \pm 0.66$	$1.86 \pm 0.04$
MnBi-M15	$4.02 \pm 0.09$	$44.32 \pm 0.72$	$1.59 \pm 0.07$

Figure 4.17 shows the XRD patterns of the MnBi powders after sintering in vacuum at 275 °C for 12 hrs. The MnBi (JCPDS Card. No. 96-900-8900) and Bi (JCPDS Card. No. 01-085-1329) phases were found. A small fraction of the Mn phase can be measured because the Mn particles were covered by the layers of MnBi and Bi that remains after the reaction. The peak intensities of Bi increase with Mn ball milling time. When considering the MnBi content, it is indicated that the highest MnBi content is MnBi-M3. From the extrapolation, if the sample possesses the 100% of MnBi phase, the  $M_s$  value will be up to 70 emu/g. By this assumption, the  $(BH)_{max}$  can be increased by enhancing the MnBi purity.



**Figure 4.17** (a) XRD patterns of MnBi powders after sintering in vacuum at 275 °C for 12 hours (b) the magnetization ( $M_s$ ) as a function of MnBi concentration. Red line shows the extrapolation of  $M_s$ .

Figure 4.18(a) shows the XPS spectrum of the Mn 2p core level of the 3-hr-milled Mn particles as a demonstration. By fitting those peaks with Gaussian functions, each Mn peak can be deconvoluted into three peaks which are the Mn<sup>2+</sup> (or MnO) shown by the green spectrum, metallic Mn (red spectrum) and the satellite peak (blue spectrum). It is intriguing to note that the spectrum for both Mn 2p<sub>3/2</sub> and Mn 2p<sub>1/2</sub> were split into two peaks indicating the presence of the regular Mn atom and interstitial states, respectively. Hence, the binding energy of 642.2 eV and 654.3 eV were attributed to the Mn atoms in regular states, while the peaks of 641.1 eV and 653.3 eV were attributed to the interstitial Mn atoms of MnBi sample. Figure 4.18(b) shows the MnO/Mn ratio extracted from XPS at different ball milling time. It is seen that the MnO content increase with Mn ball-milling time.



**Figure 4.18** (a) XPS spectra of Mn ball milling for 3 hours and (b) MnO/Mn ratio with ball milling time.

This work demonstrates that the size of the Mn powder particle reduces as a function of ball milling time. Mn oxide is formed during the ball milling process. The amount of the oxide increases with milling time, which demonstrates the increment of MnO content on the surface of Mn particles, resulting in the hindering of MnBi formation. The formation of oxide should be the key role in the decrement of MnBi

content. It is worth noting that oxides should be removed to enhance the MnBi content and thus the magnetic properties of the sintered product.

Figure 4.19 depicts the MnBi powder morphology after sintering in vacuum at 275 °C for 12 hours using Mn ball milling for 3 hours as a component (it does not depict Mn ball milling for 7, 11, and 15 hours as a component because it is similar). The low-resolution SEM image, figure 4.19(a), shows the size distribution of the MnBi sample. The particle size of the MnBi sample is dominated by the size of the raw Mn powder. Since the sample was heated over the melting point of Bi, it has become a liquid state. The Bi (liquid state) is governed by the particle size of raw Mn powder. Bi interacts with Mn to form an MnBi layer covering Mn particles by the chemical reaction at the liquid–solid interface. It is seen that the particle trend to agglomerate is shown in Fig 4.19(b). The increased thickness of the MnBi layer by the diffusion method of Mn (solid state) through reaction with Bi atoms becomes the MnBi layer. However, it is very difficult to obtain the high purity of the MnBi phase. Furthermore, it is understood that the small particle trend has a higher packing density than the larger ones. So, this should be the reason why we see more Bi on the XRD pattern in figure 4.19.

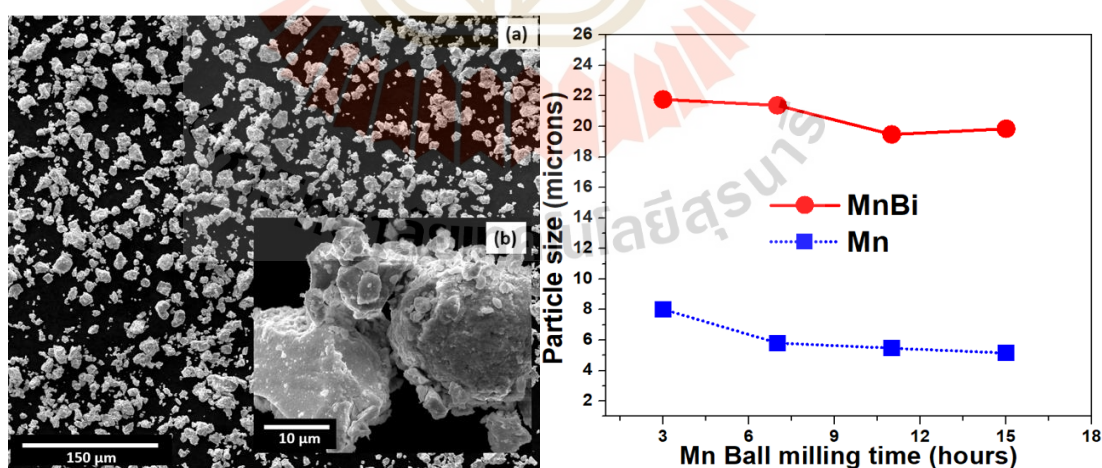
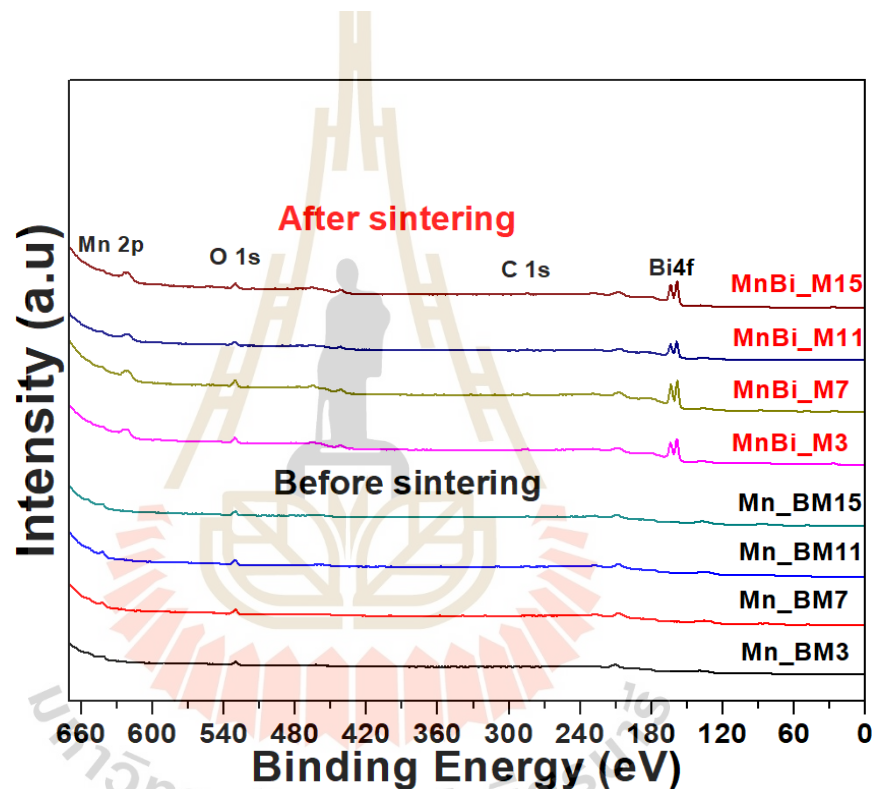


Figure 4.19 shown the distribution of the MnBi powder after sintering in vacuum after sintering in vacuum at 275 °C for 12 hours.

The wide scan spectra of the specimens both before and after sintering show the expected elements whose surface electronic states and the chemical compositions were achieved from x-ray photoelectron spectroscopy (XPS) measurement, demonstrated in figure 4.20, where the position of Mn2p, O1s, C1s, and Bi4f is evidence that indicates that without any element of the impurity, the formation of the Manganese-Bismuth-Oxygen composite, which in figure 4.20, also shows the difference in the chemical composition of the before and after sintering of the sample.



**Figure 4.20** XPS spectra of Mn ball milling different time and MnBi sample after sintering in vacuum at 275 °C for 12 hours.

#### 4.6 Influence of glycine

In this work, glycine was added, which has properties as a lubricant and a surfactant in the process of grinding Mn powder for 1 and 3 hours, it was found that the original Mn powder particle size was larger than 400 microns. They were approximately 10-11 times smaller to  $35.70 \pm 0.43$  microns and  $24.81 \pm 0.31$  microns after 1 and 3 hours of reduction, respectively. It was obvious that there will be a glycine

coating on the granules of both small and large Mn particles, clearly separated. As illustrated in figure 4.21.

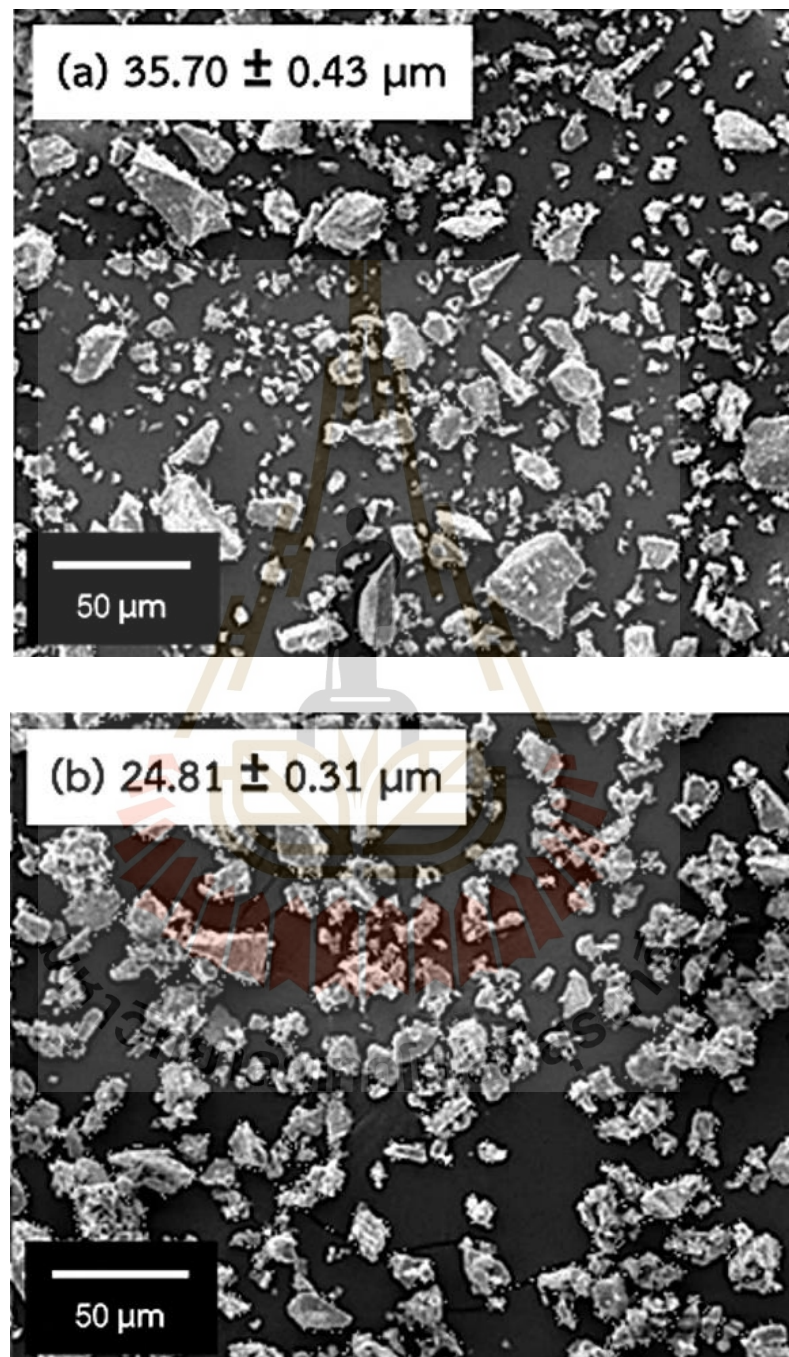


**Figure 4.21** Morphology of glycine-added Mn powder in ball milling for (a) 1 hour and (b) 3 hours.

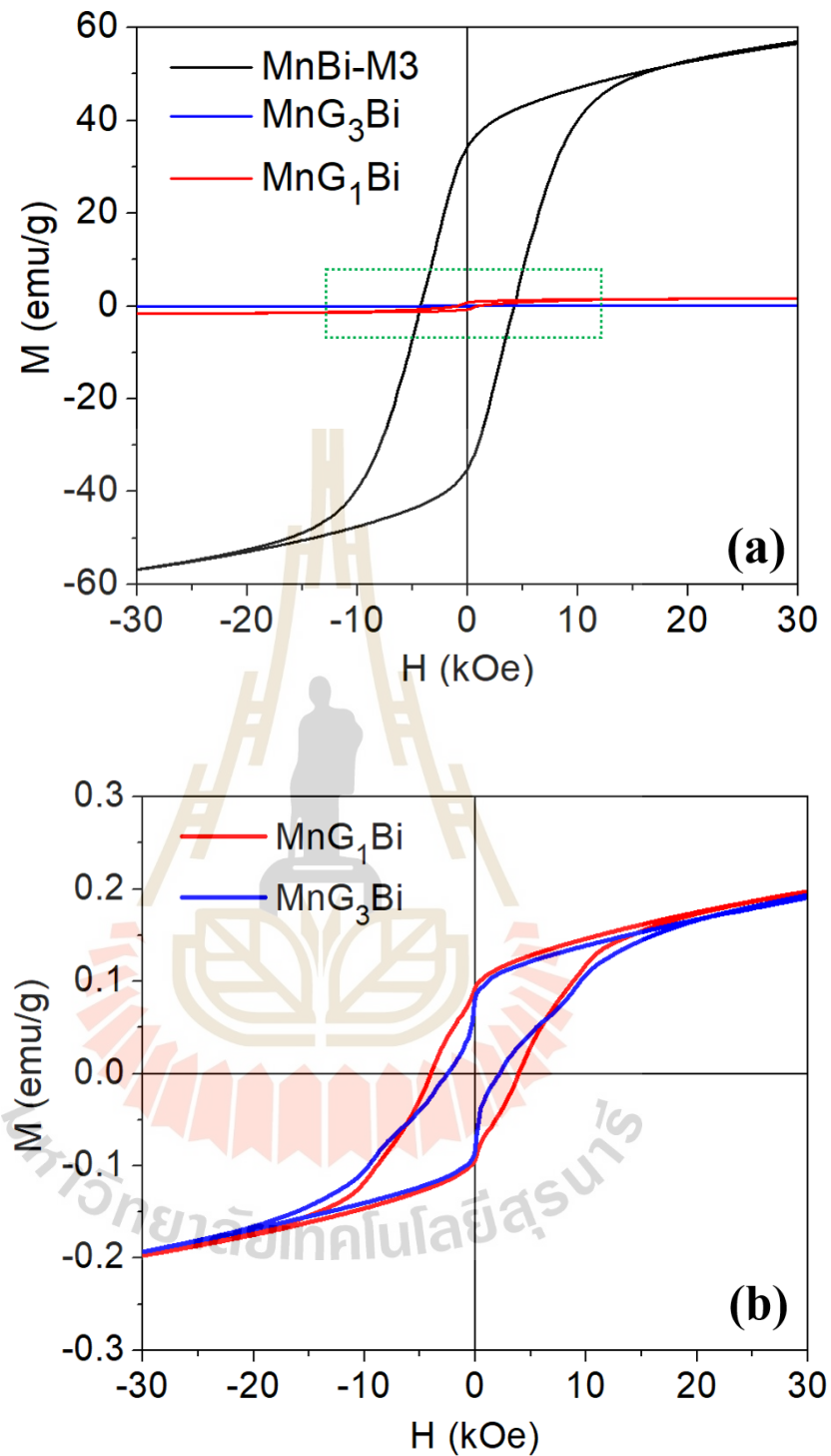


**Figure 4.22** The M-H hysteresis loop of (a) the MnBi prepared from conventional ball milling (MnBi\_M3) and (b) the glycine addition for 1 hours (MnG<sub>1</sub>Bi) and 3 hours (MnG<sub>3</sub>Bi).

Magnetic properties as measured by the VSM technique at 300 K of conventional ball milled MnBi materials and grinding in glycine for 1 and 3 hours are shown in figure 4.22. It was found that the conventionally ground MnBi showed magnetization ( $M_s$ ) and coercivity ( $H_c$ ) values of  $52.85 \pm 0.70$  emu/g and  $4.8 \pm 0.06$  kOe, respectively. On the other hand, the glycine added MnBi materials showed the  $H_c$  values of  $3.95 \pm 0.04$  and  $2.35 \pm 0.03$  kOe, and  $M_s$  of  $0.18 \pm 0.73$  emu/g, for  $MnG_1Bi$  and  $MnG_3Bi$ , respectively (shown in figure 4.22(b)). These values are considered to be significantly reduced compared to those obtained by conventional ball milling. The reason of the low magnetic value of glycine added MnBi material is the main focus of this study.

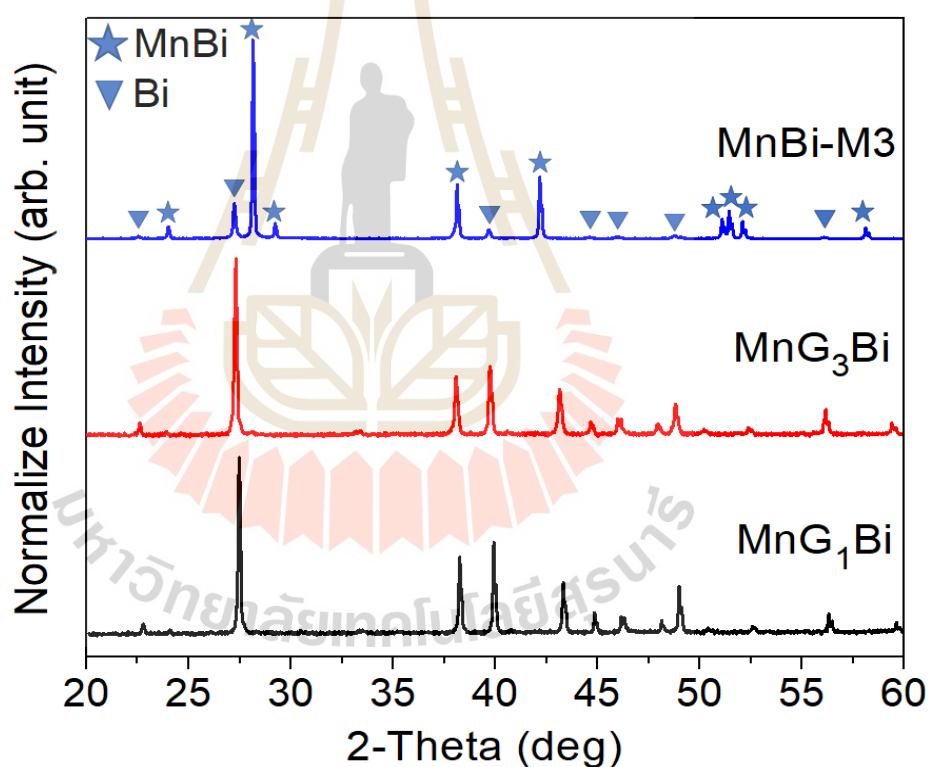
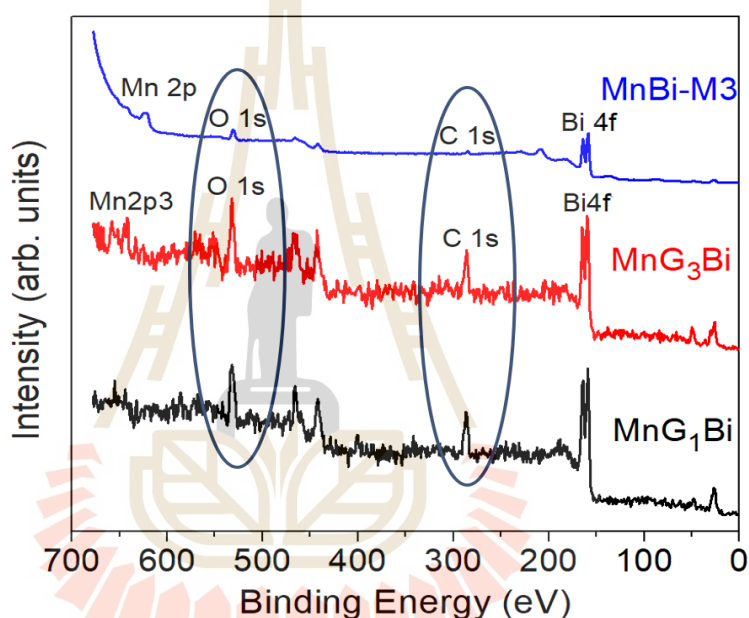


Figure 4.23 The XRD pattern of the MnBi\_M3,  $MnG_1Bi$  and  $MnG_3Bi$ .

From the XRD pattern of MnBi prepared with conventional ball milling and glycine addition. It was found that the peaks intensities in the two synthesized differed greatly by found that in grinding in glycine. It has a very high Bi (JCPDS Card. No. 01-085-1329) constituents and, conversely, has a very small proportion of MnBi

concentrations (<5%), in contrast to conventional grinding which yields a high MnBi (JCPDS Card. No. 96-900-8900) concentration ratio of about 70%, as show in figure 4.23. This section can explain why glycine is added to the manganese grinding process. May be interfere with the interactions between bismuth liquid and manganese granules to form MnBi material layer, which can be explained by disruption of diffusion during liquid phase sintering, which may be caused by hydrocarbons (i.e.,  $\text{NH}_2\text{-CH}_2\text{-COOH}$ ) which are the main constituents in glycine. This can be examined with x-ray photoemission (XPS) techniques, which will be discussed in the next section.



**Figure 4.24** XPS spectra of the MnBi\_M3, MnG<sub>1</sub>Bi, and MnG<sub>3</sub>Bi.

The wide scan XPS including Mn 2p, O 1s, C 1s and Bi 4f have been performed in figure 4.24. The main difference between MnBi\_M3 and MnG<sub>x</sub>Bi is the intensity of O 1s B.E. (532 eV) and C 1s (B.E. 288.3 eV). The MnBi obtained by grinding in glycine has a significantly high proportion of O and C. This can be explained by the presence of hydrocarbon elements such as  $\text{NH}_2\text{-CH}_2\text{-COOH}$  as the principal constituents in glycine. This is an advantage of surface sensitive XPS technique which clearly verify the presence of surface contaminations. The results of all above-mentioned experiments could imply that Mn grinding in glycine results in a significant reduction of magnetic

efficiency caused by the inhibition of MnBi layer formation due to the surface coverage of hydrocarbon elements.

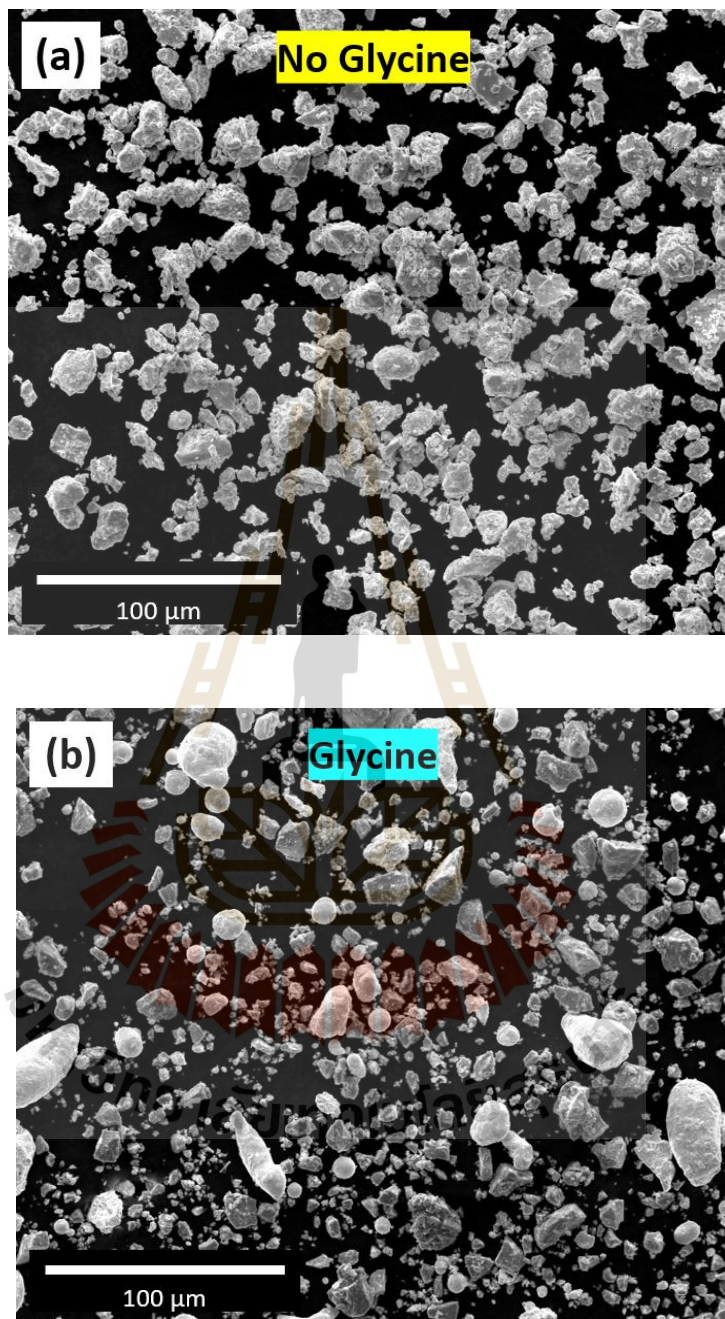


**Figure 4.25** The SEM images of the (a) MnBi\_M3 and (b) MnG<sub>3</sub>Bi.

Figure 4.25. shows the morphological comparison between the conventional ball-milled Mn powder and the glycine-added powders. According to the SEM image of the conventional-milled MnBi shown in figure 4.25(a), the particles are fairly uniformly distributed in terms of particle size and elemental composition

throughout the region. For the glycine-added particles, it was found that the appearance characteristics are rather different from the conventional ball-milled sample. In other words, the particles are distributed unevenly. There are both small and large particles, as well as having a clear difference in composition (determined from color contrast). It was found that the large-white spheres were Bi, while the small particle was Mn with some adhered Bi. Two types of particles tend to separate with each other. From this result, it can be concluded that glycine addition is likely to inhibit the Mn and Bi interactions, consistent with previous XRD results.

The magnetic performance of the MnBi prepared by glycine addition during ball milling is decreased dramatically compared to the conventional ball-milled samples. This result could be caused by the incomplete process described by the presence of unreacted Bi and the absence of the MnBi phase. The MnBi formation interruption could be described by the coverage of hydrocarbons on the surface. The proper hydrocarbon removal process is required prior to the sintering process to obtain high magnetic performance.

#### 4.7 LTP-MnBi and Co composite

If the use of LTP-MnBi in permanent magnet production is not particularly appealing due to its relatively low maximum energy product. Although, the coercivity value increases with temperature, the saturation magnetization value is also trending to decrease. There is also a problem with the degradation of magnetic materials. Hence, the development of permanent magnetic materials to improve the efficiency of future applications may require the use of LTP-MnBi magnetic as the main component. The research in this section has the concept of the composite between LTP-MnBi (hard magnetic materials) and cobalt (soft magnetic materials). However, the doping of the third element stresses the crystal structure and changes the LTP-MnBi ratio, resulting in a magnetic interaction between the Mn atoms in the crystal structure and the Mn atoms inserted within the crystal structure (interstitial Mn), leading to a decrease in magnetization. Meanwhile, the thermal stability is improved. Cobalt is one of the soft magnetic materials used in this section. The study and preparation of the

composite were divided into three stages of preparation. Starting with grinding Mn for 3, 7, and 11 hours, it was then mixed with Bi powder and synthesized using a vacuum sintering technique at 275 °C for 12 hours. that, LTP-MnBi powder composite with cobalt in an atomic ratio of 1:1 %at and using a planetary micro mill at 300 rpm for 30 minutes. The VSM measurement shown in figure 4.26 compares the hysteresis loop of specimens and finds that the coercivity value is equal to 1.82, 1.63, and 1.53 kOe, the saturated magnetization value is equal to 78.93, 76.61, and 76.09 emu/g and the maximum energy product is equal to 0.81, 0.63, and 0.58 MGOe for LTP-MnBi magnetic materials via varied Mn ball milling 3, 7, and 11 hours sintering in vacuum at 275 °C for 12 hours composite with Cobalt shown in figure. 4.26 respectively. It can be clearly seen that the exchange slightly.

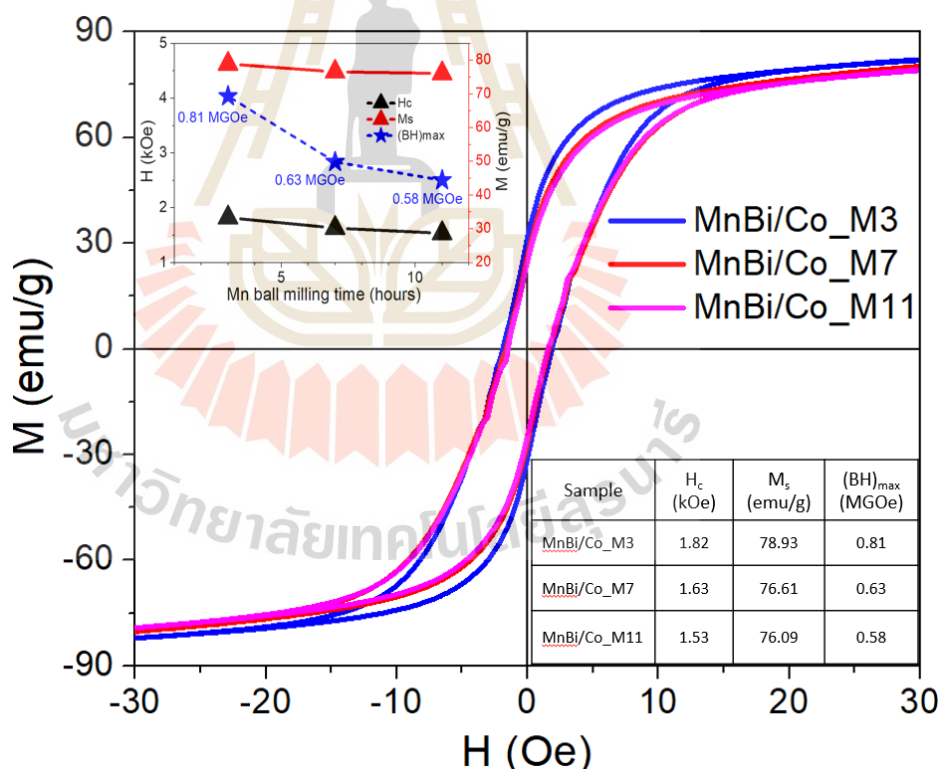
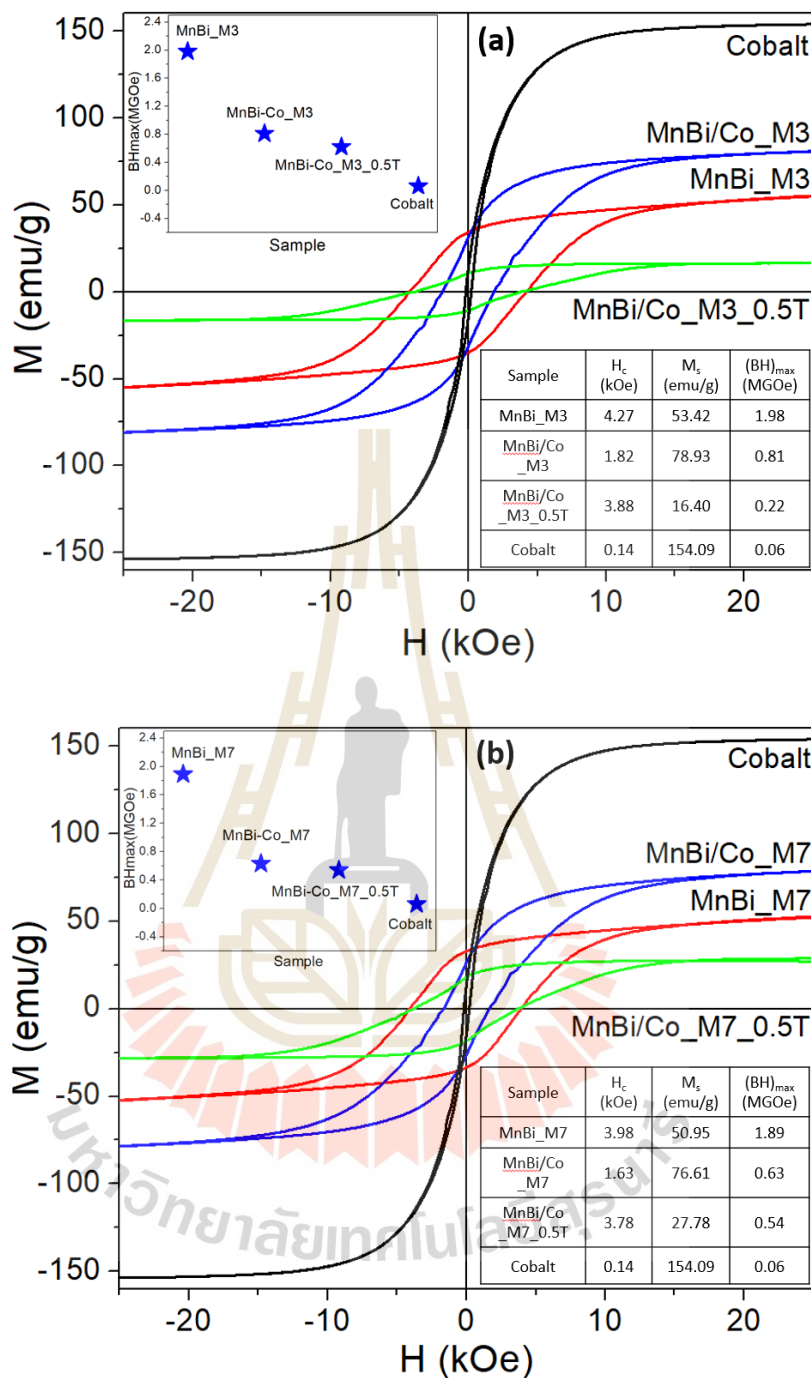
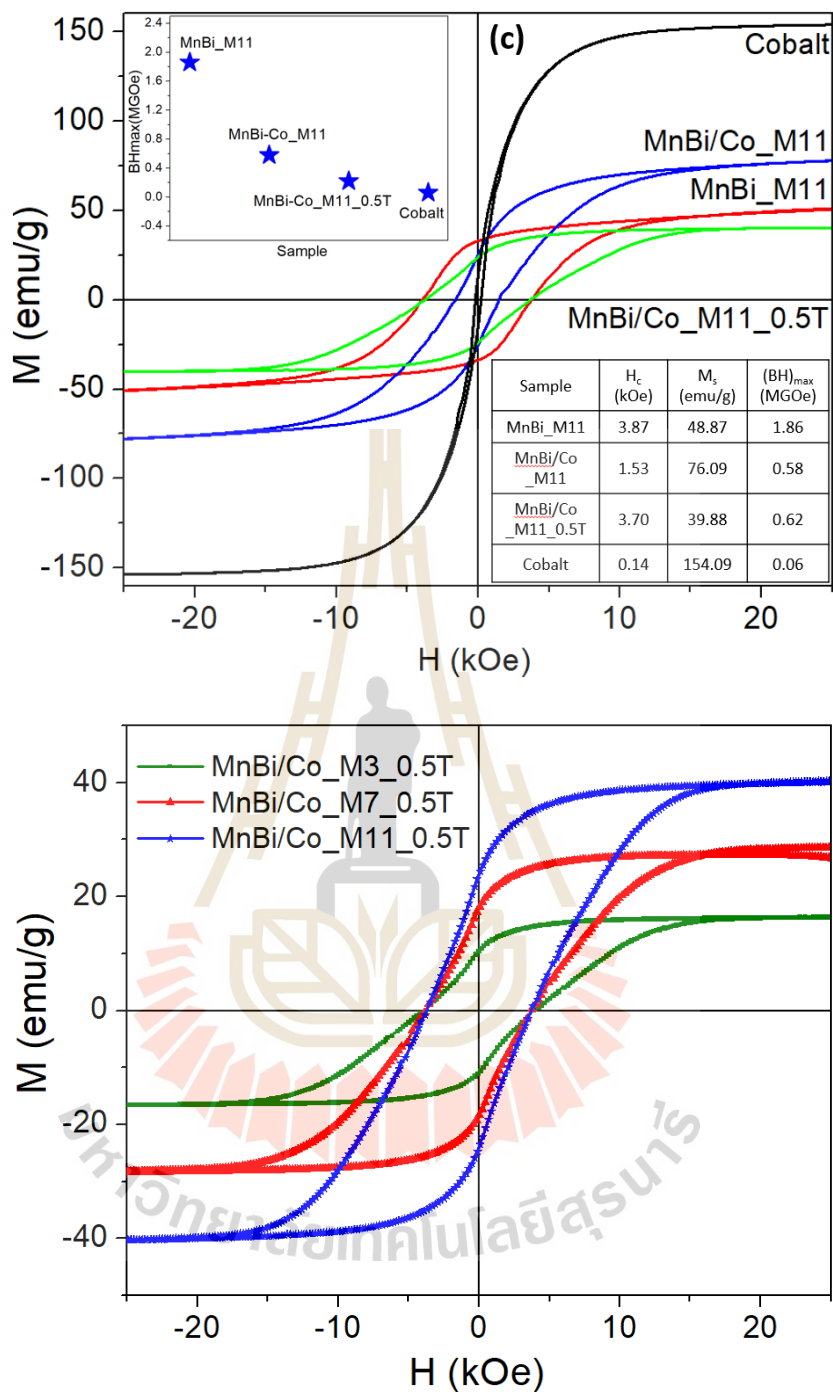


Figure 4.26 shows the M-H curves of the sintered samples prepared using Mn powder particle from ball milling for 3, 7, and 11 hours.

To exhibit the higher maximum energy product ( $BH_{max}$ ) of the MnBi powder. To consider the exchange-coupled interaction of hard and soft phases. The soft phase of cobalt has a larger saturation magnetization and quite a few coercivity. The exchange coupling effect of this with LTP-MnBi has a low saturation magnetization and a high coercivity value, which the MnBi/Co composite demonstrates higher saturation magnetization when compared with the LTP-MnBi phase. It was discovered that when the MnBi/Co sample was magnetically aligned under a magnetic field of 0.5 T, it exhibited low saturation magnetization but the coercivity increased up to two times when compared with LTP-MnBi. Starting from MnBi powder, MnBi/Co composite, and MnBi/Co alignment, the energy product ( $BH$ )<sub>max</sub> of these samples tends to decrease, as shown in figure 4.27(a-c). The effect of magnetically aligned Manganese Bismuth composite with Cobalt. The saturated magnetization is 16.40, 27.78, and 39.88 emu/g, respectively, and the maximum energy product is 0.22, 0.54, and 0.62 MGOe for the LTP-MnBi sample that uses manganese powder from the grinding high speed at 300 rpm for 3-, 7-, and 11-hours composite with Cobalt under a magnetic field of 0.5 T, as shown in figure 4.27(d).



**Figure 4.27** (a) M-H curves after sintering in vacuum of MnBi-M3, MnBi/Co-M3, MnBi/Co-M3-0.5T and Cobalt. The inset of (a) shows the  $(BH)_{max}$  of samples (upper left). (b) M-H curves after sintering in vacuum of MnBi-M7, MnBi/Co-M7, MnBi/Co-M7-0.5T and Cobalt. The inset of (a) shows the  $(BH)_{max}$  of samples (upper left).



**Figure 4.27** (Continued) (c) M-H curves after sintering in vacuum of MnBi-M11, MnBi/Co-M11, MnBi/Co-M11-0.5T, and Cobalt. The inset of (a) shows the  $(BH)_{max}$  of samples (upper left). (d) M-H curves after sintering in a vacuum and alignment the direction particles with the magnetic field of 0.5 T.

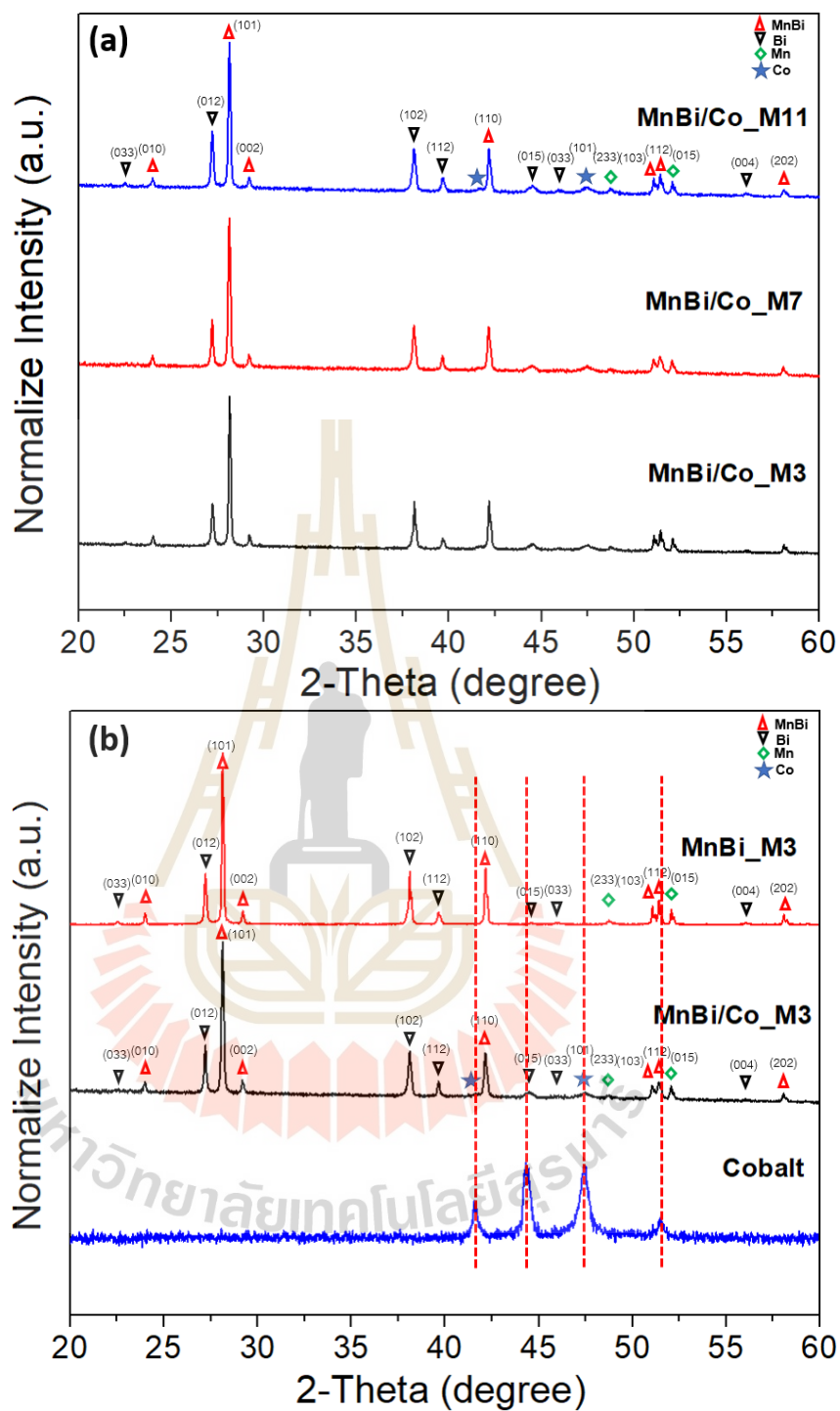
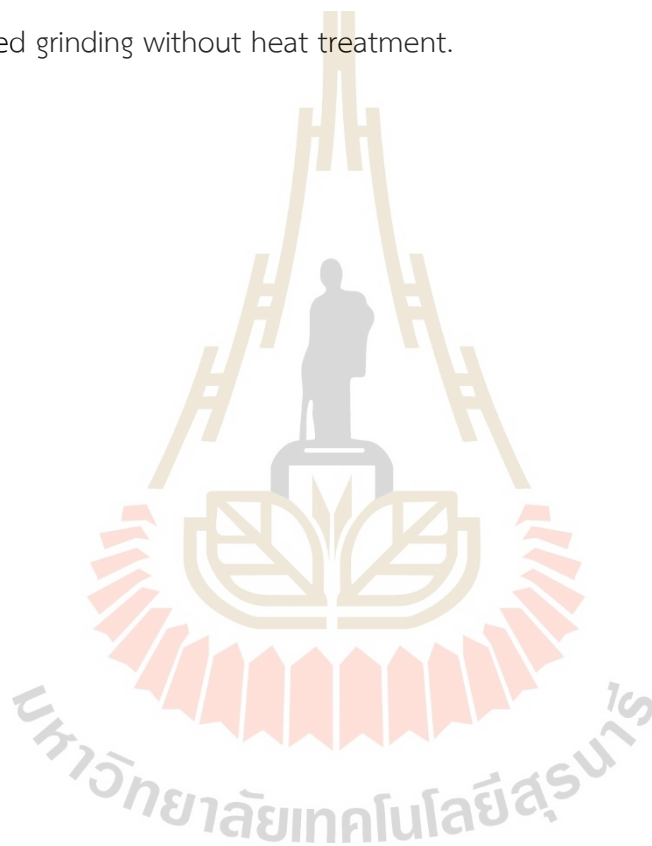


Figure 4.28 XRD patterns of (a) MnBi/Co-M3, MnBi/Co-M7, and MnBi/Co-M11 and (b) MnBi-M3, MnBi/Co-M3 compared with Cobalt.

Figure 4.28(a) is the result of XRD measurements of all three samples. It indicates that the primary constituent after vacuum sintering was LTP-MnBi and Bi where Mn element was found to be low intensity due to Mn being surrounded by LTP-MnBi and Bi. In which, there is a layer too thick that all X-ray radiation can pass through. Figure 4.28(b) is an example of XRD measurements of LTP-MnBi and LTP-MnBi/Co samples using Mn powder from grinding for 3 hours compared with Cobalt from a bottle. It clearly shows and supports the composite M-H curves that exchange coupling from combined grinding without heat treatment.



## CHAPTER V

### CONCLUSIONS AND REMARKS

This thesis work focused on the development of vacuum sintering techniques and the synthesis of LTP-MnBi magnetic materials as an alternative to producing rare-earth-free permanent magnetic materials. The synthesis methods were studied and optimized with various parameters and conditions, such as the effect of gravity during sintering, particle size, vacuum pressure, Mn grinding time, glycine addition, and hybridization with cobalt. XRD, SEM/EDS, and XPS techniques were used to investigate the phases, microstructure, morphology, and chemical composition. The VSM technique was employed to investigate the magnetic properties.

A simple vacuum sintering system was built and utilized throughout this thesis work. The system provided opportunity to synthesize MnBi magnetic materials sintering without the formation of oxides. The sintered materials are made up of three different materials i.e., LTP-MnBi, Bi and Mn. The MnBi content for short sintering times was still low, resulting in the low energy product which is approximately ten times lower than predicted theoretically. Longer sintering time or using smaller Mn particle size was expected to yield higher MnBi content, and consequently the higher energy product. However, the technique was demonstrated to be a facile technique for synthesizing LTP-MnBi with less energy and time consuming as compared to other techniques.

It was demonstrated that vacuum pressure must be low enough to prevent oxidation. Preparations of MnBi in ultra-high vacuum ( $10^{-7}$  mbar), low vacuum ( $10^{-2}$  mbar), and under Ar flow were experimented. It was found that vacuum pressure is critical in the formation of MnBi during liquid phase sintering (LPS). The AP-MnBi ingot resulted in the inhomogeneous sintered product after sintering, with separated layers of Bi and MnBi, whereas the UHV-MnBi ingot produced a rather homogeneous material. Oxides were formed in the cases of LV-MnBi and AP-MnBi than in UHV-MnBi.

One of the main goals of this thesis work is to increase the MnBi content by using the initial Mn with powder particles as small as possible in order for the whole Mn particles could be transformed to MnBi. It is well known that the magnetic properties of MnBi magnetic materials depend on many factors. One of those factors is particle size. In addition, there is an advantage that smaller the powder particle size, the higher coercivity. In this work, ball milling was used to reduce the size of the initial Mn powder particles. The particle size of Mn powder decreases as the ball milling time increases. However, Mn oxides were formed during milling. The amount of oxide increases with milling time, indicating an increase in MnO content on the surface of Mn particles, which inhibits MnBi formation during sintering. The formation of oxide should play a significant role in the reduction of MnBi content. It should be noted that oxides should be removed in order to improve the magnetic properties of MnBi.

To avoid the formation of oxides during ball milling of Mn, glycine was added. The addition of glycine is expected also to prevent particle agglomeration, resulting in small, non-gathered Mn particles. Small powder particles of Mn were obtained after prolonged ball milling. This small Mn powder was used in the sintering. However, the magnetic properties of MnBi prepared from the glycine-added Mn were not as good as expected. It was found that small amount of MnBi was formed, suggesting that less chemical reaction between Bi and Mn occurred during sintering. This was explained by the fact that the surfaces of the ball-milled Mn were coated by hydrocarbons, the product of glycine during ball milling. This coating layers prevent the formation of the MnBi.

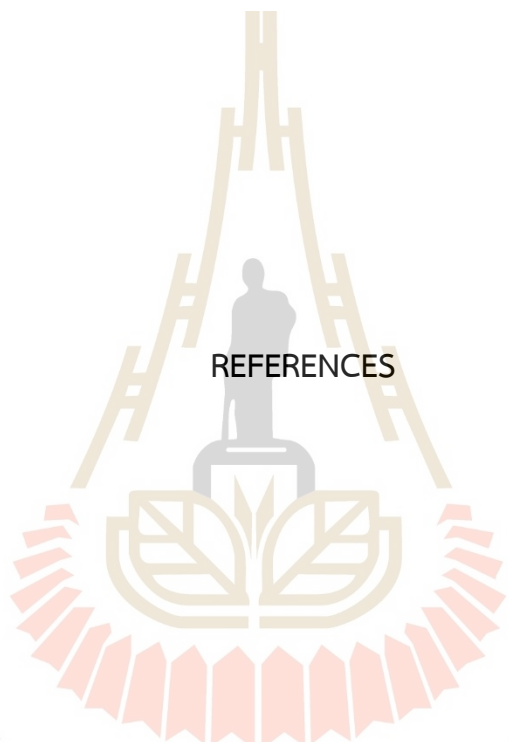
The exchange coupling effect has a low saturation magnetization and a high coercivity value, whereas the MnBi/Co composite has a higher saturation magnetization when compared to the LTP-MnBi phase. When the MnBi/Co sample was magnetically aligned in a 0.5 T magnetic field, it showed low saturation magnetization but increased coercivity by up to two times when compared to LTP-MnBi. The energy product (BH)<sub>max</sub> of these samples tends to decrease as they progress from MnBi powder to MnBi/Co composite to MnBi/Co alignment.

Great efforts are still needed for further development of rare-earth free magnetic materials. LTP-MnBi is one of the promising materials, and the preparation

technique used in this thesis work is also a promising technique for mass production. The stringent condition to be overcome is to increase LTP-MnBi content in the sintered product. The approach that has been attempted was to use the Mn powder with particle size as small as possible. In principle, it shall be in the range of a few microns. These sizes of powder particles not out of reach by today technology if more investment is available.

For research and development at a laboratory scale, further work may be carried out by using a low-energy ball milling machine to prevent the formation of oxides on the milled particles. However, if a low-energy ball milling machine is not available, a reduction process after normal ball milling might be required to remove the oxides. With small powder particle sizes, high content LTP-MnBi may be obtained by low-temperature liquid-phase sintering in vacuum, as employed in this work. High performance LTP-MnBi may even enhance if magnetic separation will be carried out. After successful demonstrations, mass production may require a large production Mn using a technique like atomizer to produce small powder particles of Mn for the sintering.

Finally, if LTP-MnBi will be used as a hard phase material for composited materials for high performance magnet, investigations of magnetic composites are of great importance for further research.



REFERENCES

มหาวิทยาลัยเทคโนโลยีสุรนารี

## REFERENCES

- Abdelbasir, S. and Shalan, A. E. (2019). Intriguing properties and applications of functional magnetic materials. *Functional Materials*.
- Adams, E., Hubbard, W. M., and Syeles, A. M. (1952). A new permanent magnet from powdered manganese bismuthide. *Journal of Applied Physics*, 23(11), 1207-1211.
- Aharoni, A. (1998). Demagnetizing factors for rectangular ferromagnetic prisms. *Journal of applied physics*, 83(6), 3432-3434.
- Akhtar, K., Khan, S. A., Khan, S. B., and Asiri, A. M. (2018). Scanning electron microscopy: Principle and applications in nanomaterials characterization. *Handbook of materials characterization*, Springer, Cham.
- Antonov, V. N. and Antropov, V. P. (2020). Low-temperature MnBi alloys: Electronic and magnetic properties, constitution, morphology, and fabrication. *Low Temperature Physics*, 46(1), 1-27.
- Bandaru, P. R., Sands, T. D., Kubota, Y., and Marinero, E. E. (1998). Decoupling the structural and magnetic phase transformations in magneto optic MnBi thin films by the partial substitution of Cr for Mn. *Applied physics letters*, 72(18), 2337-2339.
- Borsup, J., Eknapakul, T., Myint, H. T., Smith, M. F., Yordsri, V., Pinitsoontorn, S., and Songsiriritthigul, P. (2022). Formation and magnetic properties of low-temperature phase manganese bismuth prepared by low-temperature liquid phase sintering in vacuum. *Journal of Magnetism and Magnetic Materials*, 544, 168661.
- Burgei, W., Pechan, M. J., and Jaeger, H. (2003). A simple vibrating sample magnetometer for use in a materials physics course. *American Journal of Physics*, 71(8), 825-828.

- Cao, J., Huang, Y. L., Hou, Y. H., Zhang, G. Q., Shi, Z. Q., Zhong, Z. C., and Liu, Z. W. (2018). Effects of intergranular phase on the coercivity for MnBi magnets prepared by spark plasma sintering. *AIP Advances*, 8(5), 055132.
- Cao, S., Yue, M., Yang, Y. X., Zhang, D. T., Liu, W. Q., Zhang, J. X., Guo, Z.H., and Li, W. (2011). Magnetic properties and thermal stability of MnBi/NdFeB hybrid bonded magnets. *Journal of Applied Physics*, 109(7), 07A740.
- Charoensuk, T. and Sirisathitkul, C. (2018). Effects of heat treatment and composition on ball milled MnBi and MnBi/Co magnets. *Digest Journal of Nanomaterials and Biostructures*, 13, 609-614.
- Chen, D. X., Brug, J. A., and Goldfarb, R. B. (1991). Demagnetizing factors for cylinders. *IEEE Transactions on magnetics*, 27(4), 3601-3619.
- Chen, T. (1974). Contribution to the equilibrium phase diagram of the Mn–Bi system near MnBi. *Journal of Applied Physics*, 45(5), 2358-2360.
- Chen, T. and Stutius, W. (1974). The phase transformation and physical properties of the MnBi and Mn 1.08 Bi compounds. *IEEE Transactions on Magnetism*, 10(3), 581-586.
- Chen, Y. C., Sawatzki, S., Ener, S., Sepehri-Amin, H., Leineweber, A., Gregori, G., and Goering, E. (2016). On the synthesis and microstructure analysis of high performance MnBi. *AIP Advances*, 6(12), 125301.
- Christopher, N. R., Singh, N., Singh, S. K., Gahtori, B., Mishra, S. K., Dhar, A., and Awana, V. P. S. (2013). Appreciable magnetic moment and energy density in single-step normal route synthesized MnBi. *Journal of superconductivity and novel magnetism*, 26(11), 3161-3165.
- Coey, J. M. D. (2011). Hard magnetic materials: A perspective. *IEEE Transactions on magnetics*, 47(12), 4671-4681.
- Corbin, S. F. and Mclsaac, D. J. (2003). Differential scanning calorimetry of the stages of transient liquid phase sintering. *Materials Science and Engineering: A*, 346(1-2), 132-140.

- Cui, J., Choi, J. P., Li, G., Polikarpov, E., Darsell, J., Kramer, M. J., Zarkevich, N.A., Wang, L.L., Overman, N., Johnson, D.D., Marinescu, M., Huang, Q.Z., Wu, H., Vuong, N.V and Liu, J. P. (2014). Development of MnBi permanent magnet: Neutron diffraction of MnBi powder. *Journal of Applied Physics*, 115(17), 17A743.
- Cui, J., Choi, J. P., Li, G., Polikarpov, E., Darsell, J., Overman, N., Olszta, M., Schreiber, D., Bowden, M., Droubay, T., Kramer, M. J., Zarkevich, N. A., Wang, L. L., Johnson, D. D., Marinescu, M., Takeuchi, I., Huang, Q. Z., Wu, H., Reeve, H., Vuong, N. V., and Liu, J. P. (2014). Thermal stability of MnBi magnetic materials. *Journal of Physics: Condensed Matter*, 26(6), 064212.
- Cui, J., Choi, J. P., Polikarpov, E., Bowden, M. E., Xie, W., Li, G., Nei, Z., Zarkevich, N., Kramer, M. J., and Johnson, D. (2014). Effect of composition and heat treatment on MnBi magnetic materials. *Acta Materialia*, 79, 374-381.
- Cui, J., Kramer, M., Zhou, L., Liu, F., Gabay, A., Hadjipanayis, G., Balasubramanian, B., and Sellmyer, D. (2018). Current progress and future challenges in rare-earth-free permanent magnets. *Acta Materialia*, 158, 118-137.
- Dutta, T., Kim, K. H., Uchimiya, M., Kwon, E. E., Jeon, B. H., Deep, A., and Yun, S. T. (2016). Global demand for rare earth resources and strategies for green mining. *Environmental Research*, 150, 182-190.
- Fiorillo, F. (2010). Measurements of magnetic materials. *Metrologia*, 47(2), S114.
- Foner, S. (1959). Versatile and sensitive vibrating-sample magnetometer. *Review of Scientific Instruments*, 30(7), 548-557.
- German, R. M., Suri, P., and Park, S. J. (2009). Liquid phase sintering. *Journal of materials science*, 44(1), 1-39.
- Griffiths, D. J. (2005). Introduction to electrodynamics.
- Guo, X., Chen, X., Altounian, Z., and Ström-Olsen, J. O. (1992). Magnetic properties of MnBi prepared by rapid solidification. *Physical Review B*, 46(22), 14578.
- Guo, X., Zaluska, A., Altounian, Z., and Ström-Olsen, J. O. (1990). The formation of single-phase equiatomic MnBi by rapid solidification. *Journal of Materials Research*, 5(11), 2646-2651.

- Gutfleisch, O., Willard, M. A., Brück, E., Chen, C. H., Sankar, S. G., and Liu, J. P. (2011). Magnetic materials and devices for the 21<sup>st</sup> century: stronger, lighter, and more energy efficient. *Advanced materials*, 23(7), 821-842
- Huang, K. W., Chieh, J. J., Shi, J. C., and Chiang, M. H. (2015). Assaying carcinoembryonic antigens by normalized saturation magnetization. *Nanoscale Research Letters*, 10(1), 1-7.
- Huang, Y. L., Shi, Z. Q., Hou, Y. H., and Cao, J. (2019). Microstructure, improved magnetic properties, and recoil loops characteristics for MnBi alloys. *Journal of Magnetism and Magnetic Materials*, 485, 157-164.
- Jensen, B. A., Tang, W., Liu, X., Nolte, A. I., Ouyang, G., Dennis, K. W., and Cui, J. (2019). Optimizing composition in MnBi permanent magnet alloys. *Acta Materialia*, 181, 595-602.
- Jha, R., Dulikravich, G. S., Colaço, M. J., Fan, M., Schwartz, J., and Koch, C. C. (2017). Magnetic alloys design using multi-objective optimization. *Properties and Characterization of Modern Materials*, 261-284.
- Joseph, R. I., and Schlömann, E. (1965). Demagnetizing field in nonellipsoidal bodies. *Journal of Applied Physics*, 36(5), 1579-1593.
- Kang, S. J. L. (2004). *Sintering: densification, grain growth and microstructure*. Elsevier.
- Kharel, P., Shah, V. R., Skomski, R., Shield, J. E., and Sellmyer, D. J. (2013). Magnetism of MnBi-based nanomaterials. *IEEE transactions on magnetics*, 49(7), 3318-3321.
- Kim, S., Moon, H., Jung, H., Kim, S. M., Lee, H. S., Choi-Yim, H., and Lee, W. (2017). Magnetic properties of large-scaled MnBi bulk magnets. *Journal of Alloys and Compounds*, 708, 1245-1249.
- Kirkeminde, A., Shen, J., Gong, M., Cui, J., and Ren, S. (2015). Metal-redox synthesis of MnBi hard magnetic nanoparticles. *Chemistry of Materials*, 27(13), 4677-4681.
- Kot, M. (2014). *In-operando hard X-ray photoelectron spectroscopy study on the resistive switching physics of HfO<sub>2</sub>-based RRAM (Doctoral dissertation)*.

- Kramer, M. J., McCallum, R. W., Anderson, I. A., and Constantinides, S. (2012). Prospects for non-rare earth permanent magnets for traction motors and generators. *Jom*, 64(7), 752-763.
- Kronmüller, H., Yang, J. B., and Goll, D. (2014). Micromagnetic analysis of the hardening mechanisms of nanocrystalline MnBi and nanopatterned FePt intermetallic compounds. *Journal of Physics: Condensed Matter*, 26(6), 064210.
- Li, B., Ma, Y., Shao, B., Li, C., Chen, D., Sun, J., Zheng, Q., and Yin, X. (2018). Preparation and magnetic properties of anisotropic MnBi powders. *Physica B: Condensed Matter*, 530, 322-326.
- Li, C., Guo, D., Shao, B., Li, K., Li, B., and Chen, D. (2018). Effect of heat treatment and ball milling on MnBi magnetic materials. *Materials Research Express*, 5(1), 016104.
- Li, N., Cui, C., Liu, S., Liu, S., Cui, S., and Wang, Q. (2017). Microstructure and mechanical properties of Ti<sub>6</sub>Al<sub>4</sub>V alloy modified and reinforced by in situ Ti<sub>5</sub>Si<sub>3</sub>/Ti composite ribbon inoculants. *Metals*, 7(7), 267.
- Liu, S., Wang, J., and Dong, F. (2018). A new bottom-up synthesis of MnBi particles with high magnetic performance. *Chemical Physics Letters*, 691, 325-329.
- Lopez, L. F., Beaman, J. J., and Williamson, R. L. (2012, October). Linear-Quadratic-Gaussian (LQG) controller for liquid pool profile in vacuum arc remelting. *Dynamic Systems and Control Conference, American Society of Mechanical Engineers*, 45301, 677-686.
- Lopez-Dominguez, V., Quesada, A., Guzmán-Mínguez, J. C., Moreno, L., Lere, M., Spottorno, J., Giacomne, F., Fernandez, F.J., Hernando, A., and García, M. A. (2018). A simple vibrating sample magnetometer for macroscopic samples. *Review of Scientific Instruments*, 89(3), 034707.
- Ma, Y. L., Liu, X. B., Nguyen, V. V., Poudyal, N., Yue, M., and Liu, J. P. (2016). Preparation and magnetic properties of anisotropic bulk MnBi/NdFeB hybrid magnets. *Journal of Magnetism and Magnetic Materials*, 411, 116-119.

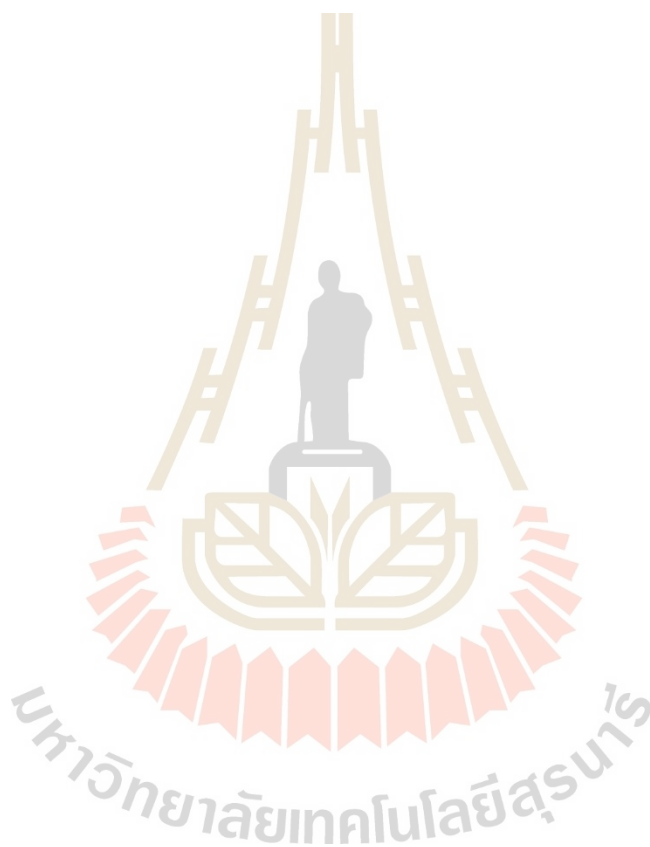
- Martone, A. M. (2017). *Development of Iron-Rich (Fe<sub>1-x-y</sub>Ni<sub>x</sub>Co<sub>y</sub>) 88Zr7B4Cu1 Nanocrystalline Magnetic Materials to Minimize Magnetostriction for High Current Inductor Cores* (Doctoral dissertation, Case Western Reserve University).
- Mitsui, Y., Koyama, K., and Watanabe, K. (2013). Bi–Mn binary phase diagram in high magnetic fields. *Materials transactions*, 54(2), 242-245.
- Mitsui, Y., Umetsu, R. Y., Takahashi, K., and Koyama, K. (2018). Reactive sintering process of ferromagnetic MnBi under high magnetic fields. *Journal of Magnetism and Magnetic Materials*, 453, 231-235.
- Mohapatra, J. and Liu, J. P. (2018). Rare-Earth-free permanent magnets: the past and future. *Handbook of magnetic materials*, 27, 1-57.
- Nakagawa, Y. and Kato, H. (1994). Magnetic hysteresis and demagnetizing-field correction for rare earth magnet materials. *IEEE Translation Journal on Magnetics in Japan*, 9(6), 177-184.
- Ngamsomrit, S., Saisopa, T., Borsup, J., Tun, M. S., Myint, H. T., Nakajima, H., Songsiriritthigul, C., Pinitsoontorn, S., and Songsiriritthigul, P. (2021). Preparation of low-temperature phase MnBi by sintering in vacuum. *Journal of Physics: Conference Series*, 1719(1), 012057.
- Nguyen, T. X., Vuong, O. K. T., Nguyen, H. T., and Nguyen, V. V. (2017). Preparation and magnetic properties of MnBi/Co nanocomposite magnets. *Journal of Electronic Materials*, 46(6), 3359-3366.
- Nguyen, V. V., Poudyal, N., Liu, X., Liu, J. P., Sun, K., Kramer, M. J., and Cui, J. (2014). High-performance MnBi alloy prepared using profiled heat treatment. *IEEE Transactions on magnetics*, 50(110266).
- Oikawa, K., Mitsui, Y., Koyama, K., and Anzai, K. (2011). Thermodynamic assessment of the Bi-Mn system. *Materials Transactions*, 1110031481-1110031481.
- Okamoto, H. and Massalski, T. B. (1990). Binary alloy phase diagrams. *ASM International, Materials Park, OH, USA*, 12.
- Pardo, E., Chen, D. X., and Sanchez, A. (2004). Demagnetizing factors for completely shielded rectangular prisms. *Journal of applied physics*, 96(9), 5365-5369.

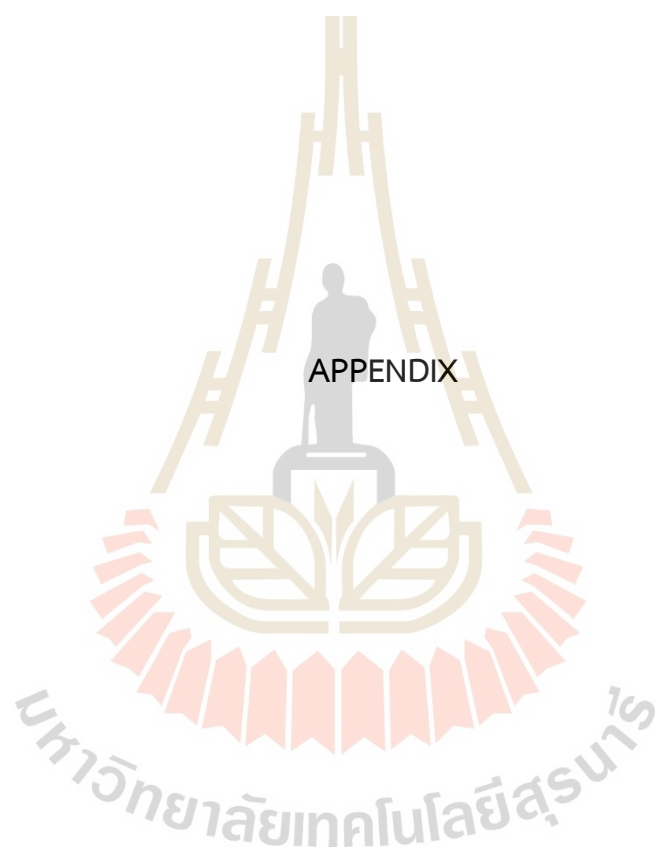
- Park, J., Hong, Y. K., Lee, J., Lee, W., Kim, S. G., and Choi, C. J. (2014). Electronic structure and maximum energy product of MnBi. *Metals*, 4(3), 455-464.
- Patel, K., Zhang, J., and Ren, S. (2018). Rare-earth-free high energy product manganese-based magnetic materials. *Nanoscale*, 10(25), 11701-11718.
- Pattnaik, D. P. (2014). *Design and fabrication of vibrating sample magnetometer (Doctoral dissertation)*.
- Piedra Marin, L. E. (2020). *Construction of an electromagnet for the development of a vibrating sample magnetometer* (Bachelor's thesis, Universidad de Investigación de Tecnología Experimental Yachay).
- Poudyal, N. and Liu, J. P. (2012). Advances in nanostructured permanent magnets research. *Journal of Physics D: Applied Physics*, 46(4), 043001.
- Poudyal, N., Liu, X., Wang, W., Nguyen, V. V., Ma, Y., Gandha, K., Lui, J.P., Sun, K., Kramer, M.J., and Cui, J. (2016). Processing of MnBi bulk magnets with enhanced energy product. *AIP Advances*, 6(5), 056004.
- Prozorov, R., and Kogan, V. G. (2018). Effective demagnetizing factors of diamagnetic samples of various shapes. *Physical review applied*, 10(1), 014030.
- Qiu, Z. (2019). Transition Metal-Based Electrocatalysts for Alkaline Water Splitting and CO<sub>2</sub> Reduction, *Doctoral dissertation, Acta Universitatis Upsaliensis*.
- Rafique, M. (2015). Study of the Magnetoelectric Properties of Multiferroic Thin Films and Composites for Device Applications, *Doctoral dissertation, COMSATS Institute of Information Technology Lahore Campus-Pakistan*.
- Ramakrishna, V. V., Kavita, S., Gautam, R., Ramesh, T., and Gopalan, R. (2018). Investigation of structural and magnetic properties of Al and Cu doped MnBi alloy. *Journal of Magnetism and Magnetic Materials*, 458, 23-29.
- Rao, N. R. and Hadjipanayis, G. C. (2015). Influence of jet milling process parameters on particle size, phase formation and magnetic properties of MnBi alloy. *Journal of Alloys and Compounds*, 629, 80-83.
- Sabet, S., Moradabadi, A., Gorji, S., Yi, M., Gong, Q., Fawey, M. H., Hildebrandt, E., Wang, D., Zhang, H., Xu, B.X., Kiibel, C., and Alff, L. (2018). On the origin of incoherent

- magnetic exchange coupling in MnBi/Fe<sub>x</sub>Co<sub>1-x</sub> bilayer system. *arXiv preprint arXiv:1804.05383*.
- Saha, S., Huang, M. Q., Thong, C. J., Zande, B. J., Chandhok, V. K., Simizu, S., and Sankar, S. G. (2000). Magnetic properties of MnBi<sub>1-x</sub>R<sub>x</sub> (R= rare earth) systems. *Journal of Applied Physics*, 87(9), 6040-6042.
- Sannasi, V. and Subbian, K. (2020). Influence of Moringa oleifera gum on two polymorphs synthesis of MnO<sub>2</sub> and evaluation of the pseudo-capacitance activity. *Journal of Materials Science: Materials in Electronics*, 31(19), 17120-17132.
- Shah, S. A. H. (2013). Vibrating Sample Magnetometry: Analysis and Construction. *Syed Babar Ali School of Science and Engineering, LUMS*.
- Shirzadi, A. A., Koziel, T., Cios, G., and Bała, P. (2019). Development of Auto Ejection Melt Spinning (AEMS) and its application in fabrication of cobalt-based ribbons. *Journal of Materials Processing Technology*, 264, 377-381.
- Smith, D. O. (1956). Development of a vibrating-coil magnetometer. *Review of Scientific Instruments*, 27(5), 261-268.
- Spaldin, N. A. (2010). *Magnetic materials: fundamentals and applications*. Cambridge university press.
- Sun, J., Li, C., Huang, Q., Liu, G., Han, G., Yu, S., and Kang, S. (2016). A facile way to synthesize rare-earth-free MnBi magnetic nanoparticles. *RSC advances*, 6(102), 100035-100039.
- Truong, N. X. and Vuong, N. V. (2015). Preparation and magnetic properties of MnBi alloy and its hybridization with NdFeB. *Journal of Magnetism*, 20(4), 336-341.
- Voncken, J. H. L. (2016). The rare earth elements-a special group of metals. *The Rare Earth Elements, Springer, Cham*, 1-13.
- Xie, W., Polikarpov, E., Choi, J. P., Bowden, M. E., Sun, K., and Cui, J. (2016). Effect of ball milling and heat treatment process on MnBi powders magnetic properties. *Journal of Alloys and Compounds*, 680, 1-5.

- Yang, J. B., Kamaraju, K., Yelon, W. B., James, W. J., Cai, Q., and Bollero, A. (2001). Magnetic properties of the MnBi intermetallic compound. *Applied Physics Letters*, 79(12), 1846-1848.
- Yang, J. B., Yang, Y. B., Chen, X. G., Ma, X. B., Han, J. Z., Yang, Y. C., Guo, S., Yan, A.R., Huang, Q.Z., Wu, M.M., and Chen, D. F. (2011). Anisotropic nanocrystalline MnBi with high coercivity at high temperature. *Applied Physics Letters*, 99(8), 082505.
- Yang, J. B., Yelon, W. B., James, W. J., Cai, Q., Kornecki, M., Roy, S., Ali, N., and l'Heritier, P. (2002). Crystal structure, magnetic properties and electronic structure of the MnBi intermetallic compound. *Journal of Physics: Condensed Matter*, 14(25), 6509.
- Yang, J. B., Yelon, W. B., James, W. J., Cai, Q., Roy, S., and Ali, N. (2002). Structure and magnetic properties of the MnBi low temperature phase. *Journal of applied physics*, 91(10), 7866-7868.
- Yang, J., Yang, W., Shao, Z., Liang, D., Zhao, H., Xia, Y., and Yang, Y. (2018). Mn-based permanent magnets. *Chinese Physics B*, 27(11), 117503.
- Yang, Y. B., Chen, X. G., Guo, S., Yan, A. R., Huang, Q. Z., Wu, M. M., Chen, D.F., Yang, Y.C., and Yang, J. B. (2013). Temperature dependences of structure and coercivity for melt spun MnBi compound. *Journal of magnetism and Magnetic Materials*, 330, 106-110.
- Yoshida, H., Shima, T., Takahashi, T., and Fujimori, H. (1999). Preparation of highly pure MnBi intermetallic compounds by arc-melting. *Materials Transactions, JIM*, 40(5), 455-458.
- Zhang, D. T., Cao, S., Yue, M., Liu, W. Q., Zhang, J. X., and Qiang, Y. (2011). Structural and magnetic properties of bulk MnBi permanent magnets. *Journal of Applied Physics*, 109(7), 07A722.
- Zhang, W., Kharel, P., Valloppilly, S., Yue, L., and Sellmyer, D. J. (2015). High-energy-product MnBi films with controllable anisotropy. *physica status solidi (b)*, 252(9), 1934-1939.
- Zhao, S. Y., Yang, S., Liang, C and Gu, D. (2016). Where is the way for rare earth industry of China: An analysis via ANP-SWOT approach. *Resources Policy*, 49, 349-357.

- ธีระพงษ์ พวงมะลิ. (2014). นาโนฟิสิกส์ Nanophysics updated edition. สำนักพิมพ์แมคกรอ-ฮิล.
- ประยูร ส่งสิริฤทธิกุล, (2020). ความก้าวหน้าของแม่เหล็กถาวรที่ปราศจากธาตุหายาก: แมงกานีส-บิสมัท. Thai Journal of Physics, 37, 2, 60-73.
- สุปรีย์ พิณิจสุนทร. (2558). วัสดุแม่เหล็ก = Magnetic materials. ขอนแก่น: โรงพิมพ์มหาวิทยาลัยขอนแก่น.





## APPENDIX

Abstract presented at the 15<sup>th</sup> Siam Physics Congress 2020 (SPC@2020), Online through hubs, Thailand.

### Preparation low-temperature phase MnBi by sintering in vacuum

Satienrapong Ngamsomrit<sup>a,b</sup>, Thanit Saisopa<sup>b,c</sup>, Jongrak Borsup<sup>a,b</sup>, Myat Su Tun<sup>a,b</sup>, Hsu Thazin Myint<sup>a,b</sup>, Hideki Nakajima<sup>d</sup>, Chomphunuch Songsiriritthigul<sup>d</sup>, Supree Pinitsoontorn<sup>e</sup>, Prayoon Songsiriritthigul<sup>a,b\*</sup>

<sup>a</sup>Research Network NANOTEC–SUT on Advanced Nanomaterials and Characterization, School of Physics, Suranaree University of Technology, Nakhon Ratchasima 30000, Thailand

<sup>b</sup>Thailand Center of Excellence in Physics, Ministry of Higher Education, Science, Research and Innovation, Bangkok 10400, Thailand

<sup>c</sup>Department of Applied Physics, Faculty of Sciences and Liberal Arts, Rajamangala University of Technology Isan, Nakhon Ratchasima 30000, Thailand

<sup>d</sup>Synchrotron Light Research Institute, Muang, Nakhon Ratchasima 30000, Thailand

<sup>e</sup>Materials Science and Nanotechnology Program, Department of Physics, Faculty of Science, Khon Kaen University, Khon Kaen, 40002, Thailand

\*Corresponding Author: sn\_1779@hotmail.com

Low-temperature phase manganese-bismuth compound (LTP-MnBi) is one of promising high-performance rare earth free magnetic materials. It exhibits outstanding magnetic properties such as high magnetocrystalline anisotropy, high curie temperature. The most unique advantage of LTP-MnBi is being large positive temperature coefficient which is favorable for high temperature applications. It is theoretically predicted that single phase of LTP-MnBi have energy product about 17.7MGOe at room temperature. Different techniques have been developed to synthesis LTP-MnBi. The most utilized technique is arc-melting followed with ball milling and low temperature annealing processes, which is time consuming. Thus, this work demonstrates that sintering in vacuum might be an alternative technique to prepare LTP-MnBi. A simple sintering system has been set up. The system has successfully been used to prepare LTP-MnBi. This report describes the system design and operational conditions. Commissioning and preliminary results from the preparation of LTP-MnBi will also be reported.

**Keyword:** LTP-MnBi. Permanent Magnet, Sintering in Vacuum

Abstract presented at the 5<sup>th</sup> International Conference on Smart Materials and Nanotechnology 2020 (SmartMat@2020), Pattaya, Thailand

Effect of Mn particle size on ferromagnetic property of MnBi prepared by sintering in vacuum

Satienrapong Ngamsomrit<sup>1,2</sup>, Tanachat Eknapakul<sup>1,2</sup>, Thanit Saisopa<sup>2,3</sup>, Kittikhun Seawsakul<sup>1,2</sup>, Hideki Nakajima<sup>4</sup>, Chomphunuch Songsiriritthigul<sup>4</sup>,

Supree Pinitsoontorn<sup>5</sup>, Prayoon Songsiriritthigul<sup>1,2\*</sup>

<sup>1</sup>Research Network NANOTEC–SUT on Advanced Nanomaterials and Characterization, School of Physics, Suranaree University of Technology, Nakhon Ratchasima 30000, Thailand

<sup>2</sup>Thailand Center of Excellence in Physics, MHEsRI, Bangkok 10400, Thailand

<sup>3</sup>Department of Applied Physics, Faculty of Sciences and Liberal Arts, Rajamangala University of Technology Isan, Nakhon Ratchasima 30000, Thailand

<sup>4</sup>Synchrotron Light Research Institute, Muang, Nakhon Ratchasima 30000, Thailand

<sup>5</sup>Institute of Nanomaterials Research and Innovation for Energy (IN-RIE), Khon Kaen University, Khon Kaen 40002, Thailand

\*Email: prayoon.song@gmail.com

The low-temperature phase MnBi has attracted both theoretical and practical interests due to its unusual magnetic properties such as high curie temperature, high magneto-crystalline, and large positive temperature coefficient which is suitable for high-temperature magnetic applications. Most of the investigated LTP-MnBi in recent years were prepared from bulk MnBi synthesized by arc- or induction-melting. To obtain LTP-MnBi powders, it requires time consuming processes such as annealing, grinding, and ball milling processes. It is known that the magnetic properties of the LTP-MnBi could be improved by reducing the particle size of powders. In this work, an alternative method to prepare LTP-MnBi is employed to reduce the processing steps. A mixer of Mn with Bi powders was sintered in vacuum at 275 °C. This investigation focused on the effects of the particle size of the starting Mn powders on the magnetic properties of the LTP-MnBi. The results obtained by using vibrating sample magnetometer, X-ray diffraction, scanning electron microscopy, energy dispersive X-Ray spectroscopy will be reported. The comparison of our data with the results obtained from others such as arc-melting LTP-MnBi will also be presented and discussed.

**Keyword:** LTP-MnBi. Permanent Magnet, Sintering in Vacuum, Microstructures

Abstract presented at the 17<sup>th</sup> Siam Physics Congress 2022 (SPC@2022), Khao Yai Convention Center (KYCC), Nakhon Ratchasima, Thailand.

### Effect of Mn grinding time on structural, chemical, and magnetic properties of the Manganese Bismuth prepared by sintering in vacuum

**Satienrapong Ngamsomrit**<sup>1,2</sup>, Tanachat Eknapakul<sup>1,2</sup>, Supree Pinitsoontorn<sup>3</sup>, Prayoon Songsiriritthigul<sup>1,2,4\*</sup>

<sup>1</sup>Research Network NANOTEC-SUT on Advanced Nanomaterials and Characterization, School of Physics, Suranaree University of Technology, Nakhon Ratchasima 30000, Thailand

<sup>2</sup>Thailand Center of Excellence in Physics, MHEsRI, Bangkok 10400, Thailand

<sup>3</sup>Institute of Nanomaterials Research and Innovation for Energy, Khon Kaen University, Khon Kaen 40002, Thailand

<sup>4</sup>Synchrotron Light Research Institute, Muang, Nakhon Ratchasima 30000, Thailand

\*Email: prayoon.song@gmail.com

This report presents the changes of structural, chemical and magnetic properties of the low-temperature phase manganese bismuth (LTP-MnBi) magnetic materials as a function of Mn grinding time. The grinding was conducted on the Mn powder with original average size of more than 400  $\mu\text{m}$  using the ball-milling technique. The grinding time was set to be 1-15 hr to obtain different Mn particle sizes prior to the MnBi synthesis. LTP-MnBi powder was successfully prepared by vacuum sintering method which was carried out at 275 °C for 12 hours at pressure below  $5 \times 10^{-7}$  mbar. Morphology, elemental composition and structure of MnBi powder were investigated by scanning electron microscopy combined with energy dispersive spectroscopy, X-ray photoemission spectroscopy and X-ray diffraction. The magnetic properties were examined using vibrating sample magnetometer. From XRD results, the MnBi content of up to 87.1% was observed with the increment of several oxides from 2.4 wt.% to 3.7wt.% as grinding time increases. This is supported by the XPS results which demonstrate the increment of MnO content on the surface as a function of Mn grinding time. It is seen that the shape of Mn particles is rather similar in all grinding conditions consisting of small and big circular shapes. We found that the average particle size decreases from 30-40  $\mu\text{m}$  to 5-6  $\mu\text{m}$  at 1-15 hr grinding time, respectively. The energy product of 1.59-1.98 MGOe was obtained in the MnBi samples prepared with different Mn grinding time. The saturation magnetization ( $M_s$ ) decreases from 53.42 to 44.32 emu/g by increasing the Mn grinding time. The unexpected decrease of  $M_s$  which strongly results to the decrease of magnetic performance might

be explained by the increase of oxides. Oxides on Mn particles could prevent the diffusion of liquid Bi to form the MnBi during sintering.

**Keyword:** LTP-MnBi, Permanent Magnet, Sintering in Vacuum, Energy Product, Magnetization



Abstract presented at the 17<sup>th</sup> Siam Physics Congress 2022 (SPC@2022), Khao Yai Convention Center (KYCC), Nakhon Ratchasima, Thailand.

### Influence of glycerin addition on formation and magnetic properties of MnBi prepared by vacuum sintering technique

Satienrapong Ngamsomrit<sup>1,2</sup>, Tanachat Eknapakul<sup>1,2</sup>, Supree Pinitsoontorn<sup>3</sup>, Prayoon Songsiriritthigul<sup>1,2,4\*</sup>

<sup>1</sup>Research Network NANOTEC–SUT on Advanced Nanomaterials and Characterization, School of Physics, Suranaree University of Technology, Nakhon Ratchasima 30000, Thailand

<sup>2</sup>Thailand Center of Excellence in Physics, MHEsRI, Bangkok 10400, Thailand

<sup>3</sup>Institute of Nanomaterials Research and Innovation for Energy, Khon Kaen University, Khon Kaen 40002, Thailand

<sup>4</sup>Synchrotron Light Research Institute, Muang, Nakhon Ratchasima 30000, Thailand

\*Email: prayoon.song@gmail.com

In this work, we present an alternative method to reduce the Mn particle size by adding glycerine during ball-milling process. This glycerin addition is expected to prevent the particle agglomeration in order to achieve the small and non-gathered Mn particles. The Mn and Bi precursors were fixed at an atomic ratio of 1:1 using Mn particles which were ball-milled in glycerin between 1 and 6 hr. It seen that the average particle size decreases from 35-40  $\mu\text{m}$  to 15-20  $\mu\text{m}$  after 1 and 6 hr grinding time, respectively. The low temperature phase MnBi (LTP-MnBi) was prepared by vacuum sintering technique using sintering temperature of 275  $^{\circ}\text{C}$  for 12 hours under ultra-high vacuum ( $\approx 10^{-8}$  mbar). The sintered LTP-MnBi samples prepared from 1 ( $\text{MnG}_1\text{Bi}$ ), 3 ( $\text{MnG}_3\text{Bi}$ ) and 6 hr ( $\text{MnG}_6\text{Bi}$ ) glycerine-added Mn grinding time were studied by X-ray diffraction, scanning electron microscopy, X-ray photoemission spectroscopy and vibrating sample magnetometry. The coercivity value ( $H_c$ ) are 3.95, 2.35 and 0.95 kOe for ( $\text{MnG}_1\text{Bi}$ ), ( $\text{MnG}_3\text{Bi}$ ) and ( $\text{MnG}_6\text{Bi}$ ) samples, respectively. The saturation magnetization ( $M_s$ ) of  $\text{MnG}_1\text{Bi}$  and  $\text{MnG}_3\text{Bi}$  are rather similar ( $\sim 0.18$  emu/g) while the  $M_s$  of  $\text{MnG}_6\text{Bi}$  is much higher than those. From XRD result, it is showed that there are a few percentages of MnBi concentration in all samples implying that glycerin addition could hinder the MnBi formation. This could be explained by the interruption of diffusion mechanism during liquid-phase sintering due to the coverage of hydrocarbon groups on Mn particles. Moreover, from elemental composition analysis, it was found that the MnO content tends to increase on the Mn surfaces as grinding time increases.

**Keyword:** LTP-MnBi, glycerin, ball-milling, liquid phase sintering, coercivity

## CURRICULUM VITAE

Name: Mr. Satiengrapong Ngamsomrit

Date and Country of Birth: 6 December 1988

### Education Background:

- 2001 B.Sc. in Applied Physics, Naresuan University, Phitsanulok, Thailand.
- 2014 M.Sc. in Applied Physics, Naresuan University, Phitsanulok, Thailand.
- 2022 Ph.D. (Applied Physics) Suranaree University of Technology, Nakhon Ratchasima, Thailand. Degree of Doctor of Philosophy.

### Work Experience:

- 2010 Assistant Research, Research and Energy Management Center (REMC), Naresuan University, Phitsanulok Province.
- 2014 Teacher, Chalermkanchana University, Phetchabun Province.
- 2015 Area Development Manager, KUMON (THAILAND) CO., LTD.  
Kumon Office (Khon Kaen Branch), Khon Kaen Province.